UCLouvain

epl

École polytechnique de Louvain

Improvement of the global efficiency of a domestic micro gas turbine using a bottoming CO_2 cycle

Dynamic analysis on the operation range of the Turbec T100

Authors: **Luca DELOS, Alice PONET**
Supervisor: **Francesco CONTINO**
Readers: **Yann BARTOSIEWICZ, Aggelos GAITANIS**
Academic year 2021–2022
Master [120] in Mechanical Engineering

Abstract

In the actual context of energy transition, a structural change is experienced by the energy system. The latter was conventionally centralized and is now becoming more renewable, spread out, thus requiring small-scale applications. A gap to fill exists for small-scale combined heat and power (CHP) units with flexible operations because of the intermittency of the renewable energy sources. Usually, Internal Combustion Engines (ICE) are the technology used for this application. However, Micro gas turbines (mGT) could be used as CHP in those smart energy grid. This technology shows potential thanks to some advantages that they present over the ICE; mostly their lower emissions levels, lower maintenance requirements and high fuel flexibility. However, they did not enter the small-scale CHP market yet because of their rather low electric efficiency (about 30 %). When the heat demand is low, the efficiency is limited to the electrical one because the exhaust gases are not valued. In this context, a bottoming cycle valorizing the waste heat of a mGT (namely, the Turbec T100) could be added to increase the electrical efficiency of this mGT. Thanks to its interesting fluid properties (high fluid density while keeping gas-like viscosity), supercritical CO_2 has shown interest in waste heat recovery applications. The present thesis will hence assess the potential of a supercritical CO_2 bottoming cycle for waste heat recovery. First, by comparing its steady-state performances with the conventional technology used in the case of waste heat recovery for the temperature ranges of the Turbec T100 exhaust (about 270 $[°C]$), namely, the Organic Rankine Cycles (ORC's). Then, because the aim of the use of the mGT is to compensate the intermittency of energy sources, they must operate in transient and part-load operations hence the bottoming cycle must also satisfy these constraints. Therefore, an analysis of the dynamic behavior of the CO_2 bottoming cycle receiving transient heat load from the mGT is required for potential future construction of such installations. In order to achieve this, the varying exhaust conditions of the Turbec T100 were used. A dynamic model, using the open-source programming language *Python* was thus developed in this thesis and calibrated with the aid of data obtained in literature. Special care was taken regarding the different components' behavior (especially the compressor and recuperator) when the working fluid was approaching critical conditions due to the sharp changes of CO_2 properties in this region.

Acknowledgments

First we would like to thank the supervising team for the proposition of this thesis. Thank you for making us discover the field of micro gas turbines and giving us the opportunity to work on the improvement of this technology.

Thank you to our supervisor, Professor Francesco Contino, who gave us his trust to work on this subject and enlightened us on the most important aspects of a master thesis.

We would like to express our deepest gratitude to our thesis advisor Aggelos Gaitanis. Without his help throughout the year and the time he dedicated to the supervision of this thesis, we wouldn't have been able to go this far in our research. He allowed this paper to be our own work, leaving us freedom on what we wanted to work on but steering us in the right direction whenever he thought we needed it. Thank you for your availability when we encountered problems and your valuable advice all along the year.

We would also like to thank Antoine Laterre for his previous work on the dynamic modeling of micro gas turbines that inspired us for the writing of this thesis and served as a basis for the subject investigated.

We would also like to acknowledge Professor Yann Bartosiewicz as a reader of this thesis, and we are grateful for taking time to read and evaluate this thesis.

We would like to express our sincere gratitude to our parents and friends for the continuous support and encouragements they provided us during all the year we spent working on this thesis, but also during all our academic journey. This accomplishment would not have been possible without them. Thank you.

Contents

List of Figures

List of Tables

Nomenclature

Symbols

d_h	Hydraulic diameter	$[m]$
Re	Reynolds number	$[-]$
$\dot{m}$	Mass flow rate	$[kg/s]$
e	Specific exergy	$[J/kg]$
h	Specific enthalpy	$[J/kg]$
h	Convective heat transfer coefficient	$[W/m^2/K]$
p	Pressure	$[Pa]$
T	Temperature	$[K]$
ρ	Density	$[kg/m^3]$
n_s	Isentropic exponent	$[-]$
c	Specific heat capacity	$[J/kg/K]$
c	Characteristic velocity	$[m/s]$
a	Speed of sound	$[m/s]$
s	Specific entropy	$[J/kg/K]$
Q	Heat flux	$[W]$
ϵ	Effectiveness	$[-]$

ϵ	Rugosity	$[m]$
ϕ	Fuel/air equivalent ratio	$[-]$
λ	Excess air coefficient	$[-]$
η	Efficiency	$[-]$
P	Power	$[W]$
f	Friction factor	$[-]$
μ	Dynamic viscosity	$[Pa\,s]$
ξ	Singular pressure losses coefficient	$[-]$
γ	Global pressure losses coefficient	$[-]$
γ	Specific heat capacities ratio	$[-]$
M	Mach number	$[-]$
M_m	Molar mass	$[kg/mol]$
PR	Pressure Ratio	$[-]$
ER	Expansion Ratio	$[-]$
MW	Molecular Weight	$[-]$
N	Rotational speed	$[rpm]$
ω	Rotational speed	$[rad/s]$
SM	Surge Margin	$[-]$
Π_h	Enthalpy rise coefficient	$[-]$
Π_m	Flow coefficient	$[-]$
Π_N	Speed coefficient	$[-]$
R_u	Universal gas constant	$[J/mol/K]$
Z	Compressibility factor	$[-]$
v	Specific volume	$[m^3/kg]$
C	Thermal capacitance	$[J/K]$

U	Global heat transfer coefficient	$[W/m^2/K]$
k	Conductive heat transfer coefficient	$[W/m/K]$
Bi	Biot number	$[-]$
Nu	Nusselt number	$[-]$
Pr	Prandtl number	$[-]$
I	Moment of inertia	$[kg\,m^2]$
Δt	Time step	$[s]$

Abbreviations

AMHX	Additive Manufacturing Heat eXchanger
CHP	Combined Heat and Power
CIP	Compressor Inlet Pressure
CIT	Compressor Inlet Temperature
COT	Compressor Outlet Temperature
CFD	Computational Fluid Dynamics
DHC	Double Heated Cycle
FEA	Finite Element Analysis
GWP	Global Warming Potential
HTT	High Temperature Turbine
HFC	Hydrofluorocarbon
IG	Ideal Gas
ICE	Internal Combustion Engines
ITAE	Integral of Time and Absolute Error
IT	Inventory tank
LNG	Liquefied Natural Gas

LTT	Low Temperature Turbine
(m)GT	(Micro) Gas Turbine
MSTE	Micro Shell Tube heat Exchanger
NTU	Number of Transfer Units
ORC	Organic Rankine Cycle
ODP	Ozone Depletion Potential
PHC	Partial Heating Cycle
PCHE	Printed Circuit Heat Exchanger
PI(D)	Proportional Integral (Derivative)
RG	Real Gas
RC	Recompression Cycle
SNL	Sandia National Laboratories
SHC	Simple Heated Cycle
SRC	Simple Recuperated Cycle
SC	Steam Cycle
$s - CO_2$	Supercritical CO_2
$t - CO_2$	Transcritical CO_2
TAC	Turbine Alternator Compressor
TIT	Turbine Inlet Temperature
WHR(U)	Waste Heat Recovery (Unit)

Research question

Within the context of energy transition, our system of energy production is experiencing a change from conventional and centralized power generation to a more renewable, spread out and small scale architecture. To balance the intermittency of renewable energy sources, flexible operation small scale combined heat and power (CHP) units are expected to play an important role [40, 96]. Micro gas turbines (mGT) could be used as CHP in those smart energy grid [6]. Indeed, this is a promising technology that presents some advantages over the internal combustion engines (ICE) that are commonly used, mostly their lower emissions levels, lower maintenance requirements and high fuel flexibility [40]. The main reason they did not enter the small-scale CHP market yet is their rather low efficiency (about 30 % electric efficiency) which limits the profitability for consumers with a variable heat demand. Indeed, when the user need for heat is low, the efficiency is limited to the electrical one as the exhaust gases are blown off and not valued [20].

The mGT considered in this study is the Turbec T100. This turbine outputs $100\,[kW]$ of electricity and $170\,[kW]$ of heat that is recuperated from the exhaust. This heat is available as a flow of about $0.79\,[kg/s]$ of flue gas at $270\,[°C]$ and is wasted when not needed. By valorizing this waste heat, the efficiency of the mGT during low heat demand could increase, allowing this technology to enter the market and induce a reduction of the emissions of CHP's.

For this purpose, some studies have already been done, investigating the micro humid air turbine cycle [20], recuperators [91] or bottoming cycles [70]. In this master thesis, the focus will be on recuperating the heat from the exhaust gases to produce electricity using a bottoming CO_2 cycle for waste heat recovery (WHR).

Considering the bottoming cycle efficiency achievable in [45] that is of 23 %, the additional work recoverable would be of $39.1\,[kW]$, which boosts the total electrical efficiency from 30 to 41.7 %. The latter model doesn't include pressure losses, considers a steady-state operation and a pressure ratio of 3.2, which does not seem realistic with the existing turbomachinery for this mass flow rate of $s - CO_2$. With a pressure ratio of 1.8 for existing turbine used in testing facilities, the efficiency could still be boosted to 37 %. This is superior to the gain in efficiency obtained using a humid air cycle in [20] (34.2 % of electrical efficiency) and is then worth investigating.

Waste heat sources can be divided into three main categories according to their temper-

ature ranges: high grade heat source (temperatures above 650 $[°C]$), medium grade heat source (temperature range between 230 and 650 $[°C]$) and low grade heat source (temperatures below 230 $[°C]$) [26]. Hence the type of waste heat from the mGT is what is considered to be medium grade. The cycles commonly used in industry for this purpose are the organic Rankine cycles (ORC). Indeed, as explained in [5], although the main solution for large size power plants for WHR is the traditional Steam Cycle (SC), for small and mid-size GT, it cannot always be compatible due to the complex architecture of this cycle and its lack of flexibility (especially when the GT operating conditions vary following the site demand). The alternative cycles used are thus more flexible and allow simpler generation of vapour thanks to lower critical temperature of the working fluid. Conventionally, ORC's are used for the considered operating range but CO_2 cycles are showing interest thanks to the interesting properties of CO_2.

The main advantages of CO_2 cycles compared to the latter for WHR are their lower turbomachinery investment costs, smaller streams of working medium in circulation, lower price of the working medium, and the properties of the working medium (ORC fluids are often hazardous) [38]. Indeed, the working fluids used in ORC's are mostly hydrofluorocarbons (HFC), which have relatively high Global Warming Potential (GWP). In addition, a HFC ORC has a constant evaporating temperature for its high pressure heat addition process. This will lead to a temperature profile mismatch between the flows of heat source and the ORC working fluid, thus increasing irreversible losses and reducing system efficiency. These will influence long term applications of ORC system in the future [46]. What also makes $s-CO_2$ technology attractive and competitive with respect to the ORC solution according to [5] is the fact that $s-CO_2$ is a high density fluid similar to liquid water throughout the cycle, is non-toxic, nonflammable and abundant, possibly provided by greenhouse gas emission sequesters. Also, the CO_2 cycles seem to operate efficiently on a higher range of operation [85], which is an important aspect since it should work on the whole range of operation of the mGT. Flexibility is then an important aspect.

But $s-CO_2$ cycles still present challenges, the technology being at an early stage and not yet ready to enter the market. Some of the current challenges according to [5] are the development of compact high pressure heat exchangers at reasonable cost, the reduction of leakage and mechanical losses in turbomachines and the optimal regulation and safe operating conditions of the compressor near the CO_2 critical point (as shown by [66], a significant decrease in static temperature and static pressure in the local area of flow acceleration is observed indicating a high potential for the appearance of two-phase condition inside the compressor). The sharp change of fluid properties in this region showing potential implications on the stable and safe operation of the compressor and thus of the cycle and the real gas behavior also makes very questionable the application of the know-how gained on conventional turbomachines to the $s-CO_2$ compressor. Indeed, as said in [4], while $s-CO_2$ high fluid density results in the compactness of the turbomachinery (hence reducing the material costs and showing interest in low space and potentially low weight applications) the combination of pressure, temperature, and density in $s-CO_2$ power cycles are outside the experience base of existing turbomachines such as gas turbines, steam turbines, and even high-pressure gas compressors. $s-CO_2$ turbomachinery design is thus a significant challenge for realizing these cycles.

To make sure the components of the cycle, and mostly the turbomachinery, operate in a safe zone despite the variable waste heat profile from the mGT, dynamic modeling of the cycle is necessary. Indeed, the flexibility of operation of the mGT induces a high variability of

its exhaust as well in mass flow rate than in temperature. To maximize the energy recuperated by the cycle on the range of operation of the mGT, a control strategy must also be designed. To do so, dynamic performances must be obtained and modeled. It is critical for $s-CO_2$ cycles to not only consider the design point as the properties of the fluid might change at part load, as well as the efficiency of the turbomachinery [84].

The precise aim of the following research should assess the potential increase of the efficiency of the mGT from the addition of the $s-CO_2$ bottoming cycle. First, by comparing this cycle to the conventional Rankine cycles using organic fluids compatible with the temperature range from the mGT (for example R113 and R245fa as done in [69]) in steady-state conditions to show the interest of $s-CO_2$ cycles. Secondly, by doing a dynamic analysis and by investigating on turbomachinery and heat exchangers compatible with such cycles and the challenges associated with them. The development of a dynamic tool for simulation will allow future research on the field and the investigation of control strategies.

Thesis structure

This thesis will follow the structure described hereunder. It follows the thesis of A. Laterre [40] about the modeling of the mGT Turbec T100 from which we aim to improve the efficiency by adding a CO_2 bottoming cycle. This work is in view of a potential installation construction.

- **Chapter 1 - Review of literature** serves as a presentation of the overall context followed by a more specific overview of the challenges, technologies and perspectives around the application considered. This Chapter's purpose is to make the gap in the research field more obvious introducing the need for the work presented.
- **Chapter 2 - Potential of CO_2 bottoming cycle** shows a steady-state analysis of four cycles; two CO_2 cycles differing in their compressor entry conditions and two ORC's. The purpose is to investigate if the performances of CO_2 cycles are of the same order of magnitude than the main technology today for waste heat recovery, the ORC's.
- **Chapter 3 - Physical model** will thoroughly explain the main assumptions taken for the dynamic modeling of the system as well as the methodology employed for the physical model, considering a block approach for the dynamic modeling taking into account the main phenomena of the system.
- **Chapter 4 - Numerical model** will graphically show the sequential procedure used in the model implemented.
- **Chapter 5 - Estimation and tuning of the parameters** shows how the different parameters used in the cycle were estimated due to lack of experimental data.
- **Chapter 6 - Dynamic analysis results** serves as an investigation of the behavior of the designed model for waste heat recovery of the mGT exhaust. First some sensitivity analysis on important parameters of the cycle have been carried out. Afterwards, a dynamic simulation of the cycle has been made while recovering changing exhaust flow and temperature of the mGT. The simulation is the one obtained during a change of operation of the Turbec T100, from 100 to 80 $[kW]$ and from 90 to 100 $[kW]$.
- **Chapter 7 - Conclusion** summarizes the main findings and discusses the further potential improvements.

CHAPTER 1

Literature review

1.1 Introduction

This Chapter serves as an assessment of overall properties, technologies and perspectives around supercritical carbon dioxide in order to have a better understanding of the challenges and particularities to face in further modeling of supercritical cycles.

This includes a review of supercritical CO_2 properties, applications using supercritical CO_2 in power cycles, types of cycle layouts used and their characteristics, a component review with special focus on the key components such as the compressor, the turbine and heat exchangers. Lastly a review of transient modeling of supercritical CO_2 will be made.

1.2 Supercritical CO_2 cycles

Supercritical fluids are fluids where pressure and temperature exceed the critical pressure and temperature. In this case, it can thus adopt properties midway between liquid and gas. Historically, the concept of power cycles using CO_2 as a working fluid was presented in 1948 when Sulzer Bros completed a patent for a partial condensation CO_2 Brayton cycle [23]. In recent years, the focus on reducing energy losses has pushed to further investigate power cycles using supercritical CO_2. Power cycles using supercritical CO_2 take advantage of the real gas behavior in order to achieve high thermal efficiency and reduce compressor work (usually working near the critical point where the properties of the fluid change sharply) [37].

1.2.1 Supercritical CO_2 properties

CO_2 presents a high critical pressure $p_{crit} = 73.77\,[bar]$ while a relatively low critical temperature $T_{crit} = 30.98\,[°C]$ resulting in unique challenges for supercritical CO_2 cycles.

The main advantages of CO_2 can be summed up as follows; the high operating pressures enable smaller size components, supercritical CO_2 cycles achieve high efficiencies at low temperatures, CO_2 is a very stable, non-toxic, non-flammable fluid, it is not hazardous to waters, it has a low critical temperature (which allows to use water at ambient temperature

as a coolant), is abundantly available and maintains a low viscosity with high density. Furthermore, it possesses high power density, low surface tension (reduced effects of cavitation in the machinery) and low molecular leak due to higher molecular mass. Moreover, it is low costs, easily handled and plant personnel is accustomed to CO_2 [37].

In a small range of temperature and pressure starting at the critical point and extending to greater pressure and temperature values, some properties of supercritical CO_2 exhibit very sharp changes. When these relevant thermodynamic properties are represented in pressure-temperature space, curves linking the inflection points of these properties for different conditions represent what is called *pseudo-critical lines*. Various physico-chemical quantities (e.g. compressibility, heat capacity, density and speed of sound) have different *pseudo-critical lines* and collectively these curves define a pseudo-critical region, located in a area [76] represented in Fig. 1.1. The supercritical space is divided into three areas: the liquid-like, pseudo-critical and vapour-like regions.

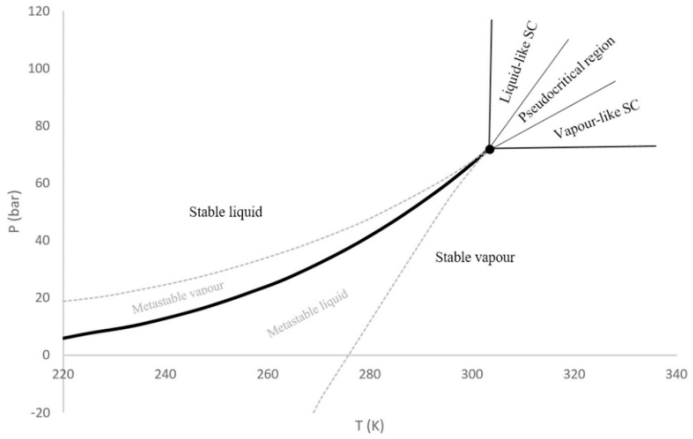

Figure 1.1: Phase diagram of CO_2 showing the defined supercritical regions [76]

Examples of *pseudo-critical lines* of the Specific Heat Capacity and the Isentropic Exponent (defined by equation (3.18)) are represented in Fig. 1.2.

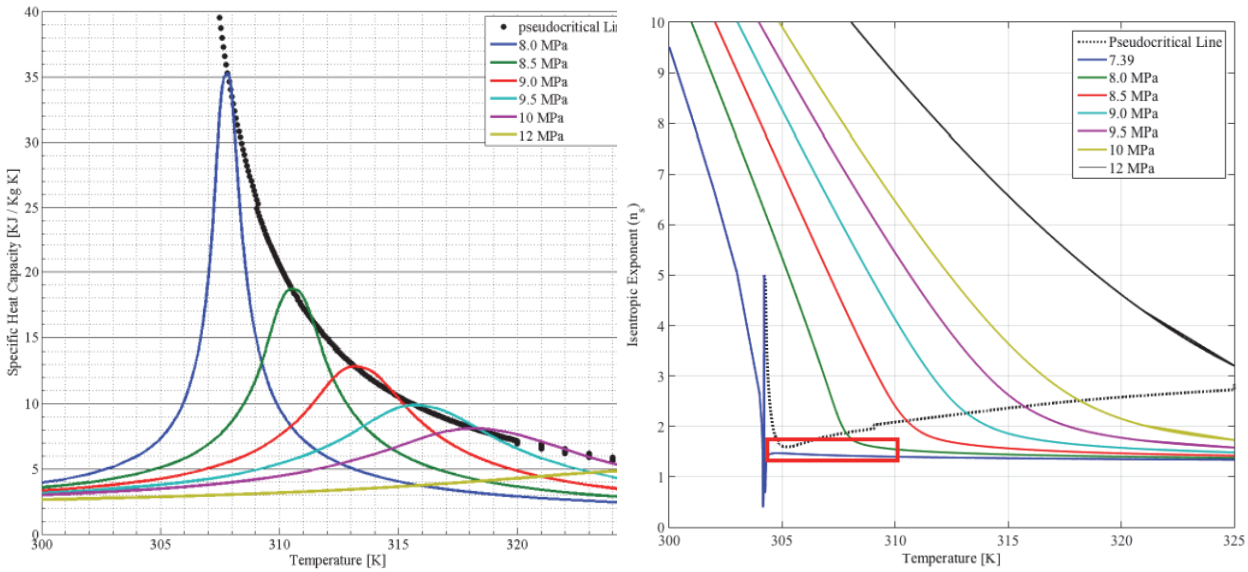

Figure 1.2: Pseudo-critical lines examples [56]

Fig. 1.3 and Fig. 1.4 show the density and speed of sound (the latter defined in equation (3.16) for a real gas) variations of supercritical CO_2.

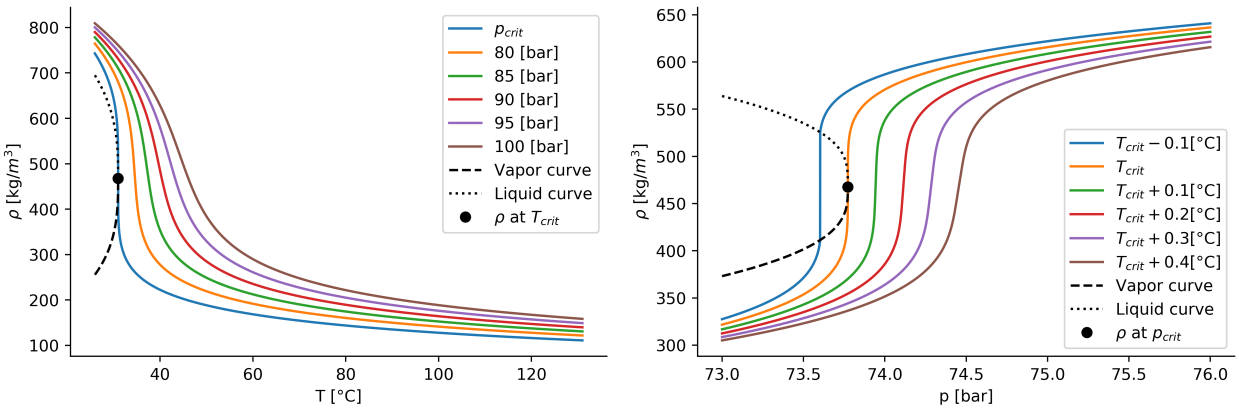

Figure 1.3: CO_2 density variations in function of (a) temperature, (b) pressure

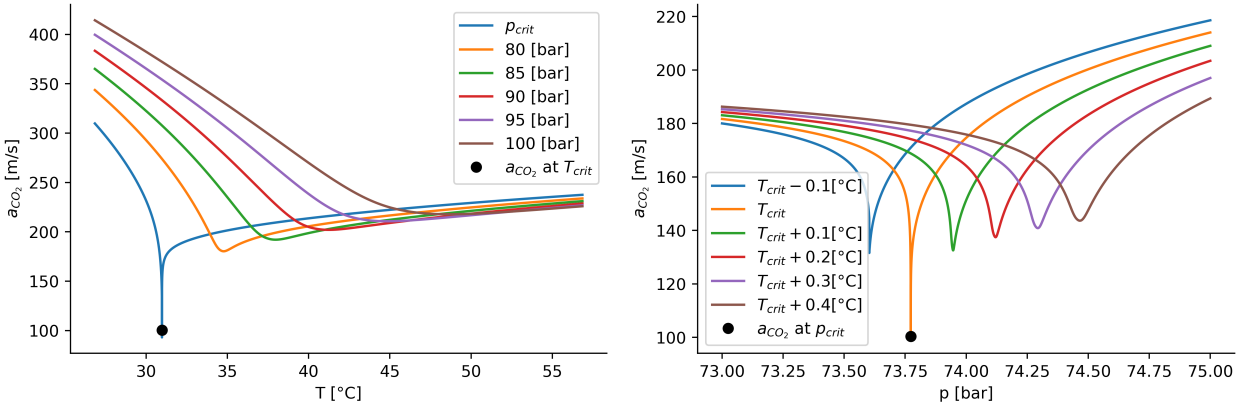

Figure 1.4: CO_2 speed of sound variations in function of (a) temperature, (b) pressure

This illustrates the sharp changes of fluid properties with relatively small temperature and pressure changes. One can also distinguish the supercritical liquid-like and vapour-like fluid from the sharp changes in density with pressure and temperature in Fig. 1.3.

1.2.2 Applications in power cycles

Supercritical CO_2, due to its improved thermal-to-mechanical conversion efficiency, has received increasing interest for electric production thanks to its coupling with many different power sources including nuclear energy, fossil fuels, waste heat, solar energy, and fuel cells as well as coal-fired power plant [22, 44].

Recently, many researchers have focused on the application of carbon dioxide power cycle for waste heat recovery [44]. The most mature technology for waste heat recovery today are the Organic Rankine Cycles (ORC's) and Steam Cycles (SC's), where, in most cases, all of

the cycle takes place in the subcritical region. On the contrary, supercritical CO_2 systems still need significant development to enable their penetration in the market, both at the system and at the component level [71]. Supercritical CO_2 shows a great range of temperature from which it can recuperate heat. It can recover low grade heat source (with temperatures below 230 $[°C]$) with the use of a transcritical cycle (some states of the cycle are taking place in subcritical conditions), which is most effective at harvesting low-grade heat sources when a low temperature heat sink is accessible [26]. This is especially interesting since there are large amounts (more than 50 % according to statistics) of low grade heat sources from industrial waste and renewables that can be converted into electricity through advanced thermodynamic power cycles and appropriate working fluids. However, very few experiments have been made considering power cycles with transcritical CO_2 cycles in which actual power generations were measured; most investigations are limited to theoretical and small-scale laboratory work [26]. Furthermore, supercritical CO_2 cycles represent a potentially more effective solution than ORC's for heat source temperatures greater than 350 $[°C]$; this is particularly true if cold water is available, making condensation possible [8]. In the case of SC's, they become expensive for low temperature heat sources in comparison to potential CO_2 systems [37].

Other drawbacks of ORC's and SC's compared to supercritical CO_2 is their constant evaporation temperature, which increases irreversibly during the heat addition process when using sensible heat sources such as waste heat. In comparison, the supercritical heat addition process of a supercritical/transcritical cycle can produce high efficiency temperature matching between the sensible heat source and the working fluid, leading to no pinch limitations. Furthermore, due to the high fluid density and other properties (latent heat, specific heat, thermal conductivity, volumetric cooling capacity, and lower viscosity) of supercritical CO_2 cycles, it allows for more compact components than in the case of ORC's. Due to their efficiency and compactness, supercritical CO_2 cycles have the potential to be applied in distributed or portable energy systems [92]. Moreover, a hydrofluorocarbon (HFC) working fluid is usually used in ORC's, which has zero Ozone Depletion Potential (ODP) but a relatively high global warming potential (GWP) hence posing a threat to the environment [26]. Thermal stability (limiting the achievable cycle maximum temperature, due to fluids thermal decomposition [7]) is a significant property of ORC working fluids and is the primary limitation for working fluid selection and system design [18].

As of today, the development of supercritical cycles presents many scientific and technological challenges; commercial operation of a supercritical CO_2 cycle power plant is not yet available. Globally, there is a lack of methodology for system design and analysis for supercritical CO_2 cycles receiving heat from different heat sources under design and off-design conditions and transient operation. Furthermore, heat transfer and heat to power processes are not well known resulting in non-optimized design for cycle components. Moreover, technological barriers exist for fabrication, seal, leakage and rotor-dynamics stability of the key components [92]. Further improvements required are for example the development of compact high pressure heat exchangers at reasonable cost, the reduction of leakage and mechanical losses in turbomachines, the selection of materials compatible with high cycle pressure and possible corrosion at high temperatures, etc [5].

1.2.3 Cycles layout

Fig. 1.5, Fig. 1.6 and Fig. 1.7 show the three basic CO_2 power cycles. The main difference lies in the compressor inlet conditions influencing the fluid properties.

- **Supercritical Brayton cycle**

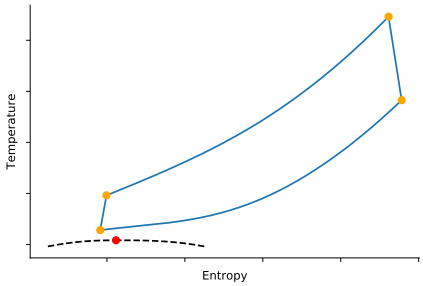

Figure 1.5: T-s diagram of $s - CO_2$ Brayton cycle example

All of the states in this cycle are supercritical; hence the inlet condition of the compressor is above the critical point (red dot in Fig. 1.5) both in temperature and pressure. In the case of Fig. 1.5, the entry of the compressor is located in the liquid-like supercritical space (see Fig. 1.1) because of the high inlet pressure compared to inlet temperature (making the point at the left of the critical point).

- **Transcritical Brayton cycle**

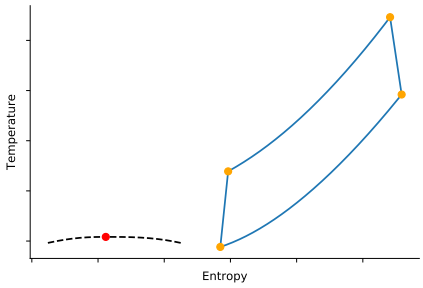

Figure 1.6: T-s diagram of $t - CO_2$ Brayton cycle example

The inlet of the compressor is below the critical point but in the vapour region. Hence part of the cycle takes place in the subcritical vapour region and part of cycle is in the supercritical vapour-like region and only one phase is present during the cycle.

- **Transcritical Rankine cycle**

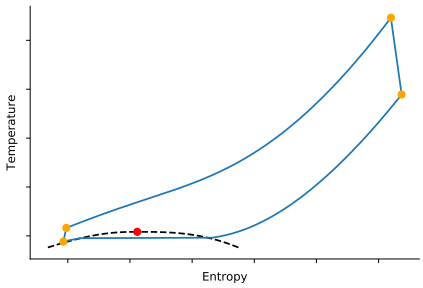

Figure 1.7: T-s diagram of $t - CO_2$ Rankine cycle example

The inlet of the compressor takes place in the subcritical liquid region. During part of the heat rejection process, condensation takes place hence a two-phase fluid appears. This might lead to a pinch point difficulty in the cooling section. For a same inlet temperature as the $t - CO_2$ Brayton cycle, the inlet pressure must increase for a liquid entry.

In practice, for a power cycle recuperating heat of low grade temperature, the Rankine transcritical cycle is used because of the good thermal match of temperature and because of the lower work achieved at the pump; this explains the scarce appearance of the transcritical Brayton cycle in the literature whose entry properties impose higher compressor work.

More advanced cycles are used in practice. Two relatively simple cycle layouts are considered the basis in the case of supercritical cycles; the Recompression Cycle (RC) and the Simple Recuperated Cycle (SRC) shown in Fig. 1.8 and Fig. 1.9. There is no consensus in literature on which cycle shows the best thermodynamic efficiency. This is because of all the various heat source existing to drive a supercritical CO_2 cycle, there is not a fixed cycle that can be suitable for all the heat sources [92]. A drawback of the SRC is the huge cycle irreversibility due to the recuperator's internal irreversibility. RC were thus introduced to resolve this problem [9]. Moroz et *al.* [59] evaluated the thermodynamic performance of a SRC and a RC as the bottom cycle of gas turbine. They found that the recuperated cycle might be the best choice among the three candidates. However, Khadse et *al.* [35] analyzed and optimized the performance of a SRC and a RC for waste heat recovery of gas turbine from the perspective of thermodynamics and economics. In their analysis, it comes out that the RC seems to outperform the SRC. But they also pointed out that the performance of the bottom cycle was highly dependent with the characteristics of flue gas [44]. And according to Kim et *al.* [36], the RC is suitable for nuclear or solar energy, but is not good for waste heat recovery [44, 92].

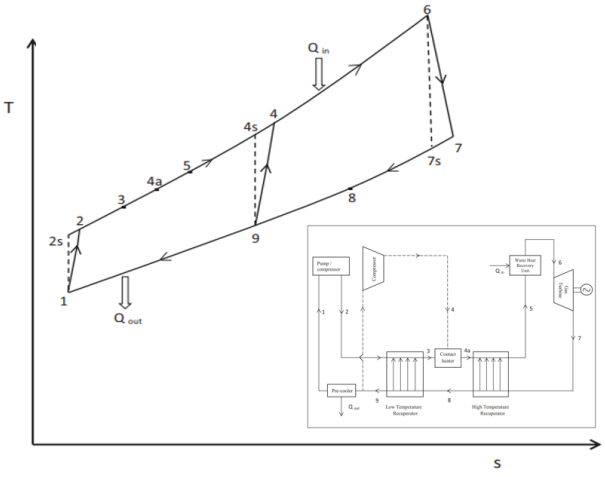

Figure 1.8: T-s diagram and layout of the Recompression Cycle [9]

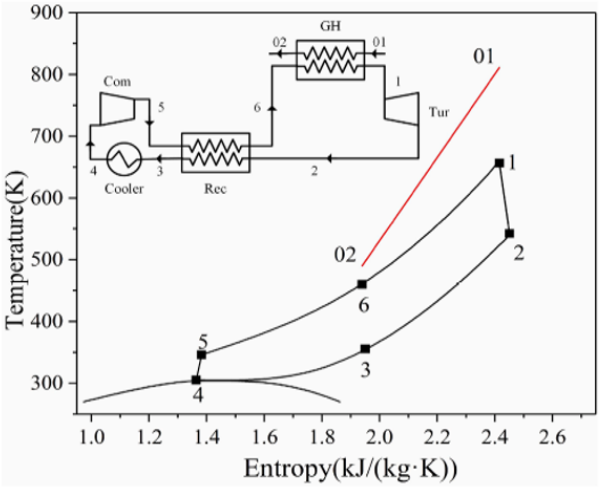

Figure 1.9: T-s diagram and layout of the Simple Recuperated Cycle [44]

The SRC only adds a recuperator whereas, for the RC, the recuperator is divided into two sections; the low temperature one and the high temperature one. This cycle can start from supercritical or subcritical conditions. Part of the flow from the low temperature recuperator in the low pressure side is recompressed to the high pressure side without entering the cooler. The recompressed flow joins the main stream before the high temperature recuperator and hence recuperators have unequal mass flow rates. Since the mass of the fluid is sufficiently reduced in the high pressure side before recombination, the difference in constant pressure specific heats values between the two pressure zones is compensated (this difference is causing irreversibility especially in the low temperature recuperator) and the temperature at the exit of the recuperator is higher than earlier [9].

Li et *al.* [44] have made a comparison between four types of supercritical CO_2 cycles layout going from the simplest type, the Simple Recuperated Cycle (SRC), to a slightly more complex, the Partial Heating Cycle (PHC), to the most complex layouts, the Simple Heated and Double Heated Cascade Cycles (SHC and DHC). Partial heating separates the gas heater into the low temperature gas heater and the high temperature gas heater. In the

Partial Heating Cycle, part of the flow absorbs heat in the recuperator while the other part is preheated in the low temperature gas heater. The point is to reduce the exergy destruction in the recuperator. As for the CO_2 power Cascade Cycles, their layouts can vary substantially. Nevertheless, the common feature of cascade CO_2 power cycles is that there are two turbines in the system with different inlet temperatures, namely low-temperature turbine (LTT) and high temperature turbine (HTT). The Single Heated Cascade cycle possesses one gas heater whereas the Double Heated Cascade cycle possesses two. A summary of six cycles belonging to the four types of cycles described above is shown in Fig. 1.10, Fig. 1.11, Fig. 1.12, Fig. 1.13, Fig. 1.14 and Fig. 1.15 all coming from [44].

One can see that the number of components of the layout increases with its complexity. Compared to the SRC, the PHC possesses one more component, whereas the SHC's possess two more and the DHC's three more. Their analysis globally shows that the more complex cycles present the best exergy efficiency (DHC II showed the best performance) while the simplest (SRC) the worse. It should be noted that the PHC showed good exergy efficiency with relatively simple layout. However the least compact cycles also show higher specific investment cost.

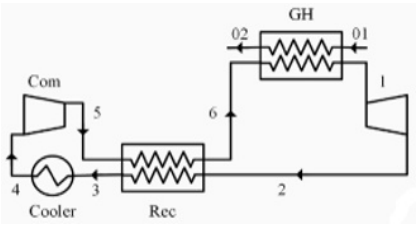

Figure 1.10: SRC layout

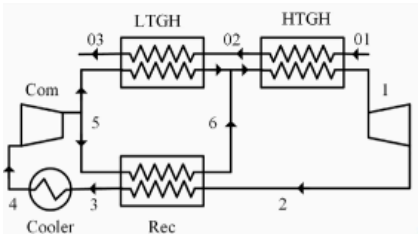

Figure 1.11: PHC layout

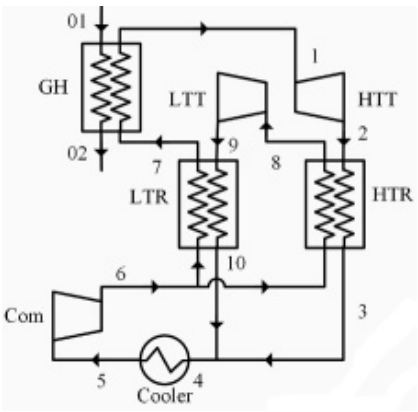

Figure 1.12: SHC I layout

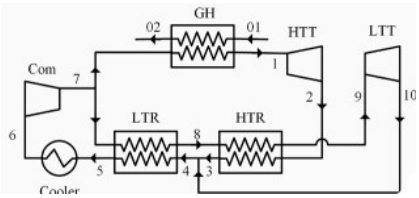

Figure 1.13: SHC II layout

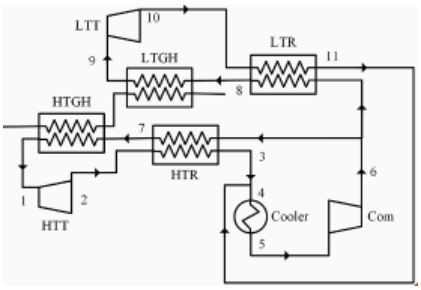

Figure 1.14: DHC I layout

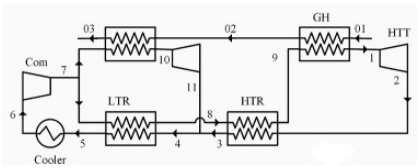

Figure 1.15: DHC II layout

1.2.4 Economical aspects

Li et *al.* [44] showed that the economic and thermodynamic performances were in conflict by nature, requiring compromises between the two aspects during the design. Even if the development of supercritical CO_2 cycles is only at its early stages, making the estimation of the cost of components imprecise, they were able to conclude that the turbine had the highest investment cost of the components and this investment increases with power generated (idem for the compressor and consumed power). Logically, the higher performances of heat

exchangers are achieved at the expense of larger heat transfer area and higher investment cost. The compactness of $s-CO_2$ turbomachines allows for the reduction of their cost. In addition, compact heat exchangers whose smaller equipment sizes might result in smaller carbon footprint could potentially have lower capital cost than a comparable SC's [4].

However, in opposition to the lower turbine size in the supercritical CO_2 cycles, the analysis made by Ancona et *al.* [5] suggest that higher heat exchanger investment costs could be expected for supercritical CO_2 bottoming cycles rather than ORC's, given the higher total heat exchanger size, which can be more than three times the ORC's configuration's one. They concluded that the overall investment cost is higher in the case of CO_2 despite showing better performances than ORC's in their analysis.

1.3 Components

Special attention must be paid to components in supercritical CO_2 cycles. Indeed, various challenges due to high pressure operations, compactness of the components, among other things, make the supercritical CO_2 component design subject unique combinations of temperature, pressure and size of components occurring in such cycles.

Due to high power density of turbomachines, it requires bearings to face high bearing surface speed and high unit load (resulting from asymmetric pressure differences across volutes and scrolls at off-design operation) [4]. Furthermore, another challenge lies in the casing design of the turbines. Moreover, the need of dry gas seals at the end of the shaft requires a sharp temperature gradient in the pressure containment near the ends of the casing, which is unique to supercritical CO_2 turbines. Furthermore, the complex nature of typical turbomachinery case geometries requires to employ Finite Element Analysis (FEA) to design for pressure containment [4].

In accordance with current research data, the maximum pressure allowed in the cycle is of $300\,[bar]$ due to technological limitations [5] bounding the possible pressure ratio hence the power potentially available from the cycle. In practice, this maximum is usually even smaller since values of pressure ratios at the compressor hardly ever exceed 3 while the compressor inlet pressure value stays close to critical pressure (e.g. Klemencic et *al.* [37] used a compressor inlet pressure of $73.8\,[bar]$ while having a maximum cycle pressure of $221.4\,[bar]$ meaning a pressure ratio of 3, which is relatively high compared to other values found in literature).

Static seals must also be of concern for turbomachines. In many cases, seals made of elastomeric materials provide good option up to temperatures going to $315\,[°C]$. But these materials, especially in the case of $s-CO_2$ cycles, are at risk of explosive decompression when fluid that has slowly absorbed into the material during pressurized operation expands within the material during a decompression event leading to material failure [4].

1.3.1 Turbomachinery

Due to compact turbomachinery, the rotational speed of the latter is relatively higher compared to other applications, particularly at relatively small power block scales [4]. Furthermore, due to high pressures, high axial forces are in action [79]. Fig. 1.16 shows the scale difference between $s-CO_2$ turbines and steam turbines for the same power output.

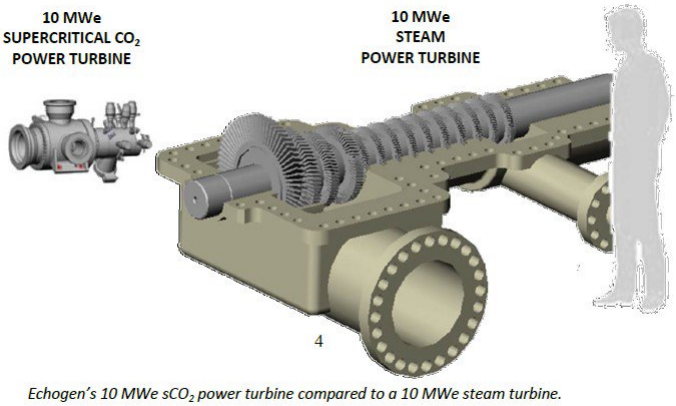

Figure 1.16: Turbine size comparison between $s-CO_2$ and steam turbines for 10 $[MW_e]$ output [17]

Compressor

One should first note that the distinction between pumps and compressor in $s-CO_2$ applications is not relevant since the fluid densities at liquid, gas, supercritical (vapour-like and liquid-like) states are all high [4]. Hence the terminology "compressor" is applied to compressor as well as pumps. Compressors in CO_2 applications are centrifugal ones for most scales. However, both axial and centrifugal compressors can be used at the multi-hundred MW_e scale [4]. Compressors typically operate in the region surrounding the critical point to take advantage of the reduced work due to fluid properties in this region (typically at the top-left the the critical point in the liquid-like region by lowering inlet temperature). This typically complicates the computational task of $s-CO_2$ compressor design since fluid properties change sharply and vary greatly from the ideal gas assumption requiring the use of proper tables. Furthermore, since the compressor inlet conditions are very near the the two-phase region, convergence issues might take place due to simulated phase change. Indeed, locally inside the compressor, an increase in fluid velocity induces local static temperature and pressure drop allowing for the local flow state to go under the saturation curve in the two-phase region [4] as seen in Fig. 1.17. Currently, the effect of two-phase flows on compressor performance for $s-CO_2$ applications is in practice unknown, the principal obstacle that the appearance of this flow causes is the fact that there is a lack of suitable computational tools available to deal with high-speed non-ideal two-phase flows interacting with compressor blades [71].

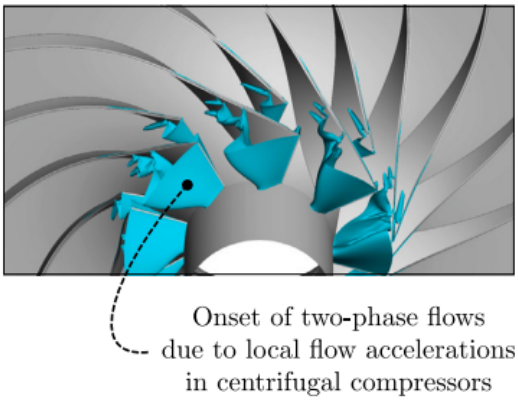

Figure 1.17: CO_2 two-phase flow apparition within the impeller blade channel [72]

The fact that small changes in intake conditions change greatly the properties of the working fluid induce several important consequences to take into consideration. Recall that the fluid can exhibit liquid-like or vapour-like behavior. These large volumetric variation of CO_2 in the region of interest for centrifugal compressors pose unprecedented challenges for compressor design. When the compressor works in its gas-like form, the compressor loading increases with a consequent reduction in the efficiency [71]. These sharp properties variation also impact the impeller mechanical design; the high fluid density in $s-CO_2$ impellers will also affect the natural frequencies of blade-dominant modes and generates relatively high aerodynamic loading amplitudes and large fluctuations in volume flow [4].

Turbine

Turbines are typically radial designs below $10\,[MW_e]$ and axial designs above $50\,[MW_e]$, with overlapping designs in the $10-50\,[MW_e]$ range. The combination of very high pressures in the turbine as well as elevated temperatures for some cycles require special matters for material selection of $s-CO_2$ turbines. Another consideration for material choice is possible corrosion of CO_2.

Furthermore, $s-CO_2$ turbines are all the more vulnerable to over-speed hence requiring a trip valve and protection system to prevent this phenomena. Because of the compactness of the turbine and the low inertia of the turbine rotor, these turbines are highly sensitive to sudden loss of electrical load. Moreover, due to the high power density of $s-CO_2$ turbines, the pressure loading on turbines blades has to be particularly taken into account. This issue is also worsened by the relatively small size of the the wheels and shaft requiring particular concerns for shaft attachment [4].

1.3.2 Heat exchanger

In $s-CO_2$ application, the pressure ratio of the compressor is limited. Pressure losses in heat exchangers should then be minimized because of their effect on the overall efficiency of the cycle. Indeed, they directly decrease the pressure ratio of the turbine and then the extracted power.

Heat exchangers must be designed to avoid pressure losses and that is why compact heat exchangers are used. A compact heat exchanger is defined by a surface area density (i.e. ratio of heat transfer area to heat exchanger volume) $A/V > 700\,[m^2/m^3]$ and hydraulic diameter $d_h < 6\,[mm]$ when the working fluid is gaseous according to Shah et *al.* [78]. As a comparison a typical shell and tube heat exchanger (widely used due to its flexibility and ability to withstand high temperature) from process industry has a surface density of less than $100\,[m^2/m^3]$. Moreover, adopting compact heat exchangers allows a reduction of the volume of heat exchangers. One of the benefits of $s-CO_2$ cycles is the possibility to downsize the turbomachinery. Using heat exchangers with high compactness significantly the volume occupied which is necessary to attain compactness of the whole cycle.

Pressure losses reduction is not trivial. Indeed, there exists a trade-off between pressure losses reduction, cost and heat duty [54]. A reduction of pressure drops is achieved by reducing the wet surface of the heat exchanger, limiting the heat transfer. On the other hand, an increase in heat duty increases the effectiveness ϵ of the heat exchanger and so the efficiency of the cycle, at the cost of an increase in heat transfer area, inducing an augmentation of pressure losses and cost. Because of the small scale application, the cost is also of importance and

should be taken into account during the choice of the exchanger.

Kwon and *al.* [39] investigated the different technologies available for compact heat exchangers adapted for $s-CO_2$ power cycle application. The Printed Circuit Heat Exchanger (PCHE) is the most promising and most widely adopted heat exchanger in the field. This type of heat exchanger is quite new as it has first been introduced in the market by the Heatric Company in 1985 in Australia. It has first been used in the offshore industry and Liquefied Natural Gas (LNG) plants where space and weight savings are of major importance. It has then been used in helium and $s-CO_2$ Brayton cycles, allowing for a reduction of 85 % in size compared to conventional shell and tube heat exchanger. The latter is not used for $s-CO_2$ due to the too high heat transfer surface required to reach an effectiveness of at least 85 %. Reducing the channel diameter, a so-called Micro Shell and Tube heat Exchanger (MSTE) is obtained with increased compactness. the drawback of this technology is the high manufacturing cost due to the special welding operation required and the structural issues that can occur due to tube buckling [39, 52]. Additive Manufacturing Heat eXchanger (AMHX) is an other technology showing a promising potential. The additive manufacturing, also called 3D printing, allows the fabrication of complex geometries. The heat exchanger is manufactured into a single monolithic bloc by adding layer after layer of material in the form of a powder. The reduced material shrinkage can make this technology cheaper than PCHE [52]. The use of this kind of heat exchanger is quite complex as no hydraulic correlation have been developed yet.

Printed Circuit Heat Exchanger

Printed circuit heat exchanger (PCHE) is widely used for $s-CO_2$ applications in recuperators due to its high heat transfer capacity, wide operation range and long-term structural integrity. Being the most popular option, there exists various studies analyzing the behaviour of PCHE for recuperator in $s-CO_2$ cycle.

The PCHE is composed of a stacking of photochemically etched plates [32, 48]. This process uses corrosive oxidation and does not alter the internal structure of the metal. The manufacturing process is similar to the one of electronic circuit printed board, hence the name PCHE. The channels are usually semicircular, with a depth varying between 0.1 to 2.5 $[mm]$. This shape of channels proved to provide the best heat transfer among the ones studied in [65]. The etching process allows for a flexibility in geometry, allowing for various angle increment during manufacturing process. The plates are then stacked and bonded together by diffusion bonding at a temperature 0.6 to 0.7 times the melting temperature of the material used. Diffusion bonding is a solid state welding technique by which two surfaces are bonded together under high temperature and mechanical pressure in a protected environment. The pressure brings two surfaces into intimate contact and the heat promotes grain growth through the interface of the plates [41]. The process results in a compact exchanger core with high integrity. The properties of the metal used for the manufacturing are conserved. On Fig. 1.18 a micrograph of the crossflow section of a PCHE is shown. It can be seen that the grains of metal have grown through the interface, building a monolithic bloc without mechanical defect at the interface. It allows for an improved resistance to pressure difference.

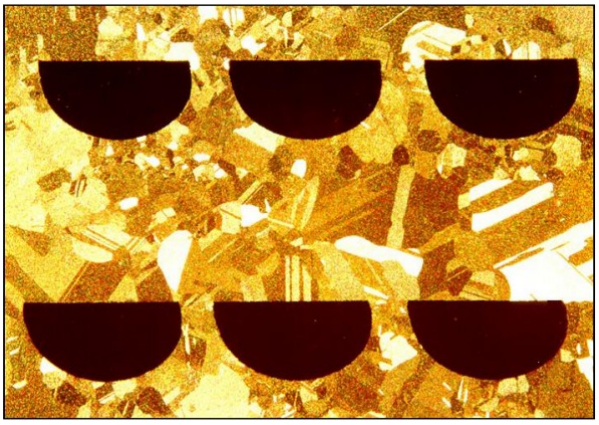

Figure 1.18: Micrograph of a PCHE section in the crossflow region from Heatric [41]

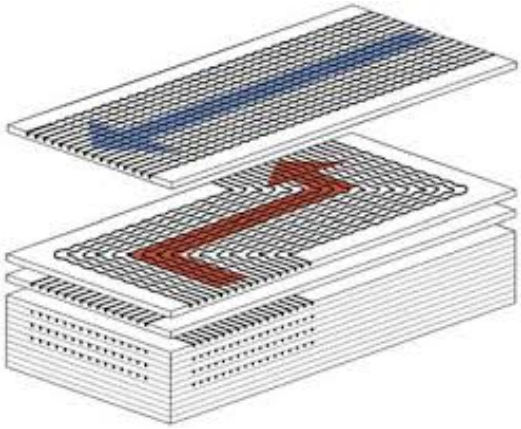

Figure 1.19: Typical layout of a zigzag PCHE from Heatric [41]

For the choice of material, most manufacturers use stainless steel to limit the cost. The operating temperature is then limited to $600 - 650\,[°C]$ to avoid creep deformation. The occurrence of creep deformation in the compact passage of PCHE can induce a flow passage blockage, increasing the back pressure of the heat exchanger. At higher temperature nickel-based alloys at titanium are used at much higher capital cost [14].

Currently four main types of PCHE configuration for flow passage have been developed and studied in literature: straight channel, zigzag or wavy channel, channel with S-shaped fins, and channel with airfoil fins (see Fig. 1.20). The thermohydraulic performances of those four types of PCHE's have been studied in [14, 48]. In most case the transfer area is the same for the hot and cold side of the exchanger. However it is possible to design it using two plates of hot fluid per plate of cold fluid , as in [61]. In some case, increasing the heat transfer area on the hot side can increase the maximum heat transfer [32].

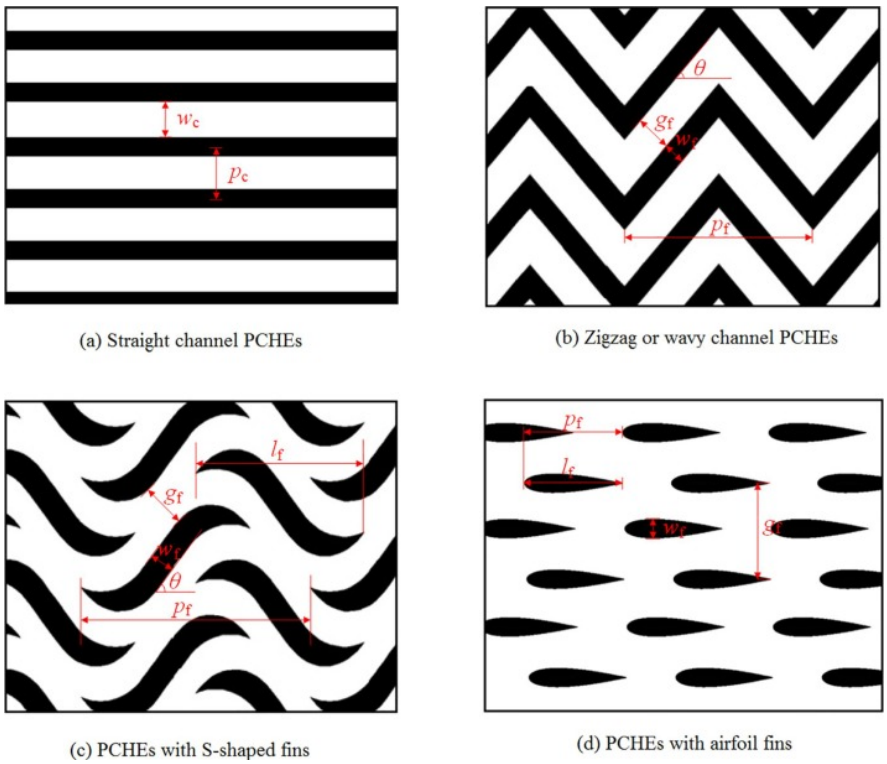

(a) Straight channel PCHEs

(b) Zigzag or wavy channel PCHEs

(c) PCHEs with S-shaped fins

(d) PCHEs with airfoil fins

Figure 1.20: Four main types of PCHE's from [14]

Among those four channel configurations, the zigzag one is the most widely used. This configuration improves the thermohydraulic performances and compactness at the cost of an increase in pressure losses compared to straight channel. The S-shaped and airfoil PCHE have discontinuous channels. The flow resistance is lower than for the zigzag channel for the same heat transfer [48], inducing reduced pressure drop and avoids channel blockage as the flow can go from one channel to an other [39]. The cycle efficiency is then increased by choosing this channel configuration. However discontinuous channels are hard to manufacture, resulting in a higher capital cost.

In [48], it can be seen that the zigzag PCHE is the one requiring the smallest volume for a certain effectiveness. On Fig. 1.21, the evolution of the efficiency of the cycle as a function of the Reynolds number (Re) can be seen for two recuperator effectiveness for the four channel configurations. The volume is also indicated on the right axis. At low effectiveness and low Reynolds number the efficiency stays the same no matter what configuration is used because the effect of pressure losses on the cycle is negligible. At high Reynolds and high effectiveness, the zigzag configuration shows poorer performance compared to the discontinuous PCHE. However the volume with this geometry is always reduced by a factor two compared to the other ones. The higher compactness induces a smaller cost and a faster dynamic during transient. This is why zigzag configuration is generally preferred and is more studied in literature [14, 48, 54, 61, 65, 77]. Hence Computational Fluid Dynamics (CFD) results are available for model validation.

In the design of the recuperator, increasing the Reynolds number reduces the volume of the PCHE but increases the pressure losses at a fixed effectiveness. At a fixed volume, increasing the Reynolds number increases the effectiveness and pressure losses. Very high effectiveness (higher than 0.95) is not recommended as the higher the gain in efficiency due to the higher heat exchanged is counterbalanced by the loss due to the higher pressure drop. This is why a range of Re between $15000 - 30000$ and ϵ between $0.9 - 0.95$ is recommended [48]. It can be seen on Fig. 1.21 that at higher Reynolds number the gain in volume reduction decreases while the induced pressure losses decreases the efficiency of the cycle. In [74], a $s - CO_2$ recompression cycle with a two recuperators has been analyzed (see Fig. 1.8). The optimal range of Reynolds number and effectiveness is Re between $32000 - 42000$ and ϵ between $0.87 - 0.94$ from a bi-objective optimisation of heat exchanger volume and cycle efficiency using genetic algorithm.

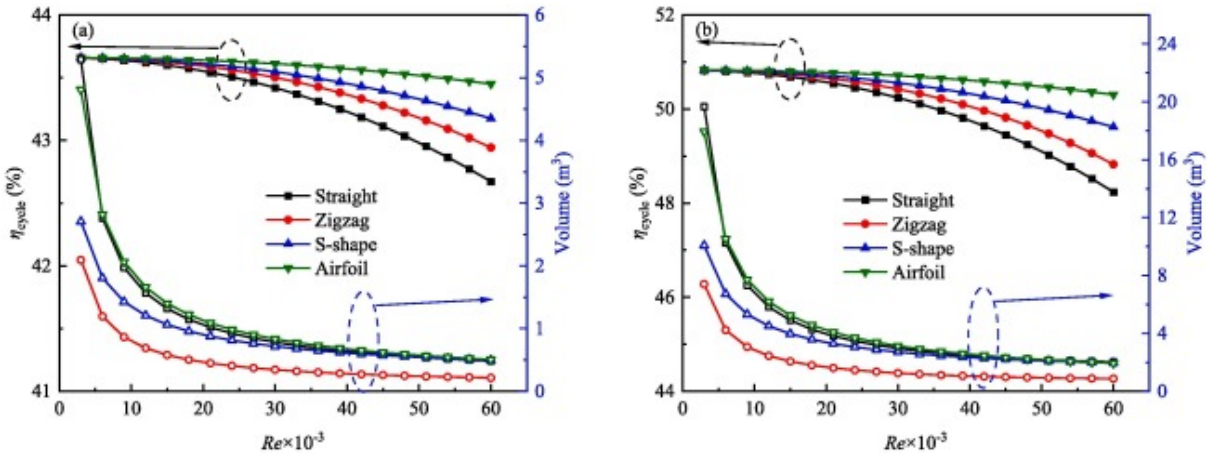

Figure 1.21: Effects of Reynolds number on the cycle efficiency and the PCHE volume. (a) $\epsilon = 0.75$, (b) $\epsilon = 0.95$ from [48]

1.4 Dynamic modeling

Because of the sensible properties exhibited by $s-CO_2$ and because of variation of waste heat load received by the bottoming cycle, the dynamic behavior of the cycle is not fully understood. Furthermore, the safe operation of the power block must be ensured by avoiding undesired phenomena such as compressor surge/choking, turbine choking, extreme CO_2 pressures and temperatures, extreme shaft rotational speeds, etc [53, 82]. There exist several approaches for dynamic modeling.

1.4.1 Dynamic models

Thermodynamic models

These kinds of models (also referred to as "white-box models" in [40]) are implemented when enough physical knowledge is known about the system. These models are based on physical laws. These are the constitutive equations, which are time-independent relations between two physical quantities (e.g. isentropic compression/expansion) as well as the conservation equations, which are time-dependent relations that describe conservation of mass (continuity equation), momentum (motion equation) and energy (from the first law of thermodynamics) [43, 40]. This type of model enables an overview of various physical system parameters (such as pressure, temperature, etc) at various locations [29]. The complexity of physical models is directly connected to their temporal and spatial dependency [40].

Black-box models

Black-box models are based on a completely empirical approach when little knowledge is available about the physics of the system. The implementation of black-box models is usually done by supplying a performance map of experimental points as a function of operating conditions [64]. Black-box models are simply the functional relationships between system inputs and system outputs. By implication, black-box models are lumped together with parameter models. The parameters of these functions do not have any physical significance in terms of equivalence to process parameters such as heat or mass transfer coefficients, reaction kinetics, etc. This is the disadvantage of black box models compared to physical models. However, if the aim is to merely represent faithfully some trends in process behavior, then the black box modeling approach is very effective [95].

Important aspects of empirical modeling are data pre-conditioning, model complexity, model linearity and model extrapolation. The various black box or empirical modeling techniques are: partial least squares modeling, time series modeling, neural network modeling, fuzzy modeling and neuro-fuzzy modeling. Process behavior is usually non-linear. Whether or not the empirical model to be developed should also be non-linear depends on the operating range in which the model will be used [80].

Hybrid models

Grey-box models combine the advantages of white-box and black-box methods to maximize their accuracy. This is done by the introduction of performance maps for turbomachinery as well as correlations for heat transfers of the heat exchangers (recuperator, waste heat recovery unit, etc) and for the pressure losses in the case of turbine modeling [40].

Such models were used by Henke et *al.* [31] whose approach is a lumped parameter model

approach. Its purpose is to achieve high simulation speed. Following this approach, it is assumed that all properties are homogeneous within a component, such as temperature of a gas volume or casing part. The recuperator being an exception, as its temperature profile is discretized in flow direction. The idea of the lumped model is to characterise the processes in the gas turbine with the steady-state values. They are characterised by a continuous progression along the steady-state curves. This is also considered as a quasi-static behaviour [29, 34].

This hybrid approach is now typical for mGT modeling [40].

1.4.2 Control

In order to achieve stable operation of the $s - CO_2$ cycle and optimize the recuperated power despite a variation of the waste heat load, the implementation of a control system is essential. The first objective of the control system is to guarantee the operational stability of the compressor by regulating the compressor inlet conditions. Then the power output of the cycle can be controlled through the Turbine Inlet Temperature (TIT) and compressor inlet temperature.

For mGT's the cycle efficiency increases as the turbine inlet temperature increases. The control strategy consist in keeping the TIT at a set temperature. For waste heat recovery bottoming cycles, the TIT is mostly imposed by the flue gas from the mGT used as a heat source.

The principal difficulty with the control of $s - CO_2$ cycle is the non-ideal behaviour of the fluid close to the critical point [63, 82]. Recall that the characteristics of CO_2 vary rapidly close to the critical point as seen in density variations which are shown on Fig. 1.3. As said earlier, in order to maximize the power output, the Compressor Inlet Temperature (CIT) should be kept as low as possible [2]. Indeed, thanks to liquid-like compressibility near the critical point, the needed work at the compressor is reduced. The compressor must perform less work to compress a more dense fluid. Reducing the lower temperature of a cycle also increases its efficiency. The density is largely sensitive to a change in the temperature at the compressor inlet. A change in CIT induces a change in pressure ratio. A large density change in the compressor has two disadvantage: it changes significantly the compressor performances, inducing pressure spikes in the system and could lead to compressor failure [82].

Low temperature control is the control of the inlet of the compressor temperature [82]. It is done by controlling the cold heat source mass flow rate in [2, 53, 63, 82], or using a compressor bypass.

To control the performances of the cycle, the most promising strategy seems to be the inventory control. The control variable is the mass of working fluid in the cycle, impacting the density of the working fluid. It allows part load operation while maintaining cycle efficiency. During power reduction, part of the working fluid is removed from the cycle, reducing its density. This leads to a reduction in pressure and mass flow rate. It can be done using two storage tanks as in [53] to remove mass of CO_2 at the high pressure side or add some at the lower pressure side. A reduction of the mass flow rate decreases the maximum pressure and without inventory control the minimum pressure increases to compensate the density reduction in the high pressure side [2].

This strategy maximizes the power output at part at 50 to 90 % of the nominal power according to Moisseytsev et *al.* [57]. This range of operating condition fits well our application. It shows a limited degradation of the turbine isentropic efficiency compared to a control strategy only based on the turbine rotation speed. Indeed, at constant rotational speed, the fluid velocity remains fairly constant so the isentropic efficiency remains relatively the same [82]. This experimental facility uses low temperature control by varying the mass flow rate of water at the cold heat exchanger. An inventory tank is also placed before the compressor to reduce the changes in pressure and prevent instability in compressor operations. A drawback of inventory control is the modification of the lower pressure of the cycle.

Most of the controllers investigated for the control of $s - CO_2$ cycles use Proportional-Integral (PI) or Proportional-Integral-Derivative (PID) controllers. The PI controller achieves a non-steady-state error and has a reduced sensitivity to high frequency disturbance [51, 53, 82].

1.5 Conclusion

With regard to matters expressed in this literature review, one finds the interest in evaluating the dynamic behavior of a $s - CO_2$ receiving transient heat load from a mGT. It allows future research on the control or optimisation of such cycle, and it is important to assess the stability of turbomachines during transient operations.

Special interest lies in the modeling of the compressor near the critical point and the heat exchangers (in particular the recuperator) especially in off-design conditions due to the varying properties of supercritical CO_2.

CHAPTER 2

Potential of CO_2 bottoming cycle

2.1 Introduction

To first investigate and estimate the gain of the addition of a CO_2 bottoming cycle, we first made a steady-state analysis. For this, we compared two CO_2 cycles with different starting states with two ORC's with organic fluids compatible with the temperature range of the mGT considered. The CO_2 cycles are composed of one Brayton cycle where the fluid is supercritical at any point of the cycle, and one Rankine cycle where the fluid is in supercritical conditions during the heat addition process but where the heat rejection phase happens in subcritical conditions. The ORC's are both Rankine cycles where any state of the fluid is in subcritical conditions.

2.2 Thermodynamic cycle

The cycle considered here is the Simple Recuperated Cycle as shown in Fig. 2.1. The fluid going out of the compressor is pre-heated (going from State 2 to State 3) before entering the Waste Heat Recovery Unit (WHRU) by the fluid going out of the turbine (going from State 5 to State 6). For the ORC's, with their entry being below the critical point, the compressor is replaced by a pump since the fluid is in liquid state. For a transcritical CO_2 Brayton cycle, the pressurizing component would still be a compressor since the entry of the compressor would be in gaseous state. However, in the case here investigated, for the $t - CO_2$ Rankine cycle, both compressor and pump terminology are valid. Indeed, the distinction between pumps and compressor in CO_2 applications is not distinct since the fluid densities are high for liquid, gas, and supercritical fluid states [4].

For the following analysis, the heat flux coming out of the heat source is imposed. We know from [40], that the exhaust temperature is about $T_{exh,in} \approx 270\,[°C]$ and the mass flow rate of the flue gas of the Turbec T100 is about $\dot{m}_{exh} \approx 0.79\,[kg/s]$ and that the fuel/air equivalent ratio is about $\phi = 0.13\,[-]$ (which gives an excess air coefficient $\lambda = \frac{1}{\phi} \approx 7.7\,[-]$). Furthermore, from [5], we know that the minimum temperature of the gas turbine exhaust gases at the exhaust stack is limited to avoid the cold-end corrosion issues in the exhaust stack and too much cooling would limit the preheating done by the recuperator. A trade-off must

be thus found and the choice was made to cool down the exhaust gases to $T_{out} = 135\,[°C]$. From this, the heat flux from the hot source Q_h can be computed:

$$Q_h = \dot{m}_{exh}(h_{exh}(p_{amb}, T_{in}) - h_{exh}(p_{amb}, T_{out})) \tag{2.1}$$

These enthalpies were computed using *CoolProp* and the exhaust gases were assumed to be equivalent to air and at ambient pressure $p_{amb} = 1\,[atm]$. Indeed, the air excess being very high, we have a very lean mixture at the exhaust of the mGT, hence a mixture composition very close to air. With pure methane and complete combustion with air, N_2 and O_2 represent 96 % (in proportions close to air) of the molar and the mass composition of the exhaust gas making this approximation valid. This heat flux is thus equal to $Q_h = 109.4\,[kW]$.

Recall from the definition of enthalpy that

$$dh = \left(\frac{\partial h}{\partial T}\right)_p dT + \left(\frac{\partial h}{\partial p}\right)_T dp\,, \tag{2.2}$$

with

$$c_p = \left(\frac{\partial h}{\partial T}\right)_p\,. \tag{2.3}$$

For an ideal gas, the second term of the enthalpy expression is dropped hence

$$dh = c_p dT\,. \tag{2.4}$$

The exhaust flow considered in this analysis is approximated as air which itself can be approximated as a ideal gas. Hence when computing the exhaust enthalpy, one can write

$$h_{exh,i} = c_{p,exh} T_i\,, \tag{2.5}$$

whereas for CO_2 and the organic fluids (the working fluids in general represented by the subscript wf), pressure must be considered hence

$$h_{wf,i} = h_{wf}(p_i, T_i)\,. \tag{2.6}$$

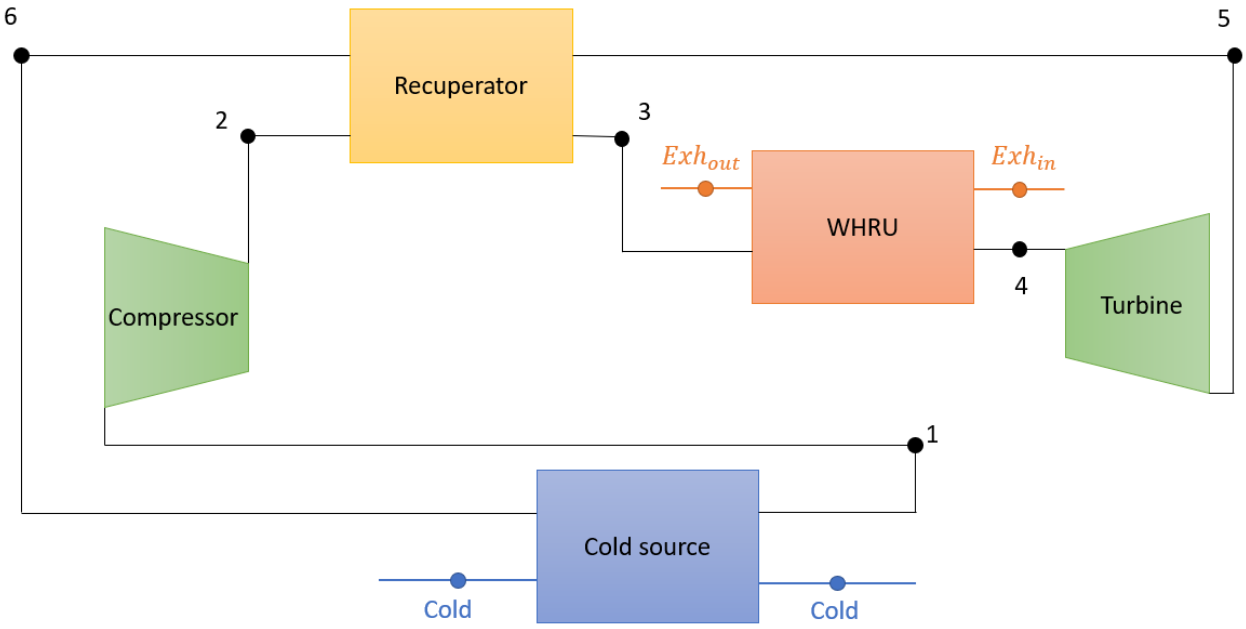

Figure 2.1: Simple Recuperated Cycle states and layout

For all the different cycles investigated, where a pinch temperature is imposed, its value is of $T_{pinch} = 10\,[°C]$. For every cycle, this pinch is imposed at the Recuperator outlet for the cold fluid ($T_6 = T_2 + T_{pinch}$). Thus, the enthalpy at the Recuperator outlet for the heated fluid can be computed as follows thank to energy conservation and the fact that the mass flow for the cold and hot fluid of this heat exchanger are the same:

$$h_{wf,3} = h_{wf,2} + (h_{wf,5} - h_{wf,6}) \tag{2.7}$$

From this value and the heat source heat flux, we can also compute the mass flow rate of the working fluid of the bottoming cycle $\dot{m}_{wf}$ assuming no heat losses:

$$\dot{m}_{wf} = \frac{Q_h}{h_{wf,4} - h_{wf,3}} \tag{2.8}$$

Furthermore, the cold source medium -water- (receiving the heat from State 6) is assumed to have constant temperature which should be equal according to [37] $T_{cold} = 12\,[°C]$. We also assume for this first analysis no heat losses in the different components and no pressure losses in the heat exchangers.

To compute the states in the compressor and the turbine, we used the isentropic efficiencies of the compressor ($\eta_{is,C}$) and of the turbine ($\eta_{is,T}$) and the states considering an isentropic compression ($h^s_{wf,2}$) and isentropic expansion ($h^s_{wf,5}$):

$$h_{wf,2} = h_{wf,1} + \frac{h^s_{wf,2} - h_{wf,1}}{\eta_{is,C}} \tag{2.9}$$

$$h_{wf,5} = h_{wf,4} - \eta_{is,T}(h_{wf,4} - h^s_{wf,5}) \tag{2.10}$$

2.2.1 $s - CO_2$ cycle

As explained in Section 2.1, in this cycle, CO_2 is in supercritical conditions at every state. This cycle is thus a Brayton cycle. The values of the isentropic efficiencies and fixed conditions of the cycle are shown in Tab. 2.1 and were determined according to [37]:

$\eta_{is,C}\,[-]$	$\eta_{is,T}\,[-]$	$T_1\,[°C]$	TIT $[°C]$	$p_1\,[bar]$	$p_2\,[bar]$
0.89	0.91	34	260	73.80	221.40

Table 2.1: $s - CO_2$ fixed steady-state cycle parameters

The initial conditions assure supercritical conditions at the inlet of the compressor. The pressure at the outlet of the compressor is bounded by the mechanical stresses that the mechanical structure can sustain; it is thus a technological constraint. The Turbine Inlet Temperature (TIT) is another fixed parameter in our analysis.

2.2.2 $t - CO_2$ cycle

This cycle, as said in Section 2.1, is very similar to the supercritical cycle except for its entry conditions hence for its heat rejection process which happens under subcritical conditions thus explaining the lower values in the initial conditions as shown in Tab. 2.2:

$\eta_{is,C}$ [−]	$\eta_{is,T}$ [−]	T_1 [°C]	TIT [°C]	p_1 [bar]	p_2 [bar]
0.89	0.91	24	260	64.34	221.40

Table 2.2: $t - CO_2$ fixed steady-state cycle parameters

The CO_2 passes through the two-phase region during the cooling process and is completely liquefied. A pump is thus used to pressurize the working fluid. A special matter in this cycle is thus the pinch point difficulty in the cooling section.

2.2.3 ORC's

Here we only consider classic Rankine cycles where all the states are in subcritical conditions as said in Section 2.1. There is thus evaporation of the working fluid during the heat addition and condensation during the cooling process leading to the pinch point problem. This leads to a significant mismatch of the two fluid states and generates a lot of irreversibility. Fig. 2.2 shows this problem during the heat addition process. Supercritical heat addition allows a better thermal match between working fluid and heat source due to its temperature glide [47].

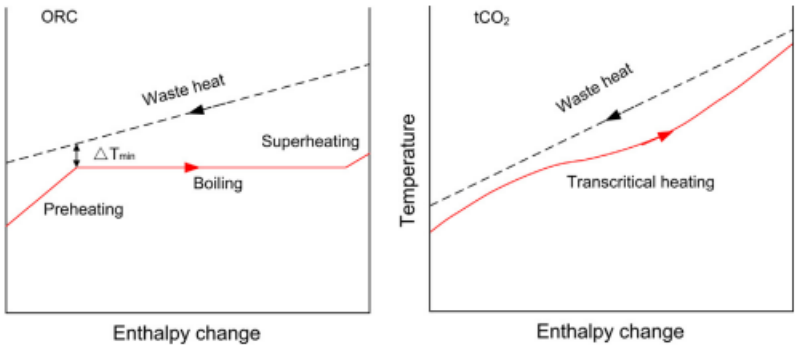

Figure 2.2: Temperature variation in the WHRU for ORC's and $t - CO_2$ cycles [86]

Considering the choice of the organic fluid, there are no strict rules for choosing the appropriate fluid, there are only some recommendations to follow. First, what is called a "dry" fluid is preferred (which is a fluid where $\frac{ds}{dt} > 0$) since it assures that the fluid will be only is gaseous state during the expansion as shown in Fig. 2.3c) on the contrary to wet fluids. For an ORC with lower operating temperatures, dry and isentropic fluids show better performances compared to the wet fluids [49].

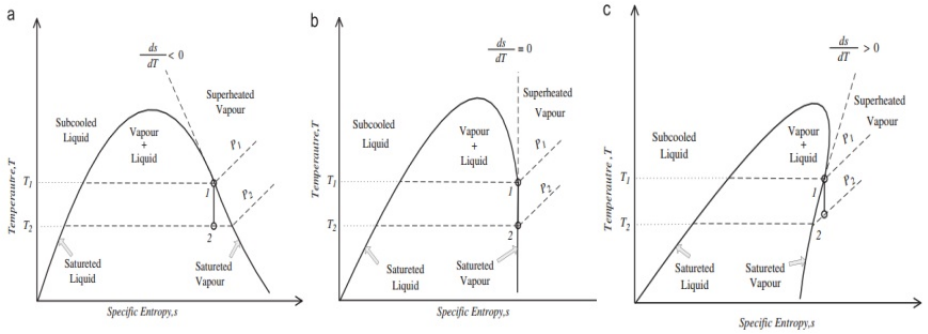

Figure 2.3: T-s diagram for (a) wet fluid (b) isentropic fluid (c) dry fluids [49]

Furthermore, the working fluid used in the cycle should be relevant to the temperature of the heat source. Indeed, a value of the critical temperature quite similar or slightly higher than the target evaporation temperature is suggested to simultaneously achieve good thermal matching between fluids and exhaust gas and to avoid excessively low vapour densities, which lead to increasing system cost [5]. Hence, the temperature at the TIT was set to TIT $= 0.97 \cdot T_{crit}$. And the maximum temperature achieved by the working should not exceed its thermal stability limit. It is better for cycle efficiency to have the critical temperature of the organic fluid close to the maximum temperature of the heat source. The freezing point of the organic fluid must be lower than the lowest temperature of the cycle [49]. Another indicator is the heat transfer capacity which determines the cost of the heat exchanger.

All of those things considered, R113 and R245fa are chosen as working fluids among those suitable for the temperature range of the thermal source for the low value of the latent heat of vaporization [69].

In regards to pressure, the cycle maximum pressure (obtained after the compressor) is limited to 90% of the critical pressure. Hence, the choice was made to limit the maximum pressure to $p_2 = 0.7 \cdot p_{crit}$. The minimum pressure however (condensing pressure) instead mainly depends on the cooling medium temperature [5]. This pressure is the saturation pressure at the condensation temperature. The state at the inlet of the compressor was considered to be saturated hence the temperature at this state is the condensation temperature which is defined by $T_1 = T_{cold} + T_{pinch}$. The isentropic efficiencies (again according to [37]) as well as the fixed parameters are summarized is Tab. 2.3 and Tab. 2.4 for R113 and R245fa respectively.

$\eta_{is,C}$ $[-]$	$\eta_{is,T}$ $[-]$	T_1 $[°C]$	TIT $[°C]$	p_1 $[bar]$	p_2 $[bar]$
0.86	0.91	22	85.33	0.40	23.75

Table 2.3: R113 fixed steady-state cycle parameters

$\eta_{is,C}$ $[-]$	$\eta_{is,T}$ $[-]$	T_1 $[°C]$	TIT $[°C]$	p_1 $[bar]$	p_2 $[bar]$
0.86	0.91	22	52.81	1.33	25.56

Table 2.4: R245fa fixed steady-state cycle parameters

2.3 Energetic and exergetic analysis

To compare the efficiencies of the cycles, we have to compare them on an energetic level as well as exergetic through different efficiencies showing a different aspect of the cycle. The method used is based on [33] treating power cycles. One should note that the subscript wf is dropped hence recall that $h_i = h_{wf,i} = h_{wf}(p_i, T_i)$ and the exhaust gas notation becomes $h_{exh,i} = h_{exh}(p_{amb}, T_i)$.

2.3.1 Energetic approach

- *Cycle efficiency:* η_{cyclen}
  Is defined as the ratio between the power cycle work and the calorific action undergone by the fluid at the hot source.

$$\eta_{cyclen} = \frac{(h_4 - h_5) - (h_2 - h_1)}{(h_4 - h_3)} \tag{2.11}$$

- *Waste Heat Recovery Unit efficiency:* η_{gen}
  Energetic efficiency involved in generating heat flow at the hot source using the flue gases at the exit of the mGT. It is assumed equal to unity; all the heat flux from the exhaust gases goes to the flow of CO_2. One should note that this efficiency was initially defined for Combustion Steam Cycles and Gas Turbine Cycles in [33] and not for waste heat recovery cycles where combustion is not directly involved in the cycle. This efficiency initially refers to the generation of heat flow at the hot source using primary power (thus referring to the amount of fuel used in the cycle and the Lower Heating Value of this fuel). Since combustion is not treated directly in the waste heat recovery cycle, this efficiency cannot be taken into account hence its value is put to unity.

$$\eta_{gen} = \frac{\dot{m}_{wf}(h_4 - h_3)}{\dot{m}_{exh}(h_{exh,in} - h_{exh,out})} \tag{2.12}$$

- *Mechanical efficiency:* η_{mec}
  Assumed equal to 0.97 for the moment (since we don't know the components yet).

$$\eta_{mec} = \frac{P_e}{\dot{m}_{wf}((h_4 - h_5) - (h_2 - h_1))} \tag{2.13}$$

- *Total efficiency:* η_{toten}
  Product of all the 3 previous efficiencies; allows us to know the power production of the considered cycle.

$$\eta_{toten} = \frac{P_e}{\dot{m}_{exh}(h_{exh,in} - h_{exh,out})} = \eta_{cyclen} \cdot \eta_{gen} \cdot \eta_{mec} \tag{2.14}$$

2.3.2 Exergetic approach

The exergetic approach offers a way to examine the degree of perfectibility of a transformation, it adds a quality factor to energy tied to its thermal level. The exergy method does not award the same value to all types of energy which are added and subtracted in energy balance (irreversibilities generate less entropy when the fluid is at high temperature). The exergy is thus defined as:

$$\Delta e = \Delta h - T_0 \cdot \Delta s \tag{2.15}$$

With T_0 equal to the temperature at the cold source (considered constant): $T_0 = T_{cold} = 12\,[°C]$.

There are several origins of the irreversibilities in a power cycle:

1. Occurring during heat exchanges between working fluid and the heat carrying fluids at the hot source, the cold source and the recuperator.

2. Due to a finite conductibility which implies a non-zero temperature gradient to ensure heat transfer.

3. From the losses due to mixing of identical/different substances at identical or not pressure and/or temperature.

4. Due to viscous dissipation degrading mechanical energy (in particular kinetic energy in turbomachinery).

5. From friction between contacting surfaces

The different exergetic effiencies are thus defined as follows:

- *Cycles efficiency:* η_{cyclex}
  Ratio of work produced to the exergetic content of the calorific action provided by the hot source.
  $$\eta_{cyclex} = \frac{(h_4 - h_5) - (h_2 - h_1)}{(e_4 - e_3)} \tag{2.16}$$

- *Rotationg apparatus efficiency:* η_{rotex}
  Viscous dissipation occurring during expansion/compression. This efficiency is expressing that the value of the loss of enthalpy occurring in the turbine is worth less than loss of exergy in the turbine. And that the value of the gain of enthalpy in compressor is higher than gain of exergy in the compressor.
  $$\eta_{rotex} = \frac{(h_4 - h_5) - (h_2 - h_1)}{(e_4 - e_5) - (e_2 - e_1)} \tag{2.17}$$
  With this definition, η_{cyclex} can be re-written as:
  $$\eta_{cyclex} = \eta_{rotex} \frac{(e_4 - e_5) - (e_2 - e_1)}{(e_3 - e_2)} \tag{2.18}$$

- *Heat transfer efficiency:* $\eta_{transex}$
  Exergetic efficiency of the heat transfer between the flue gases and the working fluid in the waste heat recovery unit. It expresses the irreversibility of energy transfer in a heat exchanger; it amounts to the ratio between the increase in exergy flow rate of the heated fluid and the decrease in exergy flow rate of the heating fluid.
  $$\eta_{transex} = \frac{\dot{m}_{wf}(e_4 - e_3)}{\dot{m}_{exh}(e_{exh,in} - e_{exh,out})} \tag{2.19}$$

- *Chimney efficiency:* $\eta_{chimnex}$
  Expressing the amount of exergy left at the chimney after the heat transfer with the working fluid. The reference exergy used e_r is equal to the exergy at the reference temperature T_0. Again, this efficiency was defined for cycles with combustion hence its name (kept the same for simplicity).
  $$\eta_{chimnex} = \frac{e_{exh,in} - e_{exh,out}}{e_{exh,in} - e_r} \tag{2.20}$$

- *Waste Heat Recovery efficiency:* η_{gex}
  Product of the heat transfer and chimney efficiencies; accounts for the loss of exergy due to the difference of temperature between the hot and cold fluid (the smaller the mean difference, the smaller the loss) as well as the non-zero exergy of the flue gases at the chimney.

$$\eta_{gex} = \frac{\dot{m}_{wf}(e_4 - e_3)}{\dot{m}_{exh}(e_{exh,in} - e_r)} = \eta_{transex} \cdot \eta_{chimnex} \tag{2.21}$$

- *Total efficiency:* η_{totex}
  Product of the mechanical, cycle and WHRU efficiencies; it amounts to the ratio of the effective power produced within the plant to the primary exergetic power (here coming from the exhaust gas from the mGT).

$$\eta_{totex} = \frac{P_e}{\dot{m}_{exh}(e_{exh,in} - e_r)} = \eta_{cyclex} \cdot \eta_{gex} \cdot \eta_{mec} \tag{2.22}$$

2.4 Effectiveness

For the heat transfer, we use the metric of effectiveness. It is defined by the ratio of the heat exchanged in the heat exchanger by the maximum heat that could be exchanged in the heat exchanger (if its area was infinite):

$$\epsilon = \frac{Q}{Q_{max}} = \frac{Q}{C_{min} \cdot \Delta T_{max}} \tag{2.23}$$

Where $C_{min} = min(\dot{m}_h c_{p,h}, \dot{m}_c c_{p,c})$ and ΔT_{max} represents the maximal temperature difference that could exist if the heat exchanger was of infinite area, this temperature difference being achieved by the fluid (heated or heating) undergoing the biggest temperature difference between the two fluids hence the definition of C_{min}. The temperature profile (assuming constant heat capacity for the cold and hot fluid) are shown in Fig. 2.4 and 2.5 considering a counter flow heat exchanger.

In this case, $\Delta T_{max} = T_{h,in} - T_\infty$.

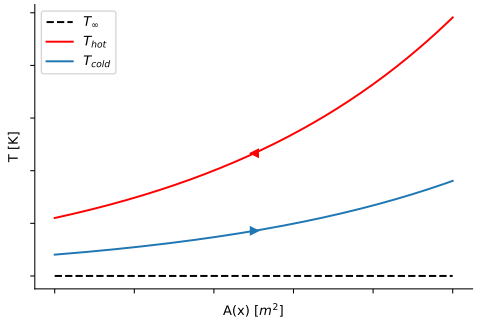

Figure 2.4: Heat exchanger temperature profile example - $\dot{m}_c c_{p,c} > \dot{m}_h c_{p,h}$

In this case, $\Delta T_{max} = T_\infty - T_{c,in}$.

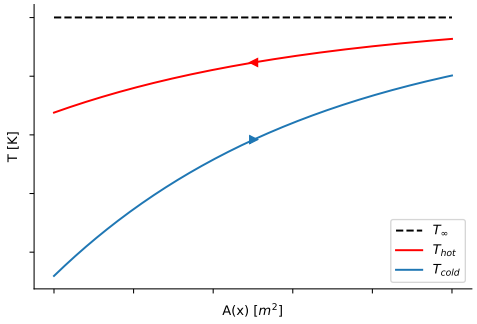

Figure 2.5: Heat exchanger temperature profile example - $\dot{m}_h c_{p,h} > \dot{m}_c c_{p,c}$

This example holds for a perfect gas (ideal gas with constant heat capacity hence $dh = c_p dT$). In the case of a real gas as it is the case for the working fluids the effectiveness are defined hereunder.

- **Recuperator**
  The heat exchanged Q_{recup} is defined as:

$$Q_{recup} = \dot{m}_{wf}(h_{wf}(p_5, T_5) - h_{wf}(p_6, T_6)) = \dot{m}_{wf}(h_{wf}(p_3, T_3) - h_{wf}(p_2, T_2)) \tag{2.24}$$

  The maximum heat exchanged possible between the heated and heating fluid in the Recuperator if its area was infinite is expressed as follows:

$$Q_{max,recup} = \dot{m}_{wf}(\Delta h_i)_{min}\,, \tag{2.25}$$

  where $(\Delta h_i)_{min}$ is defined as the minimum enthalpy difference of the fluid i (heated or heating) to achieve the desired maximum temperature difference possible $(T_5 - T_2)$. This minimum is only put on the enthalpy difference due to the same value of mass flow rate for the heated and heating fluid. $(\Delta h_i)_{min}$ is equal to:

$$(\Delta h_i)_{min} = min\left[h_{wf}(p_5, T_5) - h_{wf}(p_5, T_2), h_{wf}(p_2, T_5) - h_{wf}(p_2, T_2)\right] \tag{2.26}$$

  Hence, the effectiveness can be expressed as:

$$\epsilon_{recup,1} = \frac{h_{wf}(p_5, T_5) - h_{wf}(p_6, T_6)}{h_{wf}(p_5, T_5) - h_{wf}(p_5, T_2)} = \frac{h_{wf}(p_3, T_3) - h_{wf}(p_2, T_2)}{h_{wf}(p_5, T_5) - h_{wf}(p_5, T_2)}\,, \tag{2.27}$$

  when $(\Delta h_i)_{min} = \Delta h_h$, or

$$\epsilon_{recup,2} = \frac{h_{wf}(p_5, T_5) - h_{wf}(p_6, T_6)}{h_{wf}(p_2, T_5) - h_{wf}(p_2, T_2)} = \frac{h_{wf}(p_3, T_3) - h_{wf}(p_2, T_2)}{h_{wf}(p_2, T_5) - h_{wf}(p_2, T_2)}\,, \tag{2.28}$$

  when $(\Delta h_i)_{min} = \Delta h_c$.

- **Heat source**
  The heat exchanged Q_{hot} is expressed as:

$$Q_{hot} = \dot{m}_{exh}(h_{exh}(T_{in}) - h_{exh}(T_{out})) = \dot{m}_{wf}(h_{wf}(p_4, T_4) - h_{wf}(p_3, T_3)) \tag{2.29}$$

  The exhaust is always evaluated at p_{amb} hence the simplification of notation by not including pressure (also, this can be neglected in the case of ideal gas assumption for air). The maximum possible heat exchanged for the waste heat recovery unit is thus expressed as follows:

$$Q_{max,hot} = (\dot{m}_i \Delta h_i)_{min}\,, \tag{2.30}$$

  where $(\dot{m}_i \Delta h_i)_{min}$ is defined as the minimum heat flux difference of the fluid i (heated or heating) to achieve the desired maximum temperature difference possible $(T_{in} - T_3)$. The value of $(\dot{m}_i \Delta h_i)_{min}$ is thus equal to:

$$C_{min} = min\left[\dot{m}_{exh}(h_{exh}(T_{in}) - h_{exh}(T_3)), \dot{m}_{wf}(h_{wf}(p_3, T_{in}) - h_{wf}(p_3, T_3))\right] \tag{2.31}$$

  Hence the effectiveness also is defined according to two definitions:

$$\epsilon_{hot,1} = \frac{h_{exh}(T_{in}) - h_{exh}(T_{out})}{h_{exh}(T_{in}) - h_{exh}(T_3)}\,, \tag{2.32}$$

  when $(\dot{m}_i \Delta h_i)_{min} = \dot{m}_h \Delta h_h$, or

$$\epsilon_{hot,2} = \frac{h_{wf}(p_4, T_4) - h_{wf}(p_3, T_3)}{h_{wf}(p_3, T_{in}) - h_{wf}(p_3, T_3)}\,, \tag{2.33}$$

  when $(\dot{m}_i \Delta h_i)_{min} = \dot{m}_c \Delta h_c$.

- **Cold source**
  The heat exchanged Q_{cold} is defined as:

$$Q_{cold} = \dot{m}_{wf}(h_{wf}(p_6, T_6) - h_{wf}(p_1, T_1)) \tag{2.34}$$

  Because of to the constant temperature cold source $C_c = C_{max} \longrightarrow \infty$, the maximum heat exchange becomes:

$$Q_{max,cold} = \dot{m}_{wf}(h_{wf}(p_6, T_6) - h_{wf}(p_6, T_{cold})). \tag{2.35}$$

  The effectiveness is thus expressed as:

$$\epsilon_{cold} = \frac{h_{wf}(p_6, T_6) - h_{wf}(p_1, T_1)}{h_{wf}(p_6, T_6) - h_{wf}(p_6, T_{cold})} \tag{2.36}$$

2.5 Results and discussion

A summary of the different energy and exergy efficiencies for the different cycles analyzed is shown in Tab. 2.5. One can note that η_{gen}, η_{mec} and $\eta_{chimnex}$ are not present. As explained in Section 2.3.1, the value of η_{gen} was put to one in all the cycles. Also, the mechanical efficiency was assumed identical for each cycle and its value is $\eta_{mec} = 0.97\,[-]$. Furthermore, the chimney efficiency are the the same for each cycle as seen in equation (2.20) since the heat flux is imposed and identical for each cycle. Its value for each cycle is thus $\eta_{chimnex} = 0.724\,[-]$.

	η_{cyclen}	η_{toten}	η_{cyclex}	η_{rotex}	$\eta_{transex}$	η_{gex}	η_{totex}
$s - CO_2$	0.200	0.195	0.525	0.812	0.964	0.698	0.355
$t - CO_2$	0.247	0.240	0.716	0.890	0.870	0.630	0.437
R113	0.266	0.258	0.826	0.921	0.812	0.588	0.471
R245fa	0.195	0.189	0.797	0.912	0.617	0.447	0.346

Table 2.5: Energetic and exergetic efficiencies for the CO_2 and organic steady-state cycles

One can observe a globally low energetic cycle and total efficiency for all the cycles and especially for $s - CO_2$ and R245fa, the R113 cycle being the best. Furthermore, the exergetic cycle efficiency of the $s - CO_2$ is the lowest amongst all the cycles, which makes it the most penalizing parameter for the total exergetic efficiency for this cycle. This efficiency is higher in the case of $t - CO_2$ but still slightly below the values achieved for the ORC's which are very close to one another. This comments also justify the values obtained for the rotating apparatus efficiency.

As for the heat exchange at the hot source, the R245fa cycle possesses the lowest efficiency. In the case of this cycle, this is thus the most penalizing parameter for the total exergetic efficiency. This is also the case for the R113 cycle which has the second lowest heat exchange efficiency for the waste heat recovery unit. The $t - CO_2$ cycle possesses moderate performances for both the cycle and heat exchange exergetic efficiency even if the impact of the heat exchange efficiency has greater impact on the total efficiency as for the ORC's.

As for the different heat exchangers effectiveness (waste heat recovery unit, recuperator, cold source), their values are summarized in Tab. 2.6.

	$\epsilon_{hot,1}$	$\epsilon_{recup,1}$	ϵ_{cold}
$s-CO_2$	0.972	0.765	0.472
$t-CO_2$	0.764	0.868	0.832
R113	0.651	0.845	0.946
R245fa	0.583	0.669	0.940

Table 2.6: Effectiveness for the CO_2 and organic steady-state cycles

The hot source and recuperator effectiveness are both defined (and for all the cycles considered) according to the first definition given for their effectiveness, i.e. equation (2.32) and equation (2.27) meaning the heating fluid will perform the minimum heat flux to achieve the maximum temperature difference possible in the heat exchange. In the case of $t-CO_2$, this might not seem obvious due to the temperature profiles expressed in Fig. 2.7, but if the exhaust was cooled further down, the pinch temperature would tend to be located at the left of Fig. 2.7 after enough cooling of the exhaust. In the case of the recuperator, the definition expressed in equation (2.27) is used because the specific enthalpy at constant pressure of CO_2 and the organic fluids is lower at higher pressure for a given temperature (the specific heat at constant pressure shows the same trend for CO_2 but not in the case of the organic fluids where it is the opposite). Hence, since the mass flow rate is the same on both sides of the exchanger, the heating fluid experiences the sharpest temperature changes as seen in Fig. 2.6.

The effectiveness at the hot source is descending with each cycle investigated. A high value for this effectiveness suggests a high area for the heat exchanger since the exchanged heat at the hot source is known and is equal for all cycles (recall, from equation (2.1), we computed $Q_h = 109.4\,[kW]$). Hence for both CO_2 cycles, the WHRU should possess a higher area than for the ORC's which is economically penalizing. However, a high effectiveness for the hot source is advantageous because it suggest close mean temperatures between the heated and heating fluid hence a high heat exchange exergetic efficiency as seen in the values of $\eta_{transex}$ in Tab. 2.5. This confirms the efficiency performances regarding the heat exchanges.

As for the recuperator, the imposed temperature of the exhaust at the exit of the WHRU limits the preheating needed by the working fluid before entering the WHRU. This impacts the effectiveness of the recuperator. Indeed, the $s-CO_2$, starting from a higher compressor outlet temperature (COT), is in less need for preheating than the $t-CO_2$ cycle hence a lower recuperator effectiveness. For the ORC's, their COT is about the same, but the enthalpy at constant pressure is lower in the case of R113 allowing for a higher temperature change in the recuperator hence a higher recuperator effectiveness.

Also, the effectiveness of the recuperator influences the heat given at the cold source due to the enthalpy left at the recuperator outlet on the hot side. For $s-CO_2$, since the value of the working fluid at this heat exchanger is relatively high due to the inlet conditions at the compressor inlet and because of a moderate recuperator effectiveness, a small value of effectiveness is obtained for the cold source. The effectiveness at the cold source increases sharply when considering $t-CO_2$ because of the increase of recuperator effectiveness, the subcritical compressor inlet conditions and because of the condensation process when heat is rejected at constant temperature. The same can be said for the ORC's (except for the recuperator effectiveness of the R245fa). This high effectiveness again suggest a high heat exchanger area this case in favor of the $s-CO_2$ cycle.

2.5.1 Heat exchanger temperature profiles

The temperature profiles in the heat exchangers are show on Fig. 2.6, Fig. 2.7 and Fig. 2.8.

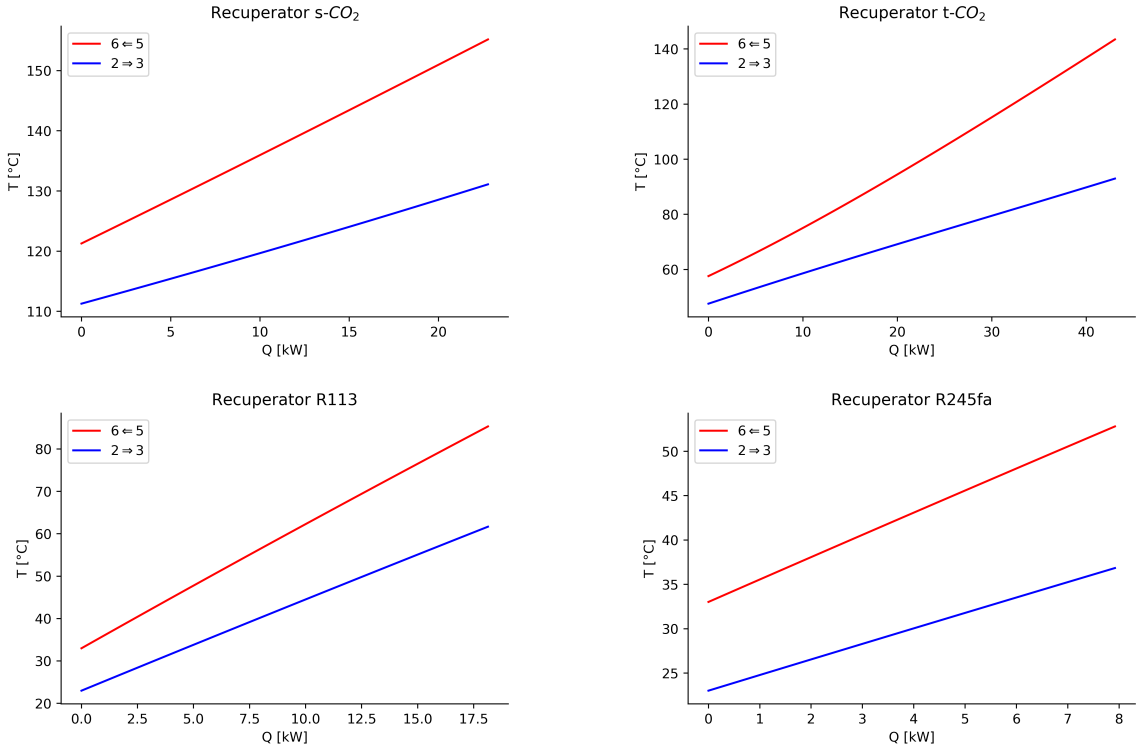

Figure 2.6: Temperature profiles in the recuperator for the steady-state cycles

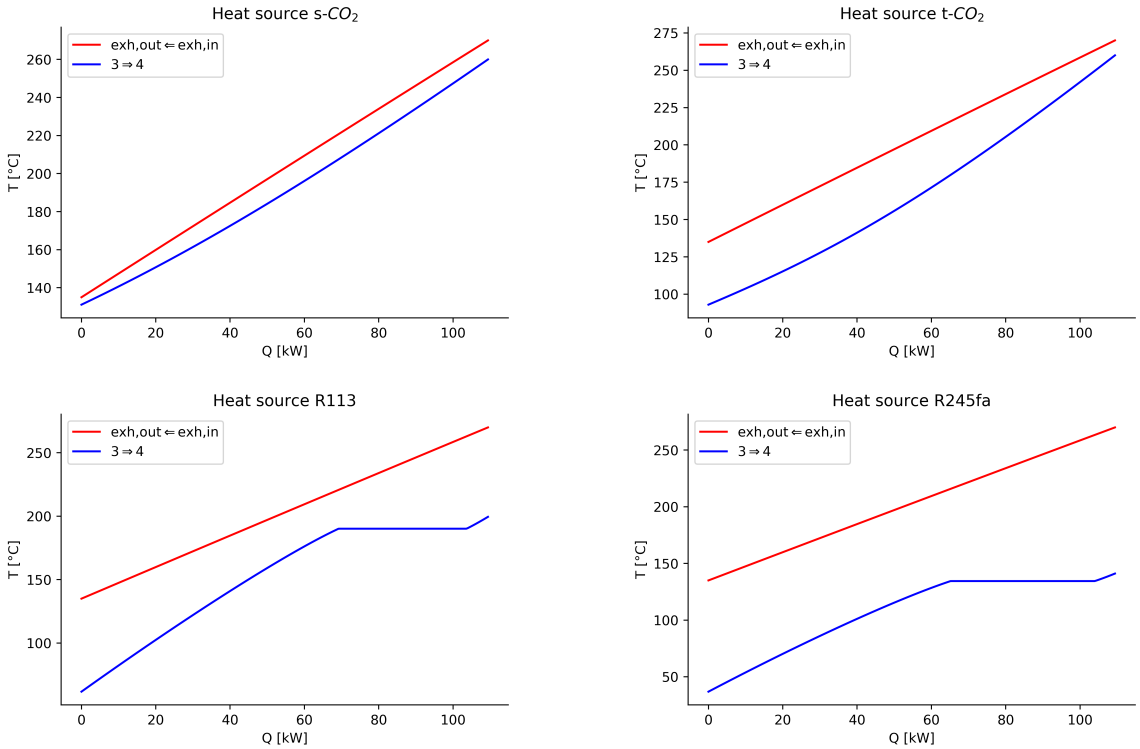

Figure 2.7: Temperature profiles in the WHRU for the steady-state cycles

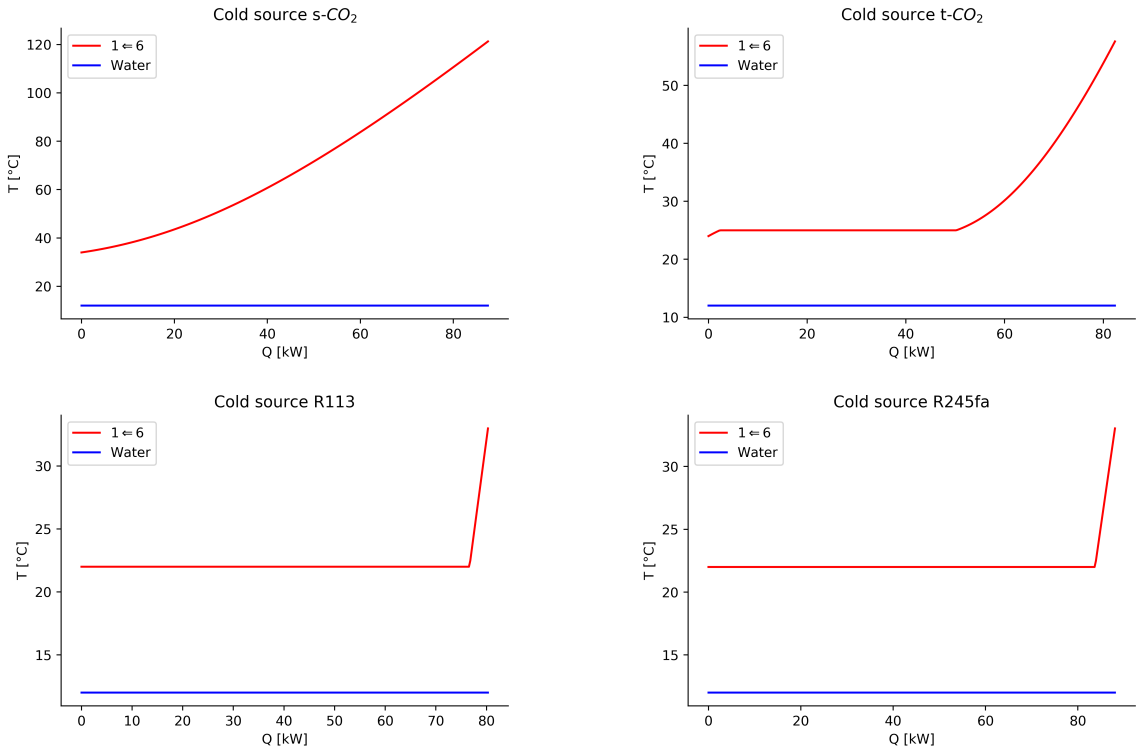

Figure 2.8: Temperature profiles at the cold source for the steady-state cycles

These graphs confirm what was said about the efficiencies and effectiveness. One can observe the condensation and evaporation happening at constant temperature for the Rankine cycles that limit the temperature glide of the working fluid.

2.5.2 T-s diagrams

The Temperature-Entropy diagram of the four different cycles are shown on Fig. 2.9. The reason of the poor cycle efficiency presented by the $s-CO_2$ cycle can be seen in these diagrams. Indeed, the high temperature difference between the inlet and outlet of the compressor suggest a higher compressor consumption because of the decreased density at the compressor inlet in the case of the $s-CO_2$ compared to the other cycles. This is in line with what was said in Section 1.2.1 that show that $s-CO_2$ can show liquid-like or vapour-like behavior. In this case, the compressor works in the vapour-like region decreasing the cycle efficiency because of increased power needed for the compressor. To limit this power consumption, one could work closer to the liquid-like region by lowering the CIT and/or increasing the CIP. However, increasing the pressure could result in the need of lowering the pressure ratio because of mechanical stresses resulting in lower cycle efficiency.

A summary of the compressor/pump power consumption $P_{c,i}$, the effective power produced $P_{e,i}$ and the mass flow rate in the cycle $\dot{m}_i$ for the i^{th} fluid is shown on Tab. 2.7. One can see a huge decrease in compressor power consumption between the $s-CO_2$ and $t-CO_2$ cycles for a relatively same turbine enthalpy drop (as seen on Fig. 2.10). The ORC's have very small pump power consumption due their liquid state. The mass flow rate are relatively similar. However, as seen on equation (2.8), the CO_2 mass flow rate increases in the $s-CO_2$ cycle because the specific enthalpy slope at constant pressure decreases at higher temperatures as seen on Fig. 2.11(a). For the ORC's, the slope of the enthalpy at constant pressure in the range of temperature considered is higher for R245fa than for R113 resulting in lower mass

flow rate for R245fa as seen on Fig. 2.11(b).

	$P_{c,i}\,[kW]$	$P_{e,i}\,[kW]$	$\dot{m}_i\,[kg/s]$
$s-CO_2$	24.37	21.30	0.57
$t-CO_2$	8.98	26.23	0.40
R113	0.87	28.25	0.50
R245fa	0.91	20.72	0.43

Table 2.7: Compressor/pump power consumption, effective power and mass flow rates for the CO_2 and organic steady-state cycles

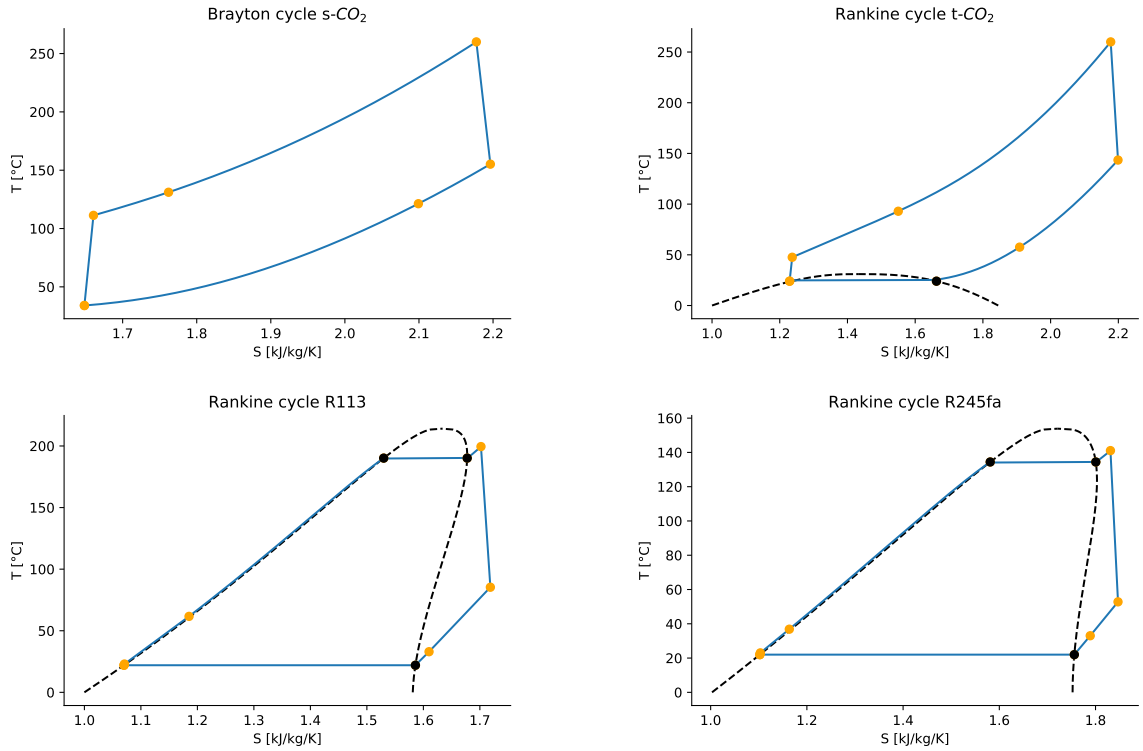

Figure 2.9: Temperature-Entropy diagrams for the CO_2 and organic steady-state cycles

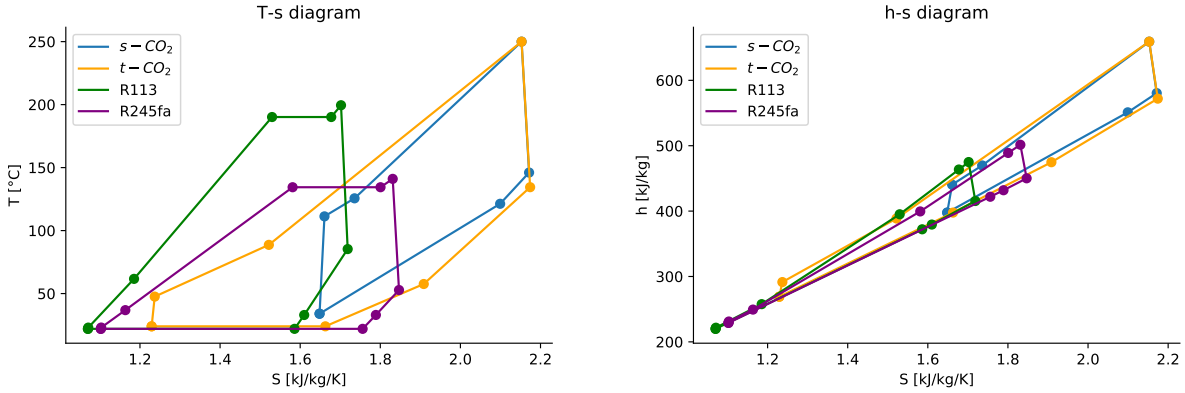

Figure 2.10: T-s and h-s diagram for the CO_2 and organic steady-state cycles

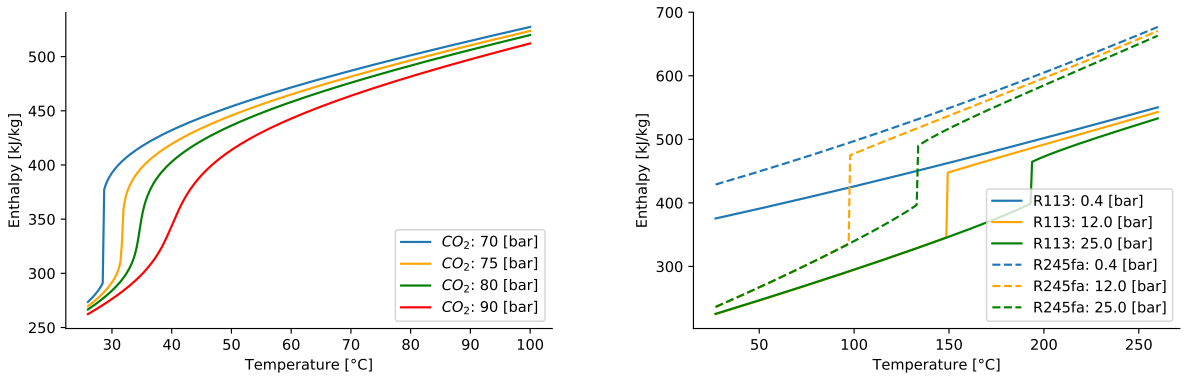

Figure 2.11: Specific enthalpies in function of temperature
(a) CO_2, (b) R113 and R245fa

2.5.3 Power losses

A summary of the exergetic losses decomposed into the main terms that make up the total exergetic losses as seen in equation (2.22) is shown graphically in Fig. 2.12. These losses are expressed according to the following expressions based on the exergetic efficiencies from the equations (2.13), (2.16), (2.21) and (2.22):

$$P_{L,mec} = \dot{m}_{wf}((h_4 - h_5) - (h_2 - h_1)) - P_e \tag{2.37}$$

$$P_{L,cyclex} = \dot{m}_{wf}((e_4 - e_3) - ((h_4 - h_5) - (h_2 - h_1))) \tag{2.38}$$

$$P_{L,gex} = \dot{m}_{exh}(e_{exh,in} - e_r) - \dot{m}_{wf}(e_4 - e_3) \tag{2.39}$$

$$P_{L,totex} = \dot{m}_{exh}(e_{exh,in} - e_r) - P_e = P_{L,mec} + P_{L,cyclex} + P_{L,gex} \tag{2.40}$$

The sum of these losses with the effective power P_e make up the total power P_{tot}. How many percent make up each of these losses and power of the total power of the considered cycle is what is shown in Fig. 2.12.

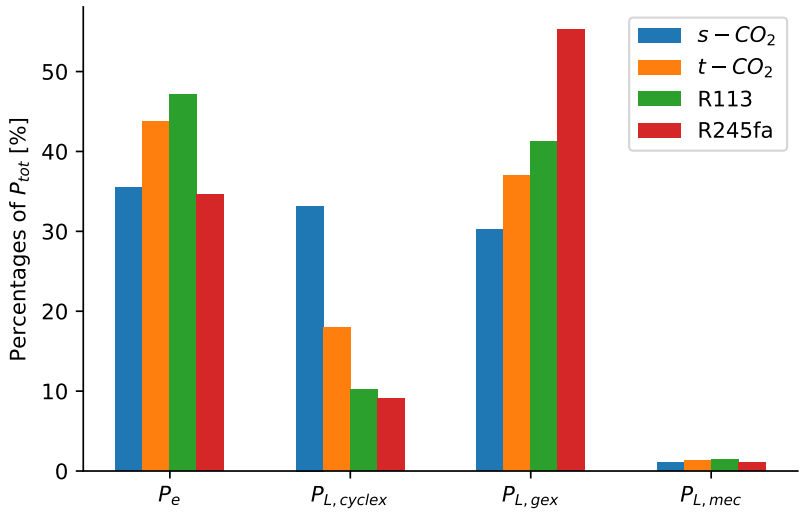

Figure 2.12: Effective power and power losses for the CO_2 and organic steady-state cycles

This figure confirms what was discussed in Section 2.5 about where the losses came from; mainly from the cycle for the $s-CO_2$ cycles and from the heat transfer for the ORC's and $t-CO_2$. Especially, because of the lower critical temperature of R245fa limiting its TIT, the mean temperature difference between the exhaust gas and heated working fluid is the highest amongst all the cycles hence exhibits the worse thermal performances.

2.6 Conclusion

To conclude this chapter, this analysis has shown the interest of using supercritical/transcritical CO_2 cycles in the context of waste heat recovery. The performances of the CO_2 cycles have proven to be of the same order of magnitude compared to the ORC's (which are the main technology used for waste heat recovery for the time being). But they need higher waste heat recovery heat exchanger surface inducing higher costs which is especially economically penalizing since this component has a high specific investment cost. However, as stated in Chapter 1, ORC's present some disadvantages such as thermal stability (whereas CO_2 is a very stable component) and have a high global warming potential (GWP) compared to CO_2. More specifically, CO_2 is competitive with the ORC's thanks to its high density, non-toxicity, the fact that it is inexpensive and non-flammable and is abundantly available possibly provided by greenhouse gas sequesters [87, 5] Furthermore, Yoon et *al.* [93], highlighted that a CO_2 recuperated cycle has higher performances at part-load operations than a simple ORC. Other drawbacks of ORC's compared to $s-CO_2$ is their constant evaporation temperature, which increases irreversibly during the heat addition process when using sensible heat sources such as waste heat. In comparison, the supercritical heat addition process of a supercritical/transcritical cycle can produce high efficiency temperature matching between the sensible heat source and the working fluid, leading to no pinch limitations.

The transcritical cycle is more efficient but its implementation can be source of problems. In terms of the isothermal condensation, a special matter is the pinch point difficulty in the cooling section. If the temperature of the cooling water is given, the water mass flow of the cooling medium has to be increased, in the case of $t-CO_2$ cycle, to liquefy the CO_2 compared to the supercritical cycle [37]. Due to its low critical temperature, the condensation of CO_2 is a vital problem in practice. CO_2 power cycles have considerable potential for low-temperature heat recovery if the proper heat sink is available for example Liquefied Natural Gas (LNG) [94]. Furthermore, specifically for low-temperature transcritical cycles, experiments in literature are scarce and available results display poor performances mainly due to non-optimized turbomachinery [42]. Consequently, up till now, investigations on low temperature heat source energy conversion systems with transcritical CO_2 have been limited to small-scale laboratory work [46].

Lastly, one should note that the cycles were not optimized hence better performances could be achieved from them. However, the assumptions taken in a perspective of simplification (no pressure and heat losses) will deteriorate their performances certainly in a unequal way. Recall also that this is only a steady-state analysis. Furthermore, the pressure ratios between the ORC's and the CO_2 cycles are orders of magnitude different but this is supported by [37].

CHAPTER 3

Physical model

3.1 Introduction

In this Chapter, the physical model of the dynamic $s - CO_2$ cycle modeled will be presented. The methodology used for the modeling of transient operations consists in the decomposition of the different thermodynamic components into different blocks to identify their main purpose in the cycle. The different blocks (compressor, turbine, heat exchangers, shaft, controller, inventory tank) of the Simple Recuperated Cycle shown in Fig. 2.1 will be detailed as well as the methodology employed to model these blocks. With this, the different assumptions and the governing equations used in this model will naturally also be featured. For clarity, the numeration of the cycle states follows the same as the one used in the Simple Recuperated Cycle Fig. 2.1.

The cycle selected is thus the SRC, widely accepted as the most promising cycle layout for WHR at the range of temperature we are interesting in, between 200 and 300 $[°C]$ [1, 11], due to the good trade-off between efficiency and cost (associated with the complexity of the cycle), as explained in Section 1.2.3.

3.2 General assumptions

For model simplification purpose, some assumptions have been made. Their explanations and the justifications for their use will be expressed hereunder.

3.2.1 Pressure losses

Due to the limited compression ratio of $s - CO_2$ cycles, pressure losses have a significant impact on the cycle performances.

The Darcy–Weisbach equation (3.1) accurately models the regular pressure losses, i.e. the pressure losses due to the friction along the length of a pipe caused by the fluid viscosity. This is a general equation that can be used for all heat transfers.

$$\Delta p = f \frac{L}{d_h} \frac{\rho c^2}{2}, \tag{3.1}$$

with c the characteristic speed of the fluid in the pipe and f the friction factor that is not a constant and depends on the characteristics of the pipe (hydraulic diameter d_h and rugosity ϵ) as well as the the ones of the flow (velocity c and dynamic viscosity μ). There exists various correlations to express the friction factor as a function of the Reynolds number $Re = \frac{\rho c\, d_h}{\mu}$ and the relative roughness of the pipes $\frac{\epsilon}{d_h}$ with d_h the hydraulic diameter and ϵ the surface roughness of the pipe surface, introduced by Colebrook, Gnielinski,etc.

To represent singular losses (pressure losses due to recirculation zones) caused by a bending of the pipes or a change of direction of the flow, a coefficient for singular pressure losses ξ is introduced, allowing for a more general expression for the pressure losses.

$$\Delta p = (f \frac{L}{d_h} + \xi) \frac{\rho c^2}{2} \tag{3.2}$$

Pressure losses are physically connected to flow average velocity. Using the mass conservation equation, the Darcy-Weisbach equation can be expressed in term of mass flow (3.3)

$$\Delta p = (f \frac{L}{d_h} + \xi) \frac{\dot{m}^2}{2 A_e^2 \rho} \tag{3.3}$$

This physical model of the pressure losses requires a precise knowledge of the geometry of the installation and of the flow development. Due to the limited knowledge available for this analysis, this model cannot be used. A simpler model should then be used.

For both heating and cooling heat transfers in the field of $s - CO_2$, studies have been carried out to simplify this model. It showed that pressure drops are mostly affected by the inlet pressure P_{in} and the mass flow $\dot{m}$ [67]. Experimental study near the critical point shows that for temperature higher than the pseudo-critical temperature, pressure drops increases with increasing inlet pressure [19] and increasing mass flow. Equation (3.3) highlights the relation between pressure losses and the square of the mass flow. Consequently, head losses can be quantified using the following model:

$$p_{out} = (1 - \gamma\, \dot{m}^2) p_{in} \tag{3.4}$$

$$\Delta p = p_{in} \gamma\, \dot{m}^2 \tag{3.5}$$

This model express the relative pressure losses as a function of the mass flow rate across the pipes and heat exchangers by the term $(\gamma\, \dot{m}^2)$. It requires a tuning of the γ coefficient for all the components of interest. Due to the limited knowledge on the piping system of the installation, the pressure losses of the pipes will be neglected or comprised in the pressure losses considered in the heat exchangers. The γ coefficient will be determined based on the relative pressure losses used in articles with experimental data to validate their simulation. This tuning has been made for the heater, recuperator and cooler heat exchangers in Section 5.2.

3.2.2 Exhaust composition

The exhaust composition was computed using complete combustion with air (whose molar composition is of 21 % O_2 and 79 % N_2) equation with pure methane with excess air $\lambda = 7.7\,[-]$ (see Section 2.2). The molar composition of the exhaust is summarized in Tab. B.1.

O_2 %	N_2 %	H_2O %	CO_2 %
18	78	2.7	1.3

Table 3.1: mGT Exhaust composition

3.2.3 Leakage losses

No leakage of working fluid was considered in the dynamic analysis. However, one should note that proper sealing of high pressure cycles such as supercritical cycles is represent a real challenge. Basis elements of these are explained in Section 1.3.

3.2.4 Heat losses and neglect of heat accumulation

In the modelling of heat exchangers, the heat losses in the external wall of the heat exchangers are neglected. The heat exchangers are insulated and designed to limit the area of those external wall. Heat losses in the pipes and additional components is also not directly taken into account. Furthermore, the heat accumulation in pipes and additional components was not taken into account due to the lack of knowledge of the actual installation.

3.2.5 Low Mach number assumption

A factor limiting the Mach number M is the avoidance of the two phase region in the compressor. From a practical point of view and assuming that condensation takes place in equilibrium conditions, in order to avoid the appearance of the two phase region in the compressor due to the local acceleration of the flow, the absolute Mach number at the throat is limited [58]. Furthermore, the flow in the compressor shows a low relative Mach number regardless of the low sound speed near critical point (due to the low compressibility factor and isentropic exponent defined in (3.17) and (3.18) respectively and higher molar mass than air as seen in equation (3.16)) hence the Mach number in the supercritical CO_2 compressor can still be considered low [16] (especially since because of the sharp variations of the isentropic exponent and compressibility factor with pressure and temperature near the critical point, the value of the speed of sound can show rapid increase as seen in Fig. 1.4). For mGT's the low Mach number assumption is taken and is reasonable since the flow velocities outside turbomachinery components are usually kept below a Mach number of 0.3 to minimize pressure losses. While flow velocities inside the compressor and turbine are higher, the implemented model is based on turbomachinery maps, which account for all flow characteristics [31]. Results show that the Mach number distribution for supercritical CO_2 tends to have lower values than in the case of ideal air for compressors [28], further justifying the use of the low Mach number assumption which reduces complexity and calculation time. Due to this assumption, the total and the static thermodynamic quantities are interchangeable in further sections i.e. thermodynamic quantities with subscript 0 and thermodynamic quantities without this subscript are confounded.

3.3 Turbomachinery

To accurately predict the performance of the turbomachines used in the power cycle, their performance maps must be known. The performance maps show the operating range and the performance of a turbomachine at design and off-design conditions. These maps can be constructed from rig test results or from numerical simulations. They allow for the knowledge of the parameters of interest in turbomachines (mass flow, isentropic efficiency, rotational speed and pressure ratio between the inlet and the outlet of the turbomachine). They usually represent the pressure ratio in function of the mass flow rate for different iso-speed lines and/or the iso-efficiency lines.

Dimensional analysis

The performances of the turbomachine can change drastically with the inlet conditions, hence dimensional analysis is used to allow a single map. Turbomachinery performance is almost always analyzed and tested with a fixed inflow condition. In other words, the assumption is that the inflow fluid temperature and pressure is defined and unchanging over the map of machine performance. Since varying conditions often exist in practice, the performance maps are sometimes adapted. The practice of adapting is particularly important in the industry. Mass produced turbomachines need to work in a huge range of ambient conditions and cannot be customized for every environment [55]. An example of this correction is shown in Fig. 3.1.

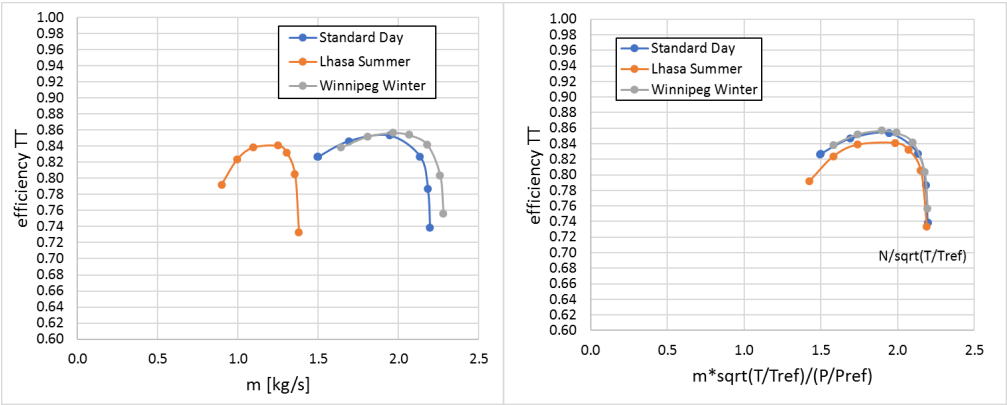

Figure 3.1: Uncorrected and corrected mass flow rate example for turbomachinery performance map [55]

Implicit in these corrections, is the assumption of perfect gas. This is a reasonable assumption for turbocharger compressors, and most air compressors in general. This assumption does not apply to our application for supercritical carbon dioxide, where the fluid properties are highly nonlinear [55]. How to manage this difficulty will be presented in Section 3.3.1.

There are several metrics used to express the mass flow rate and the rotational speed of the turbomachines to achieve a single map using dimensional analysis. One can express it with the *corrected* (or *referred*) values, the *reduced* values (called quasinondimensional, since they are derived from a truly nondimensional parameter but ignore constants, so they do have dimensions) or the *normalized* values [27]. The corrected values are a mean of standardization used to represent the operating parameters of the machine in atmospheric conditions at sea level, on a normal day (e.g. $1\,[atm]$, $288.15\,[K]$). The reduced values are derived from the actual inlet conditions only. The advantage of this definition is that it does not involve any reference value. The normalized values are often obtained from the normalization with the

design operating point, but they are rarely presented on performance maps. [40]. A summary of the different metrics can be found in Fig. 3.2 done in A. Laterre's Master Thesis:

Type	Metric	Symbol	Definition	Units
Absolute	Speed	N	–	$[rpm]$
Absolute	Mass flow	$\dot{m}$	–	$[kg \cdot s^{-1}]$
Corrected	Speed	N_{cor}	$N\sqrt{\frac{T_0}{T}}$	$[rpm]$
Corrected	Mass flow	$\dot{m}_{cor}$	$\dot{m}\frac{\sqrt{T/T_0}}{p/p_0}$	$[kg \cdot s^{-1}]$
Reduced	Speed	N_{red}	$\frac{N}{\sqrt{T}} = \frac{N_{cor}}{\sqrt{T_0}}$	$[rpm \cdot K^{-0.5}]$
Reduced	Mass flow	$\dot{m}_{red}$	$\dot{m}\frac{\sqrt{T}}{p} = \dot{m}_{cor}\frac{\sqrt{T_0}}{p_0}$	$[m \cdot s \cdot K^{0.5}]$
Normalized	Speed	N_{norm}	$\frac{N}{N_{ref}}$	$[-]$
Normalized	Mass flow	$\dot{m}_{norm}$	$\frac{\dot{m}}{\dot{m}_{ref}}$	$[-]$

Figure 3.2: Definition of the standard metrics used in performance maps. p and T stand for total inlet pressure and temperature, subscripts 0 and ref are respectively for atmospheric conditions at Sea Level on a Standard Day and reference value (i.e. design value) [40]

Scaling of the Turbec T100 Performance Maps

In this Section and the following ones, the issue of correctly predicting the performance of the turbomachines will be addressed. The model does not rely on any experimental data and the compressor and the turbine used for the cycle analyzed don't exist. The challenge will thus be to use the performance maps used in A. Laterre's Master thesis [40] (expressed with *reduced* values) and adapt them to fit supercritical CO_2 power cycles.

In his thesis, the compressor and the turbine performance maps of the Turbec T100 were modelled. Thanks to the significant number of performance data that was available and because of its simplicity, A. Laterre used a fitting method to express the global map shape. A fitting pattern was tuned to capture the shape of the map by optimizing the regression error. The results expressed with the reduced mass flow as the axis are shown in Fig. 3.3 for the compressor and Fig. 3.4 and Fig. 3.5 for the turbine. Since for the turbine map, the polynomial and the exponential fit lead to unrealistic extrapolations for certain ranges of speeds and expansion ratios, he introduced an hybridization i.e. for these range of poor prediction, the predicted points were connected with straight lines.

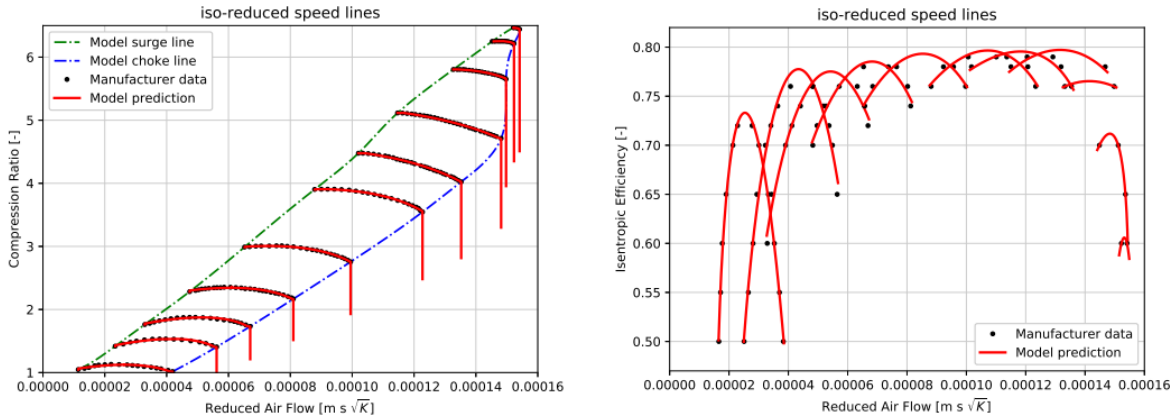

Figure 3.3: Compression ratio and isentropic efficiency T100 compressor done by [40]

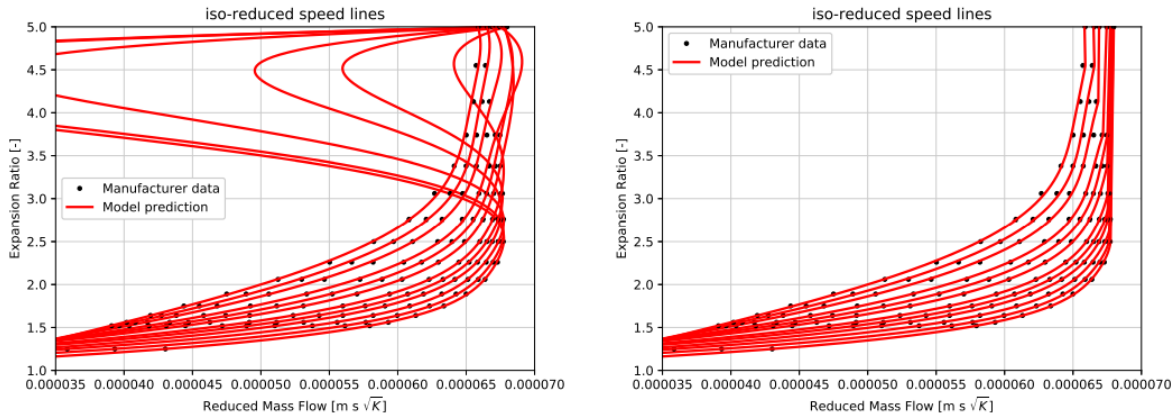

Figure 3.4: Non hybridized and hybridized expansion ratio T100 turbine done by [40]

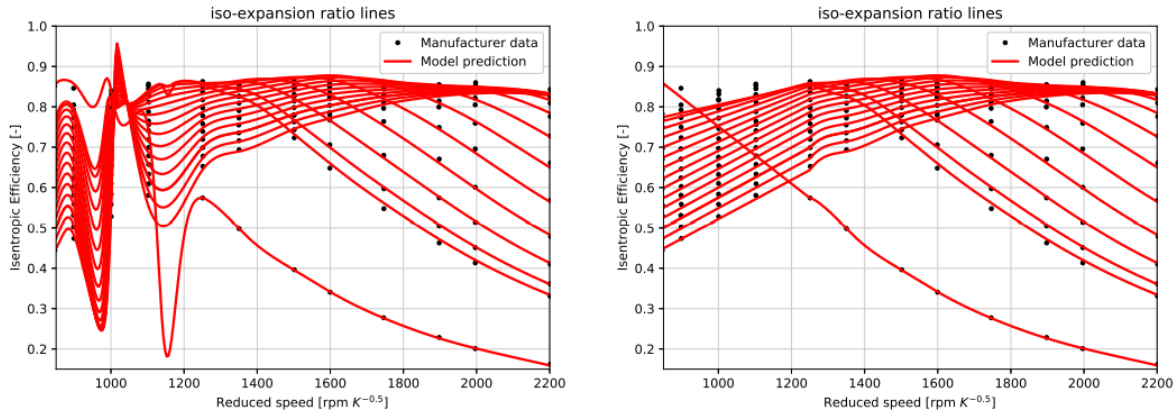

Figure 3.5: Non hybridized and hybridized isentropic efficiency T100 turbine done by [40]

Furthermore, the performance maps of the Turbec T100 give excessively high mass flow rates due to the very high pressures occurring in supercritical cycles. The bottoming compressor and turbine have been modeled by using properly scaled performance maps from topping mGT, in order to replicate the off design working conditions as done in [70]. In this way, it was possible to employ the same characteristic maps of the mGT rotating components, just scaling them with nominal $s-CO_2$ GT values. It was thus scaled as follows:

$$\dot{m}_{corr,CO_2} = \frac{\dot{m}_{air}\sqrt{T/T_{ref}}}{MW(p/p_{ref})} = \frac{\dot{m}_{corr,air}}{MW} \tag{3.6}$$

This thus means that, using the reduced values of the mass flow rate, we obtain:

$$\dot{m}_{red,CO_2} = \frac{\dot{m}_{red,air}}{MW} \tag{3.7}$$

Where MW[1] stands for the molecular weight of CO_2. Its value is $MW_{CO_2} = 44.01\,[-]$. In this way, authors were able to employ the same characteristic maps of the mGT rotating components, just scaling them with nominal $s-CO_2$ GT values.

[1]The relative molecular masses are calculated from the standard atomic weights of each element. The standard atomic weight takes into account the isotopic distribution of the element in a given sample (usually assumed to be "normal"). Relative atomic and molecular mass values as defined are dimensionless. The definition of molecular weight is most authoritatively synonymous with relative molecular mass [88].

3.3.1 Compressor

The compressor performance map shows different aspects linked to the physical operations of the compressor:

- **Pressure ratio**
  The y-axis represents the compression ratio and the x-axis represents the mass flow adapted with one of the metrics presented in Fig. 3.2. The work given to the rotating shaft allows for the compression of the fluid from inlet pressure $p_{c,in}$ to $p_{c,out}$. The compression ratio represents the ratio of the outlet pressure to the inlet pressure:

$$PR = \frac{p_{c,out}}{p_{c,in}} \tag{3.8}$$

- **Speed line**
  Different iso-speed lines are drawn on the map. They represent the shaft rotational speed. The reduced rotational speed is thus expressed as follows:

$$N_{red} = \frac{N}{\sqrt{T_{c,in}}} = \frac{60\omega}{2\pi\sqrt{T_{c,in}}} \tag{3.9}$$

- **Surge line**
  The surge line represents the line connecting the minimum mass flow rates allowed for each pressure ratio or for each speed line. Compressor surge is a form of aerodynamic instability. The term describes violent air flow oscillating in the axial direction of a compressor, which indicates the axial component of fluid velocity varies periodically and may even become negative. On a performance map, the stable operating range of a compressor is limited by the surge line. Although the line is named after a surge, technically, it is an instability boundary which denotes onsets of discernible flow instabilities [89]. Compressor surge has catastrophic consequences for the compressor. The surge margin SM is a metric used to compute the distance between the surge line (subscript s) and the operating point (subscript o). There are several definitions for this metric. The most common expressions for the surge margin are expressed either at constant rotational speed (3.10) or at constant mass flow (3.11). At constant rotational speed, the surge margin (SM) is expressed by both total pressure ratios and mass flows, whereas at constant mass flow, only the total pressure ratios are considered [68]:

$$SM = \left.\frac{\dot{m}_o}{\dot{m}_s}\frac{PR_s}{PR_o}\right|_n \tag{3.10}$$

$$SM = \left.\frac{PR_S - PR_o}{PR_s}\right|_{\dot{m}} \tag{3.11}$$

- **Choke line**
  The choke line represents the line connecting the maximum mass flow rates allowed for each pressure ratio or for each speed line. Choking of centrifugal compressor hence occurs when the compressor is operating at low discharge pressure and very high flow rates. These high flow rates at compressor choke point are actually the maximum that the compressor can push through. Any further decrease in the outlet resistance will not lead to increase in compressor output. As suggested by the compressor maps for a fixed rpm value, compressor output increases as the outlet pressure at compressor discharge drops down. This leads to increased gas velocity in the centrifugal compressor. The

increase in gas velocity can occur until it reaches its maximum at sonic velocity if there is no converging/diverging parts. When the gas velocity in any of the compressor parts reaches close to sonic velocity, this is said to be the choke point [24].

- **Isentropic enthalpy efficiency**
  Different iso-efficiency contours can also be drawn on the map showing the pressure ratio at the y-axis or the y-axis can represent the efficiency for different iso-speed lines (as done in Fig. 3.3). The expression of the compressor isentropic efficiency is expressed as follows:

$$\eta_{is,C} = \frac{h^s_{c,out} - h_{c,in}}{h_{c,out} - h_{c,in}} \tag{3.12}$$

  This compares the actual enthalpy rise that must be given to the compressor for a given pressure ratio to the ideal enthalpy rise in the case of an isentropic compression.

Map Correction Methodology

Assuming a single reference state for normalization is not valid for the compressor, which instead operates close to the critical point. In this region, the real gas properties of the fluid must be considered and the use of reduced quantities via normalization can lead to errors in the compressor performance predictions. The thermodynamic properties of supercritical real gas flows are a function of temperature and pressure contrary to ideal gas where properties only vary with temperature. Near the critical point, the properties experience sharp changes with small changes in pressure and temperature. The sharp changes in this region suggest that the performance of the machine is highly dependent on these changes which underlies the need for multiple performance map. Due to this, Marchionni et *al.* [53], implemented a model considering multiple compressor maps at four reference states that span the whole CO_2 critical region (308.15 $[K]$ at 70, 75, 80 and 85 $[bar]$). However, this could not be done in this thesis since no experimental data at different inlet conditions of the compressor is available.

To account for the real gas behavior near the critical point where the compressor operates, there is the need to find a correction of the performance maps of the Turbec T100 at the different inlet conditions. Especially since a low value of compressibility (which is the case near the critical point) is beneficial to compressors as less energy is required to compress the fluid. Pham et *al.* [66] have found out that the corrected enthalpy rise and the efficiency remain relatively constant with respect to the change of inlet conditions. This fact can be used at our advantage as further explained.

Enthalpy rise coefficient, Flow coefficient and Speed coefficient

The following methodology was based on the PhD Thesis of A-J. Martel Matos [56]. The purpose of this thesis was to make preliminary sizing and design of a centrifugal compressor for a 10 $[MW_e]$ waste heat recovery supercritical carbon dioxide Brayton power plant. But modelling and achieving proper convergence at the design point was challenging due to the proximity to the critical point. The thesis's contribution is to provide a tentative solution to the necessity of multiple compressor maps for non-ideal gas flows using dimensional analysis. By expressing the performance map in terms of the flow coefficient versus enthalpy rise coefficient for different corrected speed lines (defined by the speed coefficient), one can express the performance of the machine within a single map, referred to as the *Generalized Compressor Map*. The enthalpy rise coefficient Π_h, the flow coefficient Π_m and the speed coefficient Π_N

are defined according to equations (3.13), (3.14) and (3.15) respectively:

$$\Pi_h = \frac{\Delta h_0}{T_{0,in} R_{CO_2} Z n_s} \tag{3.13}$$

$$\Pi_m = \frac{\dot{m}_{CO_2} \sqrt{T_{0,in}}}{p_{0,in}} \sqrt{\frac{Z R_{CO_2}}{n_s}} \frac{1}{D^2} \tag{3.14}$$

$$\Pi_N = \frac{N}{\sqrt{T_{0,in}}} \frac{D}{\sqrt{Z R_{CO_2} n_s}} \tag{3.15}$$

The enthalpy rise coefficient is a dimensionless coefficient corresponding to the ratio of the difference of total enthalpy between the outlet and inlet of the compressor to the square of the speed of sound at the inlet of the compressor expressed for a real gas as:

$$a_{0,in} = \sqrt{T_{0,in} R_{CO_2} Z n_s} \tag{3.16}$$

The flow coefficient is an adimensionalization of the mass flow rate using the compressibility factor Z and the isentropic exponent n_s as well as a diameter for length scale D. The speed coefficient is an adimensionalization of the speed rotation with respect to these same parameters. R_{CO_2} is the ratio of the universal gas constant $R_u = 8.3145$ [J/mol/K] to the molar mass of CO_2; $M_{m,CO_2} = 44.0098$ [g/mol] giving a value of $R_{CO_2} = 188.924$ [J/kg/K].

The compressibility factor Z and the isentropic exponent n_s can be defined using equation (3.17) and (3.18) respectively. These terms are highly influential parameters for real gas flows.

$$Z = \frac{pv}{R_{CO_2} T} = \frac{p}{\rho R_{CO_2} T} \tag{3.17}$$

$$n_s = -\frac{v}{p} \left(\frac{\partial p}{\partial v} \right)_s = -\gamma \frac{v}{p} \left(\frac{\partial p}{\partial v} \right)_T \tag{3.18}$$

The compressibility factor Z is defined as the ratio between the actual specific volume of the fluid to the specific volume it would have if considered an ideal gas. Ideal gases are defined by values close to unity; under such conditions compressibility effects are less influential and properties vary with temperature. As Z deviates from unity, the ideal gas assumptions break down and the fluid behaves like a real gas, in which properties vary with temperature and pressure [56].

The isentropic exponent definition is based on the isentropic relations -derived from (3.19)- for a perfect gas where γ stands for the ratio of specific heat at constant pressure to the specific heat at constant volume.

$$\frac{p}{\rho^\gamma} = const. \tag{3.19}$$

But in the case of a real gas, the isentropic exponent n_s is used instead of the ratio of heat capacities. This substitution assumes a transformation with constant n_s. Thus from equation (3.20), one can derive equation (3.18):

$$\frac{p}{\rho^{n_s}} = const. \tag{3.20}$$

For a ideal gas (following $p = \rho R_{CO_2} T$), equation (3.18) reduces to $n_s = \gamma$. The variation of the compressiblity factor and the isentropic exponent for different conditions of pressure and temperature can be seen in Fig. 3.6 and Fig. 3.7.

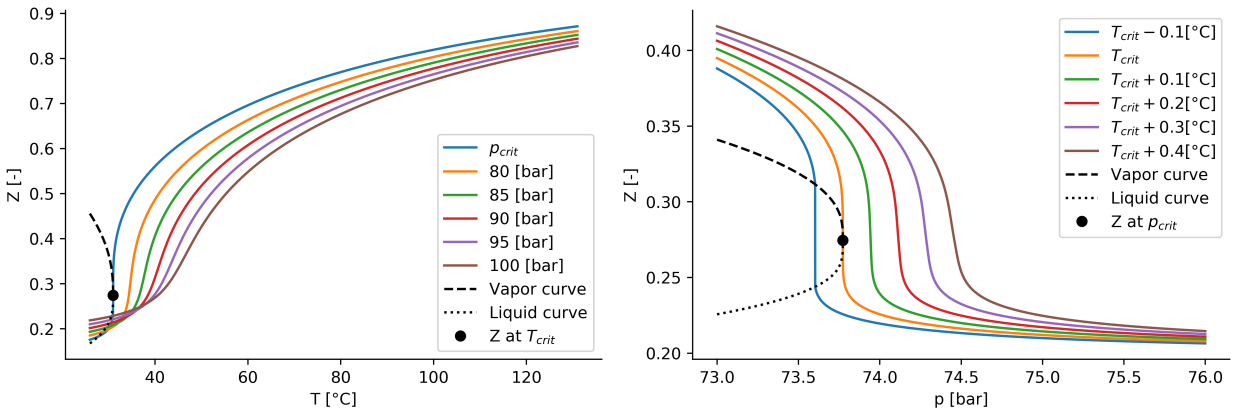

Figure 3.6: CO_2 compressiblity variations in function of (a) temperature, (b) pressure

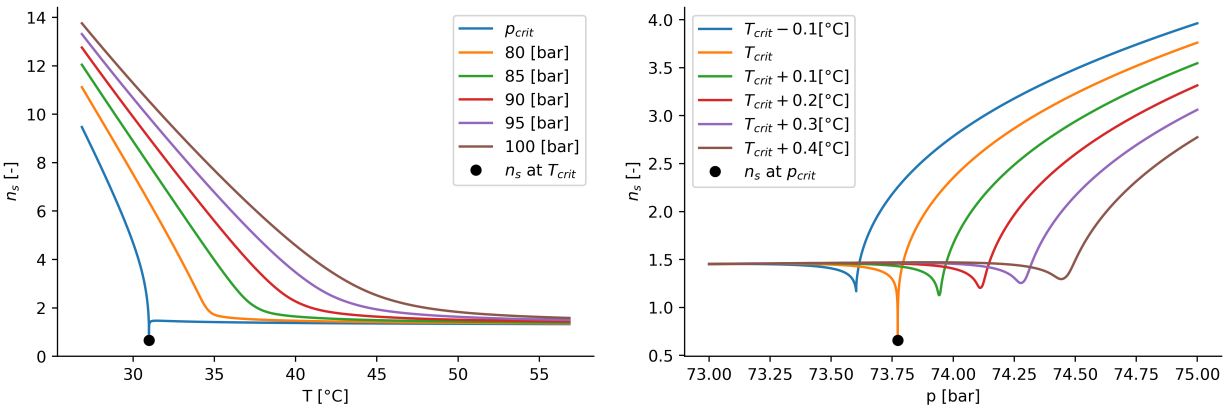

Figure 3.7: CO_2 isentropic exponent variations in function of (a) temperature, (b) pressure

These figures confirm what was said previously about the properties of the fluid experiencing very sharp changes near the critical point. From the values of the compressibility factor, one can see that supercritical CO_2 at the conditions near the critical point is far from an ideal gas hence this assumption cannot be used. The compressibility factor decreases with pressure and increases with temperature which means from equation (3.17) that density increases when Z decreases hence justifying the liquid density of the fluid near the critical point as seen in Fig. 1.3. The isentropic exponent tends to remain relatively constant even when pressure increases when temperature is sufficiently high, hence the isentropic exponent shows little variations between real and ideal gas regions for supercritical CO_2.

Generalized Compressor Performance Map

Due to the convergence problems occurring when using Computational Fluid Dynamics (CFD) using inlet conditions near the critical point, the author of the thesis [56] chose to model the centrifugal compressor at another design point which lies in the supercritical region but whose temperature and pressure are such that the perfect gas assumption can be used hence allowing proper convergence ($p = 10\,MPa$], $T = 600\,[K]$, $Z = 0.98\,[-]$ and $n_s = 1.27\,[-]$). This point is referred to as *partially dynamic* for a geometrically similar machine. The

geometry is fixed between the design point in the real gas region and in the ideal gas region and is therefore geometrically similar. To find this second operating point such that it can be called *partially dynamic*, a *Scaling Methodology* was introduced. The partial similarity was achieved by marinating the flow and speed coefficients constant. Due to a geometry constraint, the Reynolds number was not matched (the Reynolds number is mainly dependent on the rotational speed and diameter of the machine, hence since the rotational speed is fixed through the speed coefficient, while the diameter of the machine is a fixed geometry parameter, it is not possible to match it), hence why the similarity is only partial, because for two operating points to be fully dynamically and geometrically similar, all the independent variables must match. However, the effects of the Reynolds number on turbomachinery are well understood (it is known that the primary effects of the Reynolds number are reflected in the efficiency) and were accounted for by using a correction formula as shown by equation (3.21) and as presented by Sjolander [73]. It is important to understand that this correction will only affect the efficiency when there is a large difference in Reynolds number between the two operating conditions.

$$\frac{1-\eta_P}{1-\eta_M} = \left(\frac{Re_M}{Re_P}\right)^n \tag{3.21}$$

n = 0.1 for centrifugal compressor	M $\longrightarrow$ Model
n = 0.2 for axial compressors	P $\longrightarrow$ Prototype

This allowed the author to derive a performance map for this design point linking the pressure ratio to the flow coefficient as it is classically done for turbomachines.

As said previously, one can notice that the enthalpy rise coefficient remains relatively constant between the partially dynamically operating points for different inlet conditions around the critical point. Furthermore, it has been shown that despite modeling with different fluids (with different values of γ, Z and n_s (ideal versus real)) and despite different Reynolds number, the enthalpy rise coefficient remained relatively constant. In particular, at the moment, it can be shown that the enthalpy rise coefficient remains constant between air and CO_2. The enthalpy rise coefficient then becomes of great value to turbomachinery designers when it comes to expressing the characteristic map. A constant value of enthalpy rise suggests the need to create only one characteristic map. This unique map was referred in the PhD thesis to as the *Generalized Compressor Performance Map*; expressing the map with the flow coefficient Π_m versus the enthalpy rise coefficient Π_h.

The compressor performance map of the Turbec T100 (scaled according to equation (3.7)) can thus be of use. Since it was determined for air (for which the ideal gas approximation is valid), it can be used as the performance map for the second design point in the supercritical region that follow the ideal gas assumption. Hence, from that, the *Generalized Compressor Performance Map* of the Turbec T100 compressor performance map can be deduced. The next step, described below, is called the *Projection Methodology*. It allows to project the performance map at the desired inlet conditions from the *Generalized Compressor Performance Map*.

Fig. 3.9 shows the *Generalized Compressor Performance Map* derived from the Turbec T100's initial performance map scaled according to equation (3.7) showing the pressure ratio in function of the reduced mass flow rate shown in Fig. 3.8. For the *Generalized Performance Map*, the length scale diameter used to obtain the flow coefficient is worth $D = 100\,[mm]$, derived from the dimensions of the impeller of the centrifugal compressor designed in [56]. This was chosen for the purpose of representation of the maps. In practice in our analysis the

size of this diameter does not have an impact since it will cancel itself. One should note that Fig. 3.9 represents the isentropic enthalpy enthalpy rise coefficient Π_h^s defined in equation (3.22). The impact of the efficiency will be accounted for in the *Projection Methodology*.

$$\Pi_h = \frac{h_{out} - h_{in}}{a_{in}^2} = \frac{h_{out}^s - h_{in}}{a_{in}^2 \eta_{is,C}} = \frac{\Pi_h^s}{\eta_{is,C}} \tag{3.22}$$

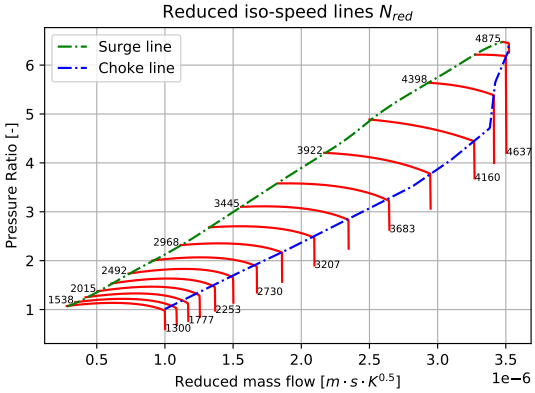

Figure 3.8: Initial T100 Compressor Map

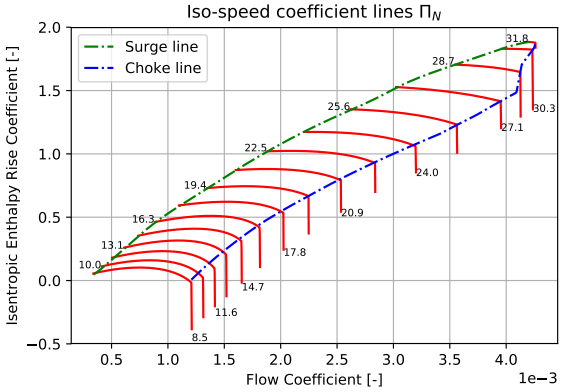

Figure 3.9: Generalized Compressor Map

Projection Methodology

As said previously, the *Projection Methodology* allows the designer to derive any map for any combination of total inlet pressure $p_1 = p_{proj,in}$ and total inlet temperature $T_1 = T_{proj,in}$ in terms of the pressure ratio from the *Generalized Compressor Performance Map*. For that, the following steps have to be followed again according to [56]:

☐ **Step 1**
Choose the total inlet conditions of the compressor which are called the *Projection Point* $(p_{proj,in}, T_{proj,in})$.

☐ **Step 2**
Using *CoolProp*, compute the following properties for the inlet state:

$$a_{proj,in} = f(p_{proj,in}, T_{proj,in}) \tag{3.23}$$

$$\rho_{proj,in} = f(p_{proj,in}, T_{proj,in}) \tag{3.24}$$

$$h_{proj,in} = f(p_{proj,in}, T_{proj,in}) \tag{3.25}$$

$$s_{proj,in} = f(p_{proj,in}, T_{proj,in}) \tag{3.26}$$

$$\mu_{proj,in} = f(p_{proj,in}, T_{proj,in}) \tag{3.27}$$

☐ **Step 3**
Choose a point in the *Generalized Compressor Performance Map*: $(\Pi_h, \Pi_m)_{GM}$ and its corresponding values for $(\Pi_N, \eta_{is,C})_{GM}$.

☐ **Step 4**
Compute the rotational speed N_{proj} and the mass flow $\dot{m}_{proj}$ of the *Projection Point*. Recall that from similarity, the Flow and speed coefficients remain constant:

$$\Pi_{N,proj} = \Pi_{N,GM} \tag{3.28}$$

$$\Pi_{m,proj} = \Pi_{m,GM} \tag{3.29}$$

Hence, N_{proj} and $\dot{m}_{proj}$ can be found using equations (3.15) and (3.14).

☐ **Step 5**

Compute the Reynolds number of the *Projection Point* (3.30) and for the inlet conditions of the *Generalized Map* (3.31).

$$Re_{proj} = \frac{\rho_{proj,i} N_{proj} D^2}{\mu_{proj,i}} \tag{3.30}$$

$$Re_{GM} = \frac{\rho_{GM} N_{GM} D^2}{\mu_{GM}} \tag{3.31}$$

☐ **Step 6**

Apply Reynolds number correction to CFD efficiency as seen in equation (3.21).

$$\eta_{proj} = 1 - (1 - \eta_{GM}) \left(\frac{Re_{GM}}{Re_{proj}} \right)^{0.1} \tag{3.32}$$

With respect to equation (3.21), n = 0.1, since the Turbec T100 compressor is a centrifugal compressor.

☐ **Step 7**

Compute the isentropic total enthalpy difference at the *Projection Point* Δh^s_{proj} from using the fact that the enthalpy rise coefficient remains constant.

$$\Pi_{h,proj} = \Pi_{h,GM} \tag{3.33}$$

$$\frac{\Pi^s_{h,proj}}{\eta_{proj}} = \frac{\Pi^s_{h,GM}}{\eta_{GM}} \tag{3.34}$$

Hence Δh^s_{proj} can be found from equation (3.13) and is expressed as follows:

$$\Delta h^s_{proj} = \Pi^s_{h,GM} \frac{\eta_{proj}}{\eta_{GM}} a^2_{proj,in} \tag{3.35}$$

The total enthalpy at the outlet of the compressor $h_{proj,out}$ is thus found:

$$h^s_{proj,out} = h_{proj,in} + \Delta h^s_{proj} \tag{3.36}$$

☐ **Step 8**

Use *CoolProp* to compute the outlet total pressure $p_{proj,o}$ hence the pressure ratio PR:

$$p_{proj,out} = f(h^s_{proj,out}, s_{proj,in}) \tag{3.37}$$

$$PR = \frac{p_{proj,out}}{p_{proj,in}} \tag{3.38}$$

☐ **Step 9**

Repeat Steps 3 to 8 until all desired operating points in the *Generalized Map* have been converted to pressure ratio versus Reduced mass flow for the new *Projection Point*.

Fig. 3.10 and Fig. 3.11 show the compressor performance maps expressed in the "usual" way i.e. in function of the pressure ratio versus the reduced mass flow rate for the different reduced speed lines. The iso-speed lines represented are deduced from the iso-speed lines in Fig. 3.9.

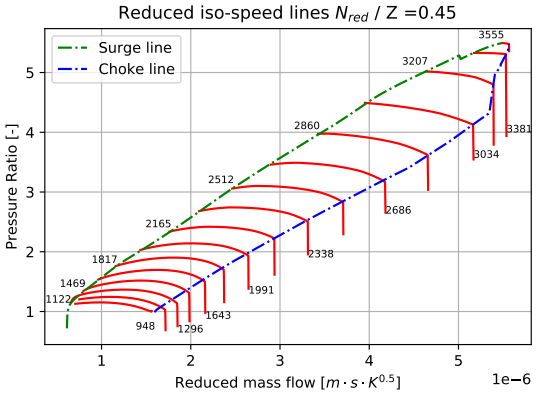

Figure 3.10: Projected Compressor Map $T_{proj,in}$ = 308.15 [K] - $p_{proj,in}$ = 76 [bar]

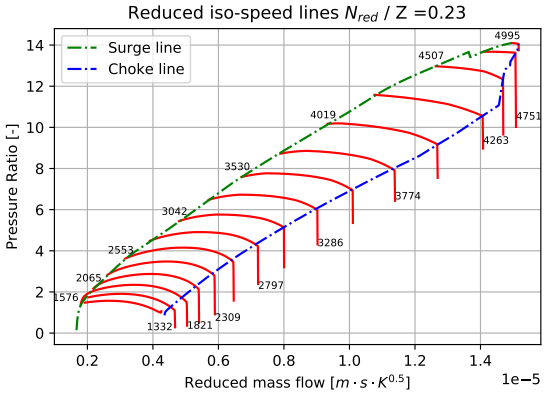

Figure 3.11: Projected Compressor Map $T_{proj,in}$ = 308.15 [K] - $p_{proj,in}$ = 90 [bar]

These maps suggest that the performance of the machine vary with inlet conditions as one would expected. These changes can be seen through the speed lines. The different speed lines achieved a different pressure ratio for each of the inlet conditions. We see from these figures that when the inlet pressure increases, the maximum pressure ratio achievable increases as well. This is due to the density of the fluid. Reduced compressibility (with pressure), induce less work needed for a given pressure rise. The maximum reduced mass flow achievable also increases with pressure increasing (so does the mass flow rate) especially due to the increase of the isentropic exponent and the decrease of compressibility. Lastly, one can observe that the reduced speed lines obtained from the same speed coefficient show higher values when the inlet pressure increases hence it is the same for the speed lines (since the inlet temperature for the three cases is the same). This is because, although the compressibility factor decreases, the isentropic exponent increases further so that in the end the value of reduced speed lines increases with the inlet pressure as seen in equation (3.15).

Fig. 3.13 shows the efficiency of the Surge line and the Choke line for different pressure inlet conditions.

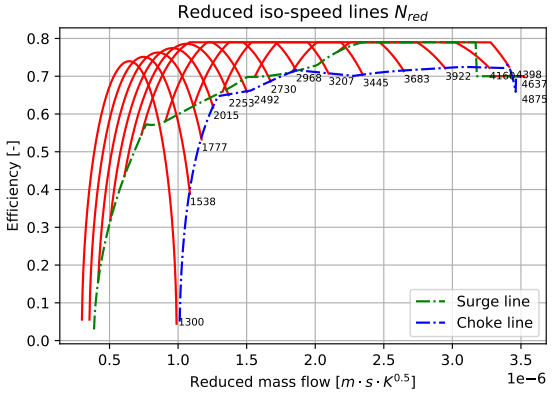

Figure 3.12: Efficiency Initial T100 Compressor Map

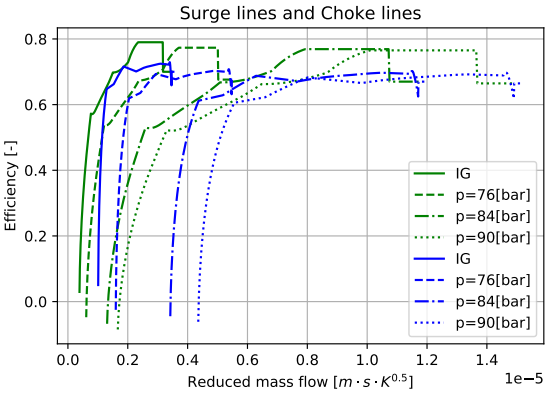

Figure 3.13: Surge line (green) and choke line (blue) projected efficiencies

These lines bound the efficiencies achievable for the minimum mass flow and the maximum

mass flow possible for each speed line as seen on Fig. 3.12 that shows the initial efficiency map when ideal gas assumption (IG) is used.

One can see that the maximum and the minimum efficiency achievable slightly reduces when the inlet pressure increases and the mass flow rate increases.

Limitations of the method

The *Projection Methodology* is valid within the region where the isentropic exponent (n_s) remains constant even if the enthalpy rise coefficient was shown to remain constant for different values of n_s. Therefore, the use of the isentropic exponent in the speed coefficient and in the flow coefficient must follow the same assumption. The accuracy of the *Projection Methodology* in the region where the isentropic exponent varies is unknown; the author of [56] suggests further investigation is recommended to fully understand the effects of the isentropic exponent changes in these regions. When projecting maps to a region near the critical point, which often happens in the case of most compressors designed for $s - CO_2$ Brayton cycles, there is a possibility that the maps will incorporate low variations between projected map and actual CFD simulations. This hypothesis could remain true as the isentropic exponent shows small changes between ideal gas region and real gas region. But the points we choose for two of the three projected maps have too low inlet temperatures for to high inlet pressures thus show large difference of isentropic exponent in comparison with the ideal gas point used in to make the *Generalized Map*; Fig. 3.7 suggests that performance maps that are projected to pressures above the critical pressure and temperatures too low for the isentropic exponent to be constant can potentially have a higher error due to the sharp changes in n_s value. This has an impact on the projected reduced mass flows and the projected reduced speed lines but not on the projected pressure ratio since as said earlier, the enthalpy rise coefficient remains constant even for different values of n_s. This is why, in [56], the maps are represented using the flow coefficient and the speed coefficient that remain the same between each maps for each *Projection Point* because of partial similarity with the *Generalized Map*. However, in the compressor block where the mass flow rate must be known, the change in isentropic exponent is accounted for because the range where the compressor is of use in the cycle analysis assumes a pressure relatively close to the critical pressure with a temperature following the *pseudo-critical line* (introduced in Section 1.2.1) such that the isentropic exponent does not exibit sharp changes. Furthermore, the change in the isentropic exponent is even more attenuated since its use is squared in the expressions of the flow coefficient (3.14) and of the speed coefficient (3.15).

Furthermore, during the compression process, the isentropic exponent and the compressibility factor experience changes between the inlet and the outlet and further investigations are required to understand the effects of this change. To be more accurate, one should use an averaged value of n_s between the inlet and outlet state of the compressor. But this would require an iterative process since the outlet state is unknown. The author of [56] and Pham et *al.* [66] both use the isentropic efficiency at the inlet of the compressor in their approach.

Finally, the investigation validated the *Generalized Compressor Map* for two different fluids down to a compressibility factor of $Z = 0.65$ [-]. Further investigation is required near the critical point to validate the *Generalized Compressor Map* for low values of Z. Just like the *Generalized Compressor Map*, the *Projection Methodology* methodology has been validated down to a compressibility factor of $Z = 0.65$ [-].

Compressor block

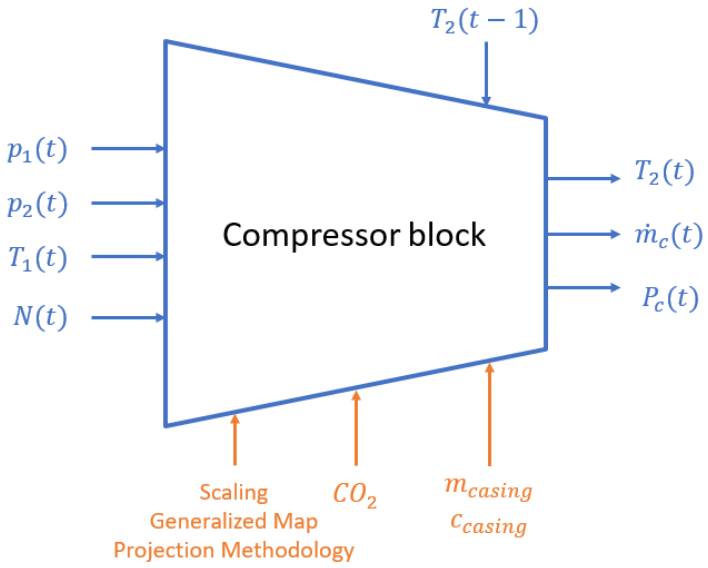

The compressor provides compressed CO_2. Using the inlet conditions of temperature and pressure, the pressure ratio as well as the shaft rotational speed, the block provides the outlet temperature, the mass flow of the compressor as well as the power required to drive the compressor. From the inlet conditions and the pressure ratio desired, the adaptation of the *Projection Methodology* provides us with the CO_2 mass flow rate as well as the efficiency.

Figure 3.14: Inputs and outputs of the compressor block

Computation of the mass flow rate and the efficiency

One must not derive the entire map for each inlet conditions encountered at the compressor but instead one point of the map is projected to derive the projection mass flow and the projection efficiency. But in this case an iterative procedure must take place. The steps to follow are as such:

- ☐ **Step 1**
  The pressure ratio and the rotational speed wanted as well as the inlet conditions constitute the projection point $(p_{proj,in}, PR_{proj}, T_{proj,in}, N_{proj})$.

- ☐ **Step 2**
  Using *CoolProp*, compute the inlet properties for the inlet state as done in the equations (3.23), (3.24), (3.25), (3.26) and (3.27).

- ☐ **Step 3**
  Use *CoolProp* and the pressure ratio PR_{proj} to find the isentropic total enthalpy rise and the projected isentropic enthalpy enthalpy rise coefficient:

$$p_{proj,out} = PR_{proj}\, p_{proj,in} \tag{3.39}$$

$$h^s_{proj,out} = f(p_{proj,out}, s_{proj,in}) \tag{3.40}$$

$$\Delta h^s_{proj} = h^s_{proj,out} - h_{proj,in} \tag{3.41}$$

$$\Pi^s_{h,proj} = \frac{\Delta h^s_{proj}}{a^2_{proj,in}} \tag{3.42}$$

- ☐ **Step 4**
  Recalling from equation (3.33) that the enthalpy rise coefficient remains constant between the *Generalized Map* and the *Projection Point*. Since the total enthalpy rise also depends

on the efficiency, which is not known, an iterative procedure must take place. As a first approximation, we assume that the efficiencies between the *Generalized Map* and the *Projection Point* match ($\eta_{GM} = \eta_{proj}$). Hence, the guess of the first coordinate of the *Generalized Map*, $\Pi^s_{h,GM,guess}$ can be found from equation (3.34):

$$\Pi^s_{h,GM,guess} = \Pi^s_{h,proj} \tag{3.43}$$

☐ **Step 5**
To find the second coordinate of the *Generalized Map*, the projection rotational speed is used N_{proj} and using partial similarity -from equation (3.28)- to find the speed coefficient $\Pi_{N,GM}$.

☐ **Step 6**
Using the *Generalized Map* represented in Fig. 3.9, the efficiency $\eta_{GM,guess}$ and the flow coefficient $\Pi_{m,GM,guess}$ of the point $(\Pi^s_{h,guess}, \Pi_N)_{GM}$ can be found.

☐ **Step 7**
Compute the Reynolds number of the *Projection Point* (Re_{proj}) (3.30) and the Reynolds number for the inlet conditions of the *Generalized Map* (Re_{GM}) (3.31) and apply the Reynolds number correction to CFD efficiency as in equation (3.32) to find $\eta_{proj,guess}$.

☐ **Step 8**
Use partial similarity again -from equation (3.29)- to find the guess for the projected mass flow $\dot{m}_{proj,guess}$.

☐ **Step 9**
Compute again the isentropic enthalpy enthalpy rise coefficient of the *Generalized Map* with the two guesses obtained for the efficiencies as in equation (3.34):

$$\Pi^s_{h,GM,new} = \Pi^s_{h,proj} \frac{\eta_{GM,guess}}{\eta_{proj,guess}} \tag{3.44}$$

☐ **Step 10**
Repeat **Step 4** up to **Step 9** until the isentropic enthalpy enthalpy rise coefficient of the i^{th} and $(i+1)^{th}$ iterations converge i.e. they are close up to an error ϵ:

$$|\Pi^s_{h,GM,i+1} - \Pi^s_{h,GM,i}| < \epsilon \tag{3.45}$$

Using these steps, the mass flow rate at the compressor $\dot{m}_c = \dot{m}_{proj}$ and the compressor isentropic efficiency $\eta_{is,C} = \eta_{proj}$ at the desired inlet conditions can be found using only one performance map.

However, using an iterative procedure can be time consuming. Hence an approximation is used; as said earlier, the correction of the efficiency shows significant impact only if the Reynolds number difference between the projected point and the design point show a large difference. Using the approximation used in the first guess which is that the efficiencies are the same, one obtains a very good approximation for the isentropic enthalpy enthalpy rise coefficient for the *Projection Point* and for the *Generalized Map*. For this parameter, the efficiency are assumed the same but the correction of the efficiency of equation (3.32) is still applied afterwards. Fig. 3.15 show the efficiency relative error e_{rel} defined in equation (3.15)

for the different reduced speed lines for the two inlet conditions (shown in Fig. 3.10 and Fig. 3.11) used in the illustration of the *Projection Methodology*.

$$e_{rel} = 100 \cdot \frac{|\eta_{GM} - \eta_{proj}|}{\eta_{GM}} \tag{3.46}$$

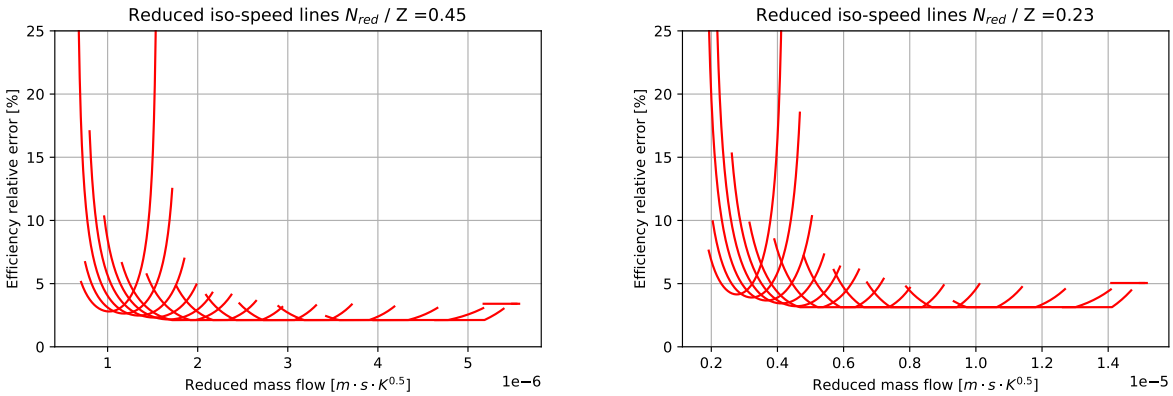

Figure 3.15: Relative difference between projected efficiency and *Generalized Map* efficiency for different projected performance maps
(a) $T_{proj,in} = 308.15\,[K]$ - $p_{proj,in} = 76\,[bar]$, (b) $T_{proj,in} = 308.15\,[K]$ - $p_{proj,in} = 90\,[bar]$

One can observe a rapid decrease of the maximal error for a given speed line when the speed lines value increase. For higher speed lines the relative error is relatively small whereas for the lower speed lines this value can show significantly high values. Furthermore, the relative error tends to slightly increase when the inlet pressure increases. Fig. 3.16 shows the relative error between the exact (subscript e) and the approximated (subscript a) *Projection Methodology* of the efficiency as defined in (3.47), as well as the relative error of the mass flow rate and the power needed for the compressor as defined in (3.48) and (3.49) respectively for typical inlet conditions obtained in the compressor.

$$e_{rel,\eta} = 100 \cdot \frac{|\eta_{proj,e} - \eta_{proj,a}|}{\eta_{proj,e}} \tag{3.47}$$

$$e_{rel,\dot{m}_c} = 100 \cdot \frac{|\dot{m}_{c,proj,e} - \dot{m}_{c,proj,a}|}{\dot{m}_{c,proj,e}} \tag{3.48}$$

$$e_{rel,P_c} = 100 \cdot \frac{|P_{c,proj,e} - P_{c,proj,a}|}{P_{c,proj,e}} \tag{3.49}$$

One can observe that the relative errors increase with the inlet temperature but tend to decrease with pressure. This error never exceeds 3.1 % for all the errors investigated. However further investigations are needed to acknowledge the impact of using the approximated method on the whole cycle. And the author of [56] suggests further investigations are needed to validate the Reynolds number correction used in the exact *Projection Methodology*. Furthermore, Pham et *al.* [66] neglected efficiency difference as they acknowledged small variation of efficiency at a given set of dimensionless mass flow rate and speed (flow coefficient and speed coefficient), this further motivates the use of the approximated *Projection Methodology* in the compressor block.

Fig. 3.17 and Fig. 3.18 show the changes brought by the *Projection Methodology*.

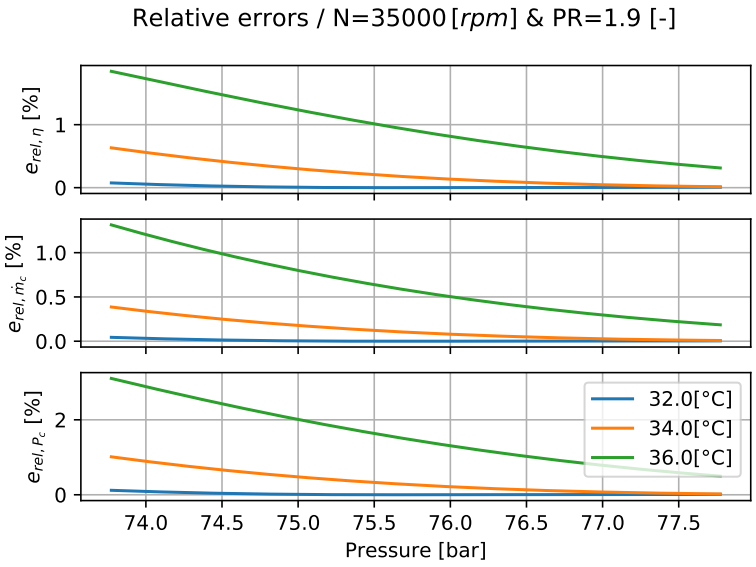

Figure 3.16: Relative errors between approximated and exact compressor block outputs

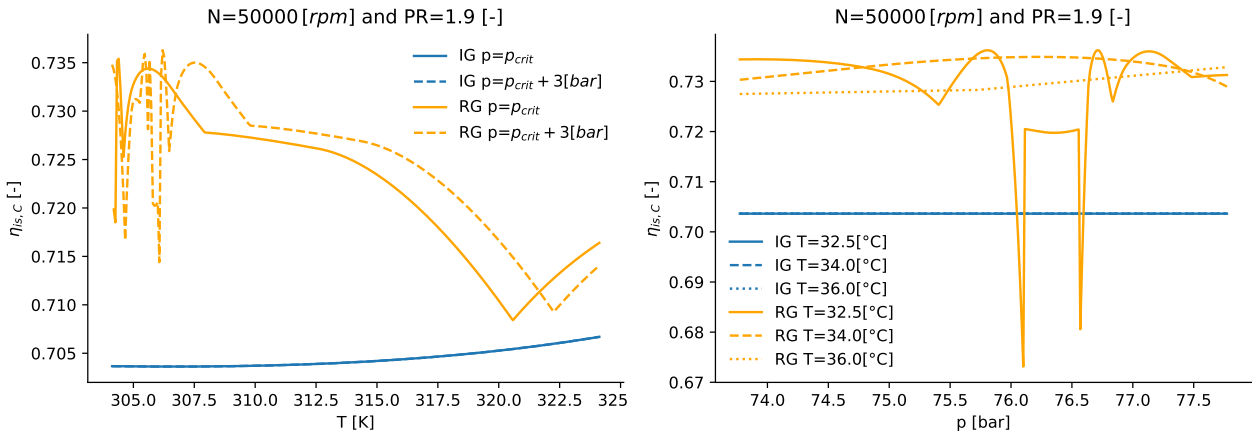

Figure 3.17: Compressor isentropic efficiency variations in function of (a) temperature, (b) pressure, ideal gas vs real gas

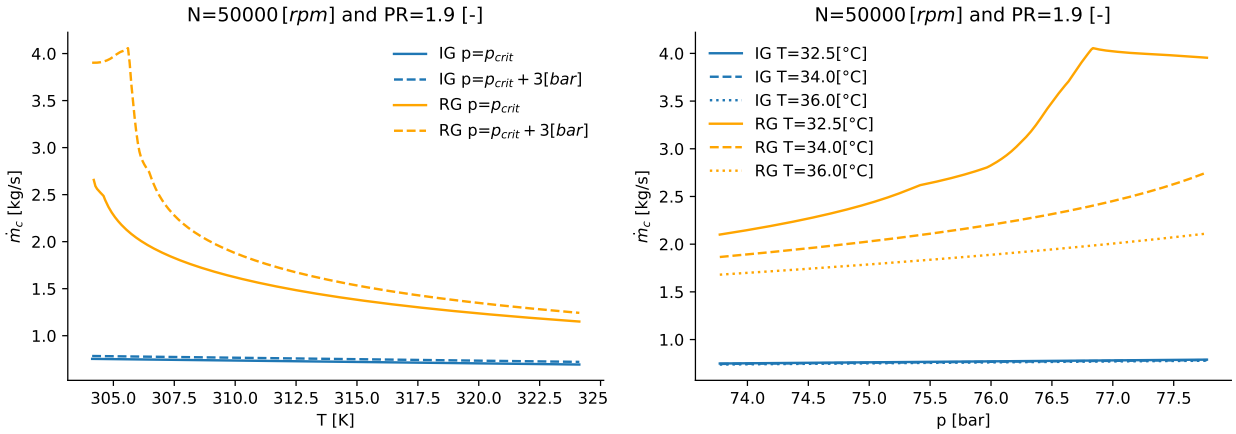

Figure 3.18: Compressor mass flow rate variations in function of (a) temperature, (b) pressure, ideal gas vs real gas

Fig. 3.17 and Fig. 3.18 show how the approximated *Projection Methodology* changes the values of efficiency and mass flow rate in comparison to the ideal gas case where the map of the Turbec T100 compressor were directly used.

The impact of the pressure is not monotonous and highly depends on the temperature in the case of efficiency. However, globally for the temperatures of interest, the isentropic efficiency tends to decrease with temperature. One can note the huge instabilities when the pressures and/or the temperatures approach the critical pressure/temperature. The mass flow rates in the case of real gas (RG) behavior are always increased compared to the compressor used with an ideal gas (IG) such as air, and they increase even more with pressure but decrease with temperature. Overall, the compressor efficiency is always increased for real gas behavior. However these values can vastly vary when changing the rotational speed and/or the pressure ratio making the impact of real gas behavior of the compressor hard to predict. Furthermore as explained earlier, the validity of the method lies in the region where the isentropic efficiency remains relatively constant. Since in equations (3.14) and (3.15), the isentropic exponent is squared, the following conditions was fixed to evaluate when the isentropic exponent of the projected point deviates too far from the isentropic exponent of the *Generalized Map*:

$$\frac{|\sqrt{n_{s,GM}} - \sqrt{n_{s,proj}}|}{\sqrt{n_{s,GM}}} < 10\ \% \tag{3.50}$$

From equation (3.50), one can see that Fig. 3.17(a) and Fig. 3.18(a) are pretty accurate because the above condition is satisfied for all the temperature investigated in the graph when $p = p_{crit}$ and for $p = p_{crit} + 3\,[bar]$, the minimum temperature before the isentropic exponent increases too much is $T_{min} = 306.74\,[K]$. Hence one can say that most of the values computed in Fig. 3.17(a) and Fig. 3.18(a) are accurate (respectively 100 % and 86.66 %). However, for Fig. 3.17(b) and Fig. 3.18(b), the accuracy sharply decreases when temperature decreases. Indeed, for $T = 36\,[°C]$, all of the values computed are deemed accurate, but for $T = 34\,[°C]$ and $T = 32\,[°C]$, only 83.0 % (i.e. when pressure rises above $p_{max} = 77.1\,[bar]$) and 44 % (i.e when pressure rises above $p_{max} = 75.54\,[bar]$) satisfy the accuracy condition. The method accuracy is thus less sensitive to pressure than temperature. This should be kept in mind for further analysis of the cycle. This means that the compressor should be working in the supercritical vapour-like region (going away from the critical temperature while staying close to critical pressure).

Temperature computation

The temperature of compressed fluid T_{comp} can be found using compressor outlet pressure $p_2 = p_{proj,out}$ and the compressed fluid enthalpy $h_{comp} = h_{proj,out}$ found with the compressed fluid isentropic enthalpy $h^s_{comp} = h^s_{proj,out}$, the compressor inlet enthalpy $h_1 = h_{proj,in}$, the compressor isentropic efficiency $\eta_{is,C} = \eta_{proj}$ as well as the entropy at the compresor inlet $s_1 = s_{proj,in}$:

$$h^s_{comp} = f(p_2, s_1) \tag{3.51}$$

$$h_{comp} = h_1 + \frac{h^s_{comp} - h_1}{\eta_{is,C}} \tag{3.52}$$

$$T_{comp} = f(p_2, h_{comp}) \tag{3.53}$$

In order to account for the heat transfer aspects to find the compressor outlet temperature T_2, one should integrate the thermal capacitance of the compressor. The thermal capacitance is

related to the energy storage capacity of the compressor casing. If the rate of flow of heat into a system is Q_1 and the rate of flow out Q_2 then the rate of change of internal energy of the system is $Q_1 - Q_2$. An increase in internal energy can result in a change in temperature [25]:

$$Q_1 - Q_2 = m \cdot c \frac{dT}{dt}, \tag{3.54}$$

where m is the mass and c is the heat capacity. The product of the two gives the thermal capacitance $C = m \cdot c$. In our case, to model the heat transfer, the thermal capacitance can be assumed to be a virtual casing capacitance. Hence the energy balance of the casing is expressed as follows as done in [40]:

$$\frac{dT_2}{dt} = \frac{\dot{m}_c(h_{comp}(p_2, T_{comp}) - h_2(p_2, T_2))}{m_{cas,C}\, c_{cas}}, \tag{3.55}$$

where $m_{cas,C}$ and c_{cas} represent the casing mass and the casing specific heat capacity making the casing thermal capacitance. The specific heat capacity of the casing and the value of the casing mass of the compressor are selected in Chapter 5. Since no experimental data is available to calibrate the casing mass, this will be estimated.

Power computation

With the mass flow rate $\dot{m}_c$ computed here above, as well as with the compressed fluid enthalpy h_{comp} and the compressor inlet enthalpy h_1, one can derive the required power consumption to drive the compressor P_c:

$$P_c = \dot{m}_c(h_{comp}(p_2, T_{comp}) - h_1(p_1, T_1)) \tag{3.56}$$

As seen, on Fig. 3.19, the power needed to drive the compressor is always higher considering real gas behavior (for the same inlet conditions) in the supercritical region. As expected, increasing the inlet pressure and/or decreasing the inlet temperature increases even more the power needed over ideal gas behavior. This is especially due to the increase of mass flow rate of the real gas despite the higher efficiency in the case of real gas behavior. However, the work needed for the compressor for the same conditions is always smaller (except for the two small peaks at 32.5 $[°C]$ due to efficiency instabilities) for the same conditions in the case of real gas behavior. In line with what was said in Section 1.2.1, when pressure increases and temperature decreases, the compressor work decreases as seen in Fig. 3.20. This shows that the trends displayed by the mass flow comparing real gas and ideal gas behavior dominate on the power.

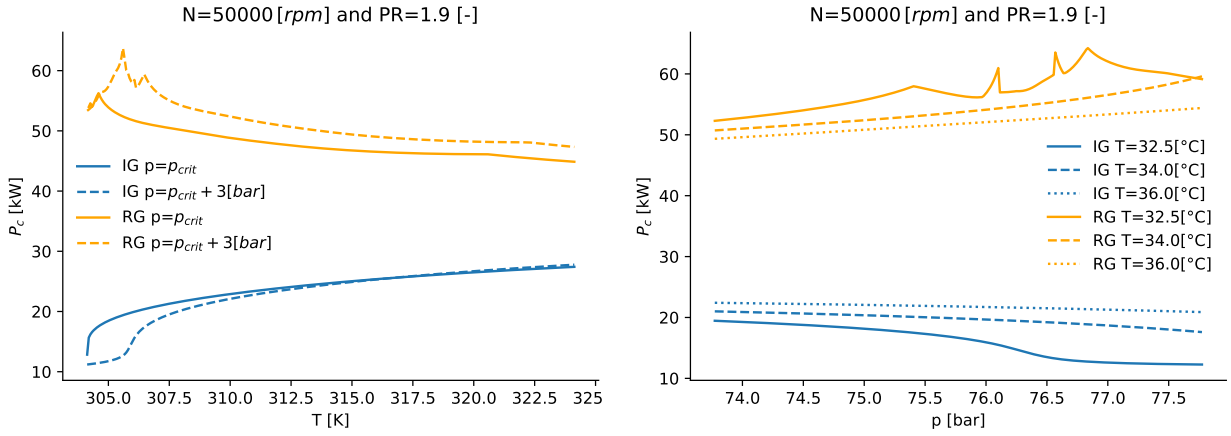

Figure 3.19: Compressor power variations in function of (a) temperature, (b) pressure, ideal gas vs real gas

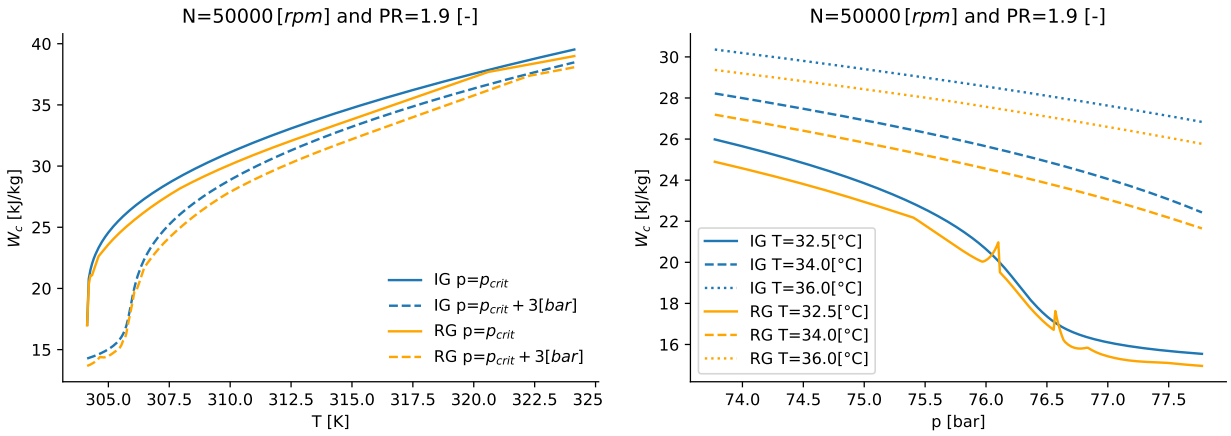

Figure 3.20: Compressor work variations in function of (a) temperature, (b) pressure, ideal gas vs real gas

One can observe that the power needed to drive the compressor show opposite trends compared to the behavior of ideal gas. This is because the values obtained in the case of the ideal gas behavior mainly follow the trends shown by the work of the compressor (shown on Fig. 3.20) because the mass flow rate variations are insignificant with changing inlet conditions as seen on Fig. 3.18 as opposed to the case considering the real gas behavior were the mass flow rates effects are dominant on the power. Hence, in conclusion, despite a better efficiency an reduced work of the compressor, the the power needed for the compressor is higher in the real gas case for the same conditions.

The same discussion about the accuracy according to equation (3.50) can take place for power and enthalpy rise as for efficiency and mass flow rate since the same ranges of temperatures and pressures were investigated.

One can also conclude from the properties of supercritical CO_2 presented in Section 1.2.1, that the compressor will mostly work in the vapour-like supercritical region meaning that the advantage that we often think of first of reduced work in the liquid-like supercritical region induces a too high mass flow rate due to increased density thus resulting in too high power consumption and unforeseeable values due to the high isentropic exponent.

Choice of rotational speed

For a given set of inlet conditions (for which the condition of equation (3.50) is satisfied), Fig. 3.21, Fig. 3.22, Fig. 3.23 and Fig. 3.24 show how the efficiency, mass flow rate, power and work of the compressor evolves with the rotational speed.

One can see that for a reduced power consumption of the compressor, the latter should work with a limited rotational speed because all the parameters analyzed exhibit a trend impacting positively power consumption when rotational speed decreases.

For the rotational speed ranges where the two lines are expressed, the real gas behavior shows better efficiency, higher mass flow rates and power consumption and smaller work confirming the discussion here above.

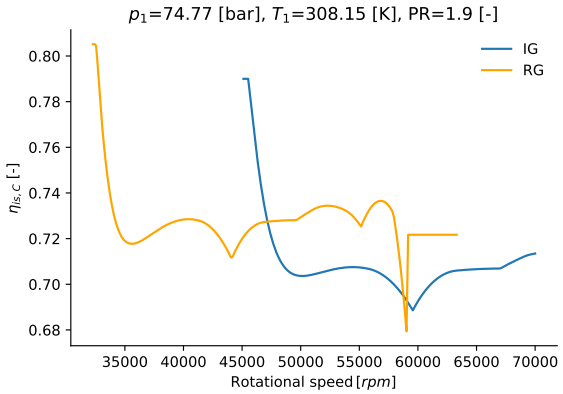

Figure 3.21: Efficiency comparison between ideal gas (IG) and real gas (RG) behavior with rotational speed

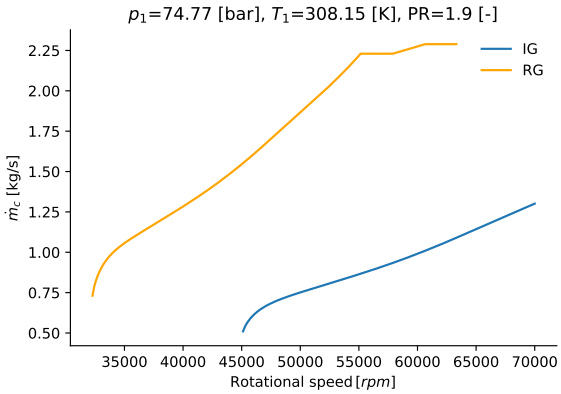

Figure 3.22: Mass flow rate comparison between ideal gas (IG) and real gas (RG) behavior with rotational speed

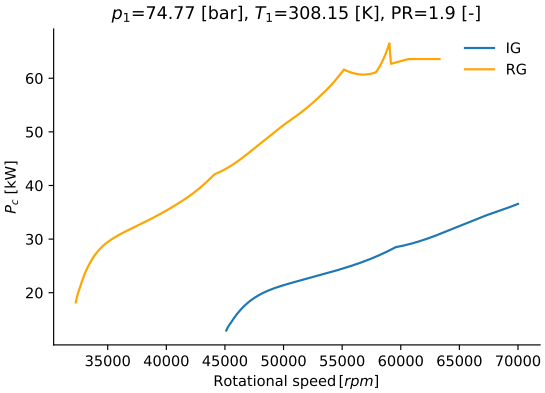

Figure 3.23: Power comparison between ideal gas (IG) and real gas (RG) behavior with rotational speed

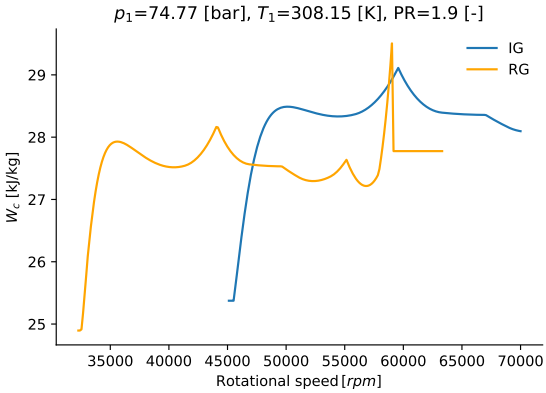

Figure 3.24: Enthalpy difference comparison between ideal gas (IG) and real gas (RG) behavior with rotational speed

One should note that when working at relatively low pressure ratio as it is the case for most supercritical cycles, the iso-speed lines do not exhibit a monotonous behavior. Especially since the initial Turbec T100 shown in Fig. 3.8 is stretched during the projection process delaying the appearance of monotonous lines for even greater pressure ratio as seen in Fig. 3.10 and Fig. 3.11. This means that for a given pressure ratio at a given speed line, two mass flow rates are possible. The mass flow rate chosen in this case is the highest. This is motivated by the fact that if the smallest mass flow rate is chosen, when the rotational speed increases such that the smallest mass flow rate is below the surge mass flow rate, the only possible mass flow rate will be the highest value hence a discontinuity in mass flow rate will appear.

The reason why the mass flow rate is not defined for all compressor rotational speeds is because, for a given pressure ratio, only a range of rotational speeds exists for all the mass flows between the surge and the choke line. The minimum of this range is higher for higher values of pressure ratio; since the projected pressure ratio is higher than the initial pressure ratio in the ideal case, this should mean than the minimum speed in the real gas behavior case should be higher. This is not what is shown (also shown in Fig. 3.10) because this effect is insignificant. The rotational speed is indeed smaller because of the compressibility is lower for a same isentropic exponent (as seen in equation (3.15) using partial similarity).

3.3.2 Turbine

The turbine performance map plays the same role as the compressor map to visualize the important physical aspects linked to its use:

- **Pressure ratio**
  The y-axis represents the expansion ratio and the x-axis represents the mass flow adapted with one of the metrics presented in Fig. 3.2 just as for the compressor. The expansion of the working fluid allows for the conversion of thermodynamic work into mechanical shaft work driving the compressor and allowing for electrical conversion of the resulting part of this work. This expansion is represented with by the ratio between the turbine outlet pressure $p_{t,out}$ to the turbine inlet pressure $p_{t,in}$:

$$ER = \frac{p_{t,in}}{p_{t,out}} \tag{3.57}$$

- **Speed line**
  Different iso-speed lines are also drawn on the map usually much closer to each other than in the case of the compressor. The reduced rotational speed is thus expressed as follows:

$$N_{red} = \frac{N}{\sqrt{T_{t,in}}} = \frac{60\omega}{2\pi\sqrt{T_{t,in}}} \tag{3.58}$$

- **Choke line**
  Such as for the compressor, not all mass flows can go through the turbine. A maximum mass flow rate represented by the choke line can pass through. As for the compressor, the choke line connects the points of maximum flow rate for the different iso-speed lines. For a given speed line at its choking point, a higher expansion ratio will no result in an increase of mass flow rate since the flow has reached sonic conditions and hence cannot increase its velocity further without change of section area. One can note that due to the closeness of the speed lines and because the typical region of use of the turbine is close to the choke line, the mass flow rate values mostly stay within a small range and close to the choke line flow rate value when changing rotational speed. The flow in the turbine is usually closer to choke than in the case of the compressor.

- **Isentropic enthalpy efficiency**
  For the turbine, an isentropic efficiency is also used and expressed as follows:

$$\eta_{is,T} = \frac{h_{t,in} - h_{t,out}}{h_{t,in} - h^s_{t,out}} \tag{3.59}$$

  The isentropic efficiency of the turbine compares the real work given by the turbine expansion to the ideal work that could have been given if the expansion happened without an increase of entropy during the process.

Performance Maps

For the turbine, due to the temperature and pressure ranges in which the turbines operates, ideal gas behavior assumption can be of use [53]. This allows for the normalization of the turbine performance map using a unique reference state hence the possibility of the direct use of the turbine performance map of the Turbec T100 using the scaling of equation (3.7). For example, using the typical range of inlet and outlet conditions, one can compute the

compressibility factor Z as seen in Fig. 3.25 and acknowledge how far these conditions vary from ideal gas assumption; recall from equation (3.17):

$$Z_{id} = 1 \Longrightarrow p = \rho R_{CO_2} T \tag{3.60}$$

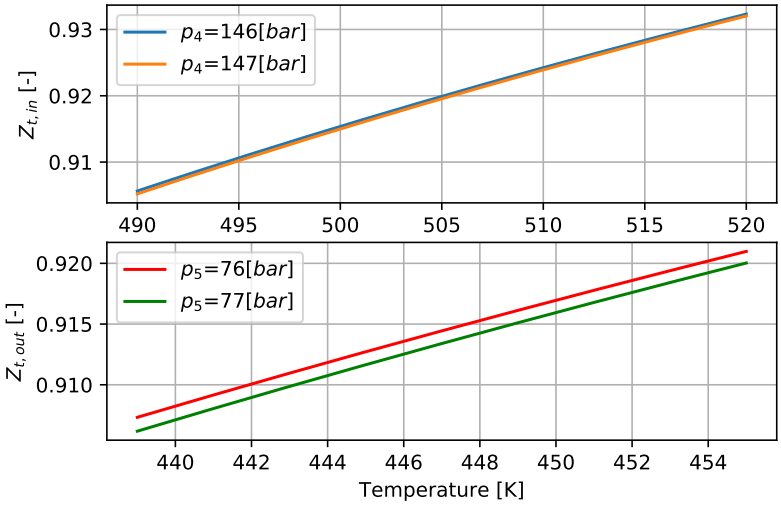

Figure 3.25: Compressibility factors for typical inlet and outlet turbine conditions

From these graphs, one can deduce that the assumption of ideal gas behavior is reasonable for both inlet and outlet conditions. Outlet conditions typically exhibit lower values of compressibility factor because despite the drop of pressure resulting in an increase of Z for given temperature (Fig. 3.17(b)), the drop of temperature at the turbine outlet, decreasing Z for given pressure (Fig. 3.17(a)), weights more on the final value of Z.

However, as one can observe in Fig. 3.26, the range of operation in $s - CO_2$ cycles does not correspond to optimized use of the Turbec T100 turbine (represented by a rectangle on Fig. 3.26).

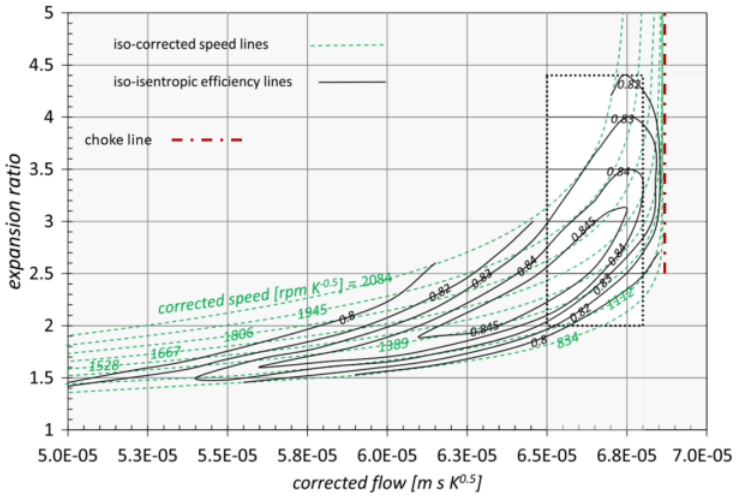

Figure 3.26: Performance maps of the Turbec T100 constructed by Caresana et *al.* [12] upon manufacturer's data. Note that the reduced flow utilized here is named under the "corrected flow" terminology. Figure found in [40].

Indeed, the pressure ratio, whose value is typically around 2 (for mechanical reasons as explained in Section 1.3), would require relatively low rotational speed to achieve high efficiency compared to higher pressure ratio and this region of use of the turbine causes higher mass flow rates changes for smaller expansion ratio changes. This turbine is not adequate for the modeling of a supercritical CO_2 cycle because its purpose is to have much higher expansion ratio. We thus assumed another strategy of modeling of the turbine block explained hereunder.

Turbine block

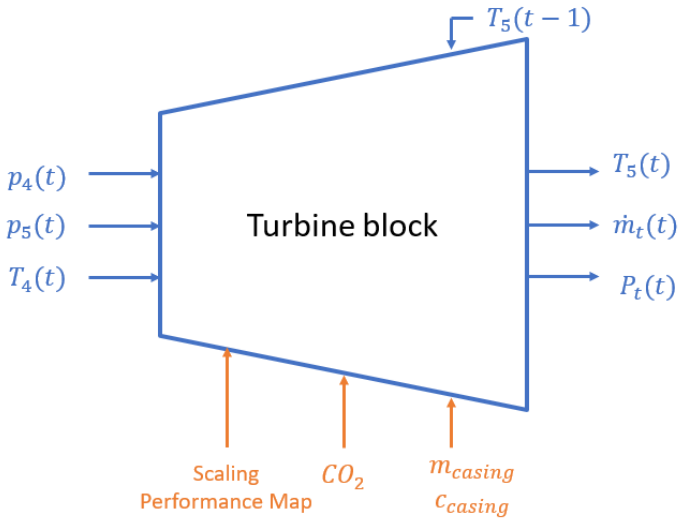

The turbine gives expanded CO_2. From the turbine inlet temperature and pressure, with the expansion ratio and the rotational speed, the block computes the outlet temperature, the mass flow rate at the turbine and the power given by the turbine to drive the compressor and provide electrical power. From the inlet conditions and the pressure ratio desired, the performance map provides us with the CO_2 mass flow rate as well as the efficiency.

Figure 3.27: Inputs and outputs of the turbine block

Computation of the mass flow rate and the efficiency

To tackle the issue of the modeling of the turbine, one can say that the turbine is choked and that the choking value is corrected for the changing turbine flow composition using following equation [13, 21]:

$$\frac{\dot{m}_t\sqrt{T_4}}{p_4} = const. \tag{3.61}$$

The first value of the mass flow rate will be taken as the one at the compressor for the first iteration. While the efficiency was assumed constant since near the choke line the efficiency does not vary significantly:

$$\eta_{is,T} = 0.84\,[-] \tag{3.62}$$

The motivations for the choice of this isentropic efficiency will be explained in Section 5.10.

Temperature computation

The temperature of the expanded flow T_{exp} is computed using turbine outlet pressure p_5 and the expanded fluid enthalpy h_{exp} computed using the expanded fluid isentropic enthalpy h^s_{exp}, the turbine inlet enthalpy h_4, the turbine isentropic efficiency $\eta_{is,T}$ as well as the entropy at the turbine inlet s_4:

$$s_4 = f(p_4, T_4) \tag{3.63}$$

$$h_4 = f(p_4, T_4) \tag{3.64}$$

$$h^s_{exp} = f(p_5, s_4) \tag{3.65}$$

$$h_{exp} = h_4 - \eta_{is,T}(h_4 - h^s_{exp}) \tag{3.66}$$

$$T_{exp} = f(p_5, h_{exp}) \tag{3.67}$$

In the same manner as for the compressor, the thermal capacitance of the casing is taken into account with a differential equation:

$$\frac{dT_5}{dt} = \frac{\dot{m}_t(h_{exp}(p_5, T_{exp}) - h_5(p_5, T_5))}{m_{cas,T}\, c_{cas}} \tag{3.68}$$

The estimation of the turbine casing mass and the specific heat value of the turbine casing are done in Chapter 5 as for the compressor.

Power computation

Knowing the mass flow and the temperature of the expanded fluid thus the expanded fluid enthalpy h_{exp} and the turbine inlet enthalpy h_4, the derivation of the power delivered by the turbine P_t follows the expression hereunder:

$$P_t = \dot{m}_t(h_4(p_4, T_4) - h_{exp}(p_5, T_{exp})) \tag{3.69}$$

Choice of rotational speed

Since the modeling of the turbine block did not require the use of a performance map, the rotational speed of the turbine is thus the same as the one of the compressor and no gear box that would induce further losses should be put between the two.

3.4 Heat exchangers

In the cycle modeled in this study, three heat exchangers have to be modeled: the recuperator, the waste heat recovery unit and the cold source. The recuperator is a CO_2/CO_2 heat exchanger whose behaviour highly influence the dynamic and efficiency of the cycle. Because 0-D model does not catch the changing characteristics of $s-CO_2$ along the heat exchanger, the recuperator will use a 1-D discretized model. The waste heat recovery unit is the flue gas/CO_2 heat exchanger, heater of the bottoming cycle. It is modeled using a 0-D model, representing the dynamic behaviour with a heat accumulator. At this exchanger, the sensitivity of the fluid characteristics to a change of temperature is smaller than the one at the recuperator, the fluid being further from critical conditions. The cold source is a water/CO_2 heat exchanger. It also uses a 0-D model, and the dynamic behaviour of the exit temperature will be modeled by considering its thermal inertia. It is used to control the lowest temperature of the cycle.

3.4.1 Recuperator

The modeling of the heat exchangers is a crucial step for the analysis of the dynamic behavior of the $s - CO_2$ cycle. Indeed, it has the slowest dynamics of the system during transient operation. Due to its high thermal load it affects the efficiency of the cycle during transient operation.

The recuperator heat exchanger is an essential component to boost the efficiency of the cycle and the power recovered from the exhaust gas. Reale et *al.* investigated the recovery of

the exhaust gas from a Turbec T100 using a simple $s-CO_2$ Brayton cycle with and without recuperator in steady state [70]. With their assumptions, the addition of a recuperator in the bottoming cycle improves its net power from 12.1 $[kW]$ to 20.6 $[kW]$. All layout of $s-CO_2$ cycle include at least one recuperator due to its crucial importance in improving the economics and performances [32, 65].

By using the hot gas at the output of the turbine to preheat the $s-CO_2$ before the waste heat recovery heat exchanger, the recuperator decreases the loss at the cold source and increase the internal efficiency of the bottoming cycle. An effective recuperator allows for a reduction of the cost and complexity associated with the design of the cooler [65]. A drawback is the reduction of the heat transfer quality at the hot source. Indeed, increasing the temperature of $s-CO_2$ at the inlet of the hot heat exchanger also increases the minimum temperature at which the flue gas from the mGT can be cooled. Overall there is a net gain in power output with the addition of an effective recuperator. A very high effectiveness, typically higher than 0.95, is not interesting as the gain in thermal efficiency is counterbalanced by the increase in pressure losses and the reduction of heat extracted from the flue gas.

A common approach in the modelling of recuperator is the use of a 1-D discretized model [48, 54]. Indeed, 0-D like the $\epsilon-NTU$ method are not able to catch the change of characteristics of the CO_2 along the heat exchanger, as those methods consider constant characteristics of the fluid. Most rigorous studies of PCHE modeling uses Computational Fluid Dynamics (CFD) to analyze the heat transfer, which is not suitable for dynamic study due to the increased computational complexity. In this 1-D model the heat exchanger can be discretized into several elements (called cells) of the same length or with the same heat duty as seen on Fig. 3.28.

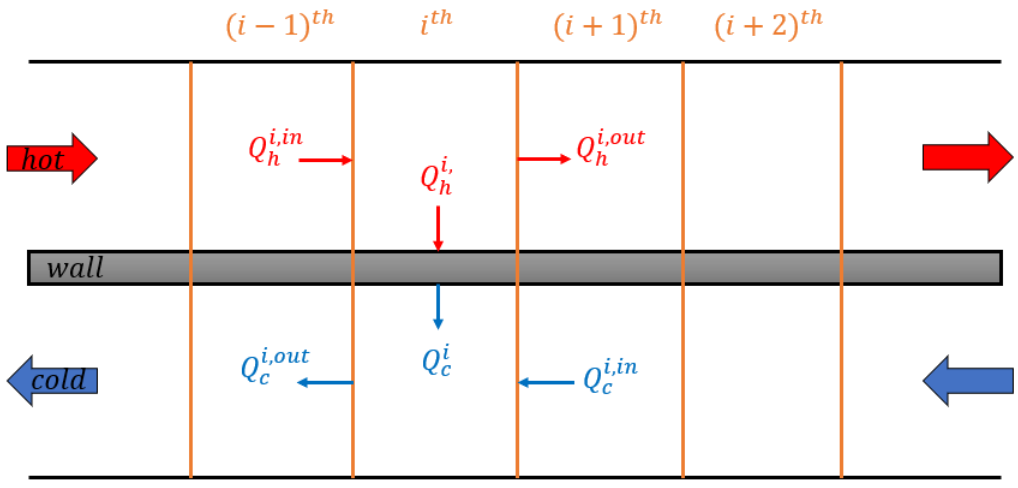

Figure 3.28: Discretization of the recuperator heat exchanger

Some assumptions must be introduced in the model:

- The PCHE considered is manufactured with an alternate stacking of hot and cold channels as a periodic repetition of the elementary unit represented on Fig. 5.3. The area of contact of the fluid with the wall is the same on both side as the number of channels is the same.
- The mass flow rate is uniformly distributed among all the channels of the heat exchanger.

- Heat losses in the external wall are neglected (see Section 3.2.4).
- Longitudinal heat conduction in the metallic core is neglected.

With those assumptions it is possible to analyze only an elementary unit of the PCHE and expand the results of the calculations to the other channels of the heat exchanger by symmetry. No special care must be accorded to the external channels due to heat losses.

The energy conservation equation for each cell at time t can be represented using the following equations:

$$Q_w^i = Q_h^i - Q_c^i, \tag{3.70}$$

with

$$Q_h^i = \dot{m}_h(h_h^{i,in} - h_h^{i,out}), \tag{3.71}$$

$$Q_c^i = \dot{m}_c(h_c^{i,out} - h_c^{i,in}), \tag{3.72}$$

where h stands for the specific enthalpy.

$$Q_w^i = m_{w,r}^i c_{w,r} \frac{dT_w^i}{dt} \tag{3.73}$$

This system of equations express the evolution of the temperature of the metallic matrix of the recuperator (also called wall, hence the subscript w, r) of the heat exchanger as a function of the heat exchanged at the hot and cold side of the heat exchanger. Here $m_{w,r}^i$ stands for the mass of metal in the wall of the recuperator heat exchanger for the i^{th} cell , and $c_{w,r}$ is the specific heat capacity of the wall material. T_w^i is the mean temperature of the metallic matrix. Q_h^i and Q_c^i are respectively the heat transfer rate in $[kW]$ at the hot and cold side of the heat exchanger for the i^{th} cell. They are explicited in term of enthalpy in equations (3.71) and (3.72).

The meaning of equation (3.70) is that all the difference between the heat flows carried in and out by the working fluid on the control volume used for conservation equation is equal to the heat flow going into the core of the heat exchanger (Q_w). The underlying assumption is that the volume of gas cannot accumulate heat. In other words the gas retention time is negligible compared to the rate of temperature change of the wall thermal mass.

The heat transfer between the cold or hot side and the wall is computed according to equation

$$Q^i = (U^i A^i)\Delta T^i\,, \tag{3.74}$$

with ΔT^i the temperature difference between the mean temperature of the wall at the i^{th} cell , written T_w^i and the mean temperature of the fluid on the i^{th} cell, respectively equation (3.75) and (3.76) for the hot and cold side.

$$\overline{T_h^i} = \frac{T_h^{i,in} + T_h^{i,out}}{2} \tag{3.75}$$

$$\overline{T_c^i} = \frac{T_c^{i,in} + T_c^{i,out}}{2} \tag{3.76}$$

Here (UA) stands for the heat transfer coefficient between the wall mean temperature and the hot/cold side, whose expression is developed in equations (3.77) and (3.78).

$$\frac{1}{(U^i A^i)_h} = \frac{1}{h_h^i A^i} + \frac{t_w/2}{k_w A^i}, \tag{3.77}$$

$$\frac{1}{(U^i A^i)_c} = \frac{1}{h_c^i A^i} + \frac{t_w/2}{k_w A^i}, \tag{3.78}$$

where h_h^i and h_c^i are respectively the convective heat transfer coefficient for the hot and cold side heat transfer between the fluid and the wall, and t_w is the thickness of the wall. k_w is the thermal conductivity of the wall material at the temperature T_w^i.

When developing equation (3.71), one can obtain [40]

$$\dot{m}_h(h_h^{i,in} - h_h^{i,out}) = (U^i A^i)_h(\overline{T_h^i} - T_w^i), \tag{3.79}$$

and since pressure is assumed constant (and the second term of equation (2.2) is assumed not to depend on temperature) within a cell, the enthalpy can be expressed only with specific heats and the above equation becomes

$$\dot{m}_h c_{p,h}^i(T_h^{i,in} - T_h^{i,out}) = (U^i A^i)_h \left(\frac{T_h^{i,in} + T_h^{i,out}}{2} - T_w^i\right), \tag{3.80}$$

with $c_{p,h}^i = c_p(p_h^i, T_h^{i,in})$ the specific heat capacity of hot side of the i^{th} cell which is considered constant for the cell and evaluated at its inlet conditions to avoid iterative procedure. The temperature at the outlet of the cell on the hot side thus becomes at time t

$$T_h^{i,out} = \frac{\dot{m}_h c_{p,h}^i T_h^{i,in} - (U^i A^i)_h \left(\frac{T_h^{i,in}}{2} - T_w^i\right)}{\frac{(U^i A^i)_h}{2} + \dot{m}_h c_{p,h}^i}, \tag{3.81}$$

As said here above, the pressure in one cell is assumed constant hence the pressure distribution (computed prior to this) considering pressure losses at the recuperator hot side is expressed as

$$p_h^i = p_5 - \frac{(p_5 - p_6)}{N_{cells} - 1}(i - 1)\,. \tag{3.82}$$

The local heat transfer coefficient is $(U^i A^i)_h = \dfrac{(UA)_h}{N_{cells}}$.

Similarly for the cold side equation (3.72) can be developed into

$$\dot{m}_c(h_c^{i,out} - h_c^{i,in}) = (U^i A^i)_c(T_w^i - \overline{T_c^i})\,, \tag{3.83}$$

$$\dot{m}_c c_{p,c}^i(T_c^{i,out} - T_c^{i,in}) = (U^i A^i)_c \left(T_w^i - \frac{T_c^{i,in} + T_c^{i,out}}{2}\right), \tag{3.84}$$

with $c_{p,c}^i = c_p(p_c^i, T_c^{i,in})$ the specific heat capacity of the cold side of the i^{th} cell which is again considered constant for the cell and evaluated at its inlet conditions to avoid iterative procedure. The temperature at the outlet of the cell on the cold side thus becomes at time t

$$T_c^{i,out} = \frac{\dot{m}_c c_{p,c}^i T_c^{i,in} + (U^i A^i)_c \left(T_w^i - \frac{T_c^{i,in}}{2}\right)}{\frac{(U^i A^i)_c}{2} + \dot{m}_c c_{p,c}^i}, \tag{3.85}$$

One should note that the expression $\dot{m}_c$ here designs the mass flow rate at the recuperator cold side and not the compressor mass flow rate as done in Section 3.3.1.

The pressure distribution considering the pressure losses is thus computed in the same

manner as for the hot side, assuming a linear pressure evolution between the cells of the exchanger.

$$p_c^i = p_2 - \frac{(p_2 - p_3)}{N_{cells} - 1}(i-1)\,. \tag{3.86}$$

The local heat transfer coefficient is $(U^i A^i)_c = \frac{(UA)_c}{N_{cells}}$. The exchanger is discretized into cells with the same heat transfer coefficient, as in Antoine Laterre's thesis [40]. It is assumed that the casing heat capacity of each cell is equal to $m_{w,r}^i c_{w,r} = \frac{m_{w,r} c_{w,r}}{N_{cells}}$.

The mean wall temperature is thus updated using equation (3.73).

$$\frac{dT_w^i}{dt} = \frac{\dot{m}_h(h_h^{i,in} - h_h^{i,out}) - \dot{m}_c(h_c^{i,out} - h_c^{i,in})}{m_{w,r}^i\, c_{w,r}} \tag{3.87}$$

How the (UA) values were estimated for the hot and cold sides is explained in Section 5.7. The casing mass and casing heat capacity of the recuperator matrix will also be justified in this Section.

Selection of the number of cells

Increasing the number of cells used to model the recuperator increases the accuracy of the model but also its computational time. The latter increases linearly with the number of cells.

To select the number of cells, an error analysis has been performed on the exit temperature predicted by the model when changing the number of cells used. The reference has been selected as the exit temperature computed with $N_{cells} = 80$. The error made during the changes of operating conditions described in Section 6.3 has been computed. The error made during transient has been defined in two ways: as the mean error made during the change of operation (equation (3.88)) and as the maximum error encountered during the transient maneuver (equation (3.89)). The error made on T_3 is shown on Fig. 3.29(a). The error made on T_5 follows the same trend.

$$error_{mean} = mean\left(\frac{T_{out,N} - T_{out,80}}{T_{out,80}}\right) \tag{3.88}$$

$$error_{max} = max\left(\frac{T_{out,N} - T_{out,80}}{T_{out,80}}\right) \tag{3.89}$$

Reducing the number of cells also has an impact on the estimated effectiveness of the heat exchanger in steady state. The steady state error made by reducing the number of cells from 80 is shown on Fig. 3.29(b). Reducing the number of cells increases the evaluated effectiveness of the recuperator and leads to an overestimated heat duty.

The number of cells chosen is 3 to limit the complexity of the model while keeping an error sufficiently low.

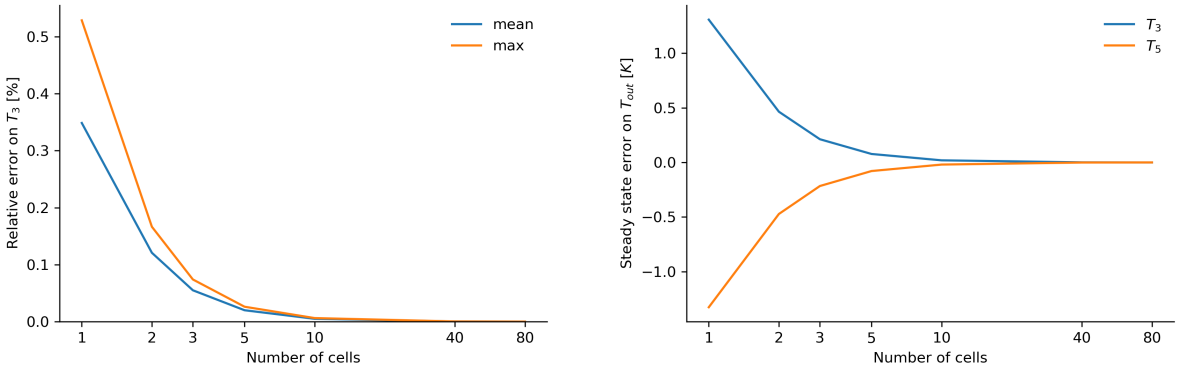

Figure 3.29: Error made by reducing the number of cells on (a) T_3 during transient and (b) T_3 and T_5 at steady state

Recuperator block

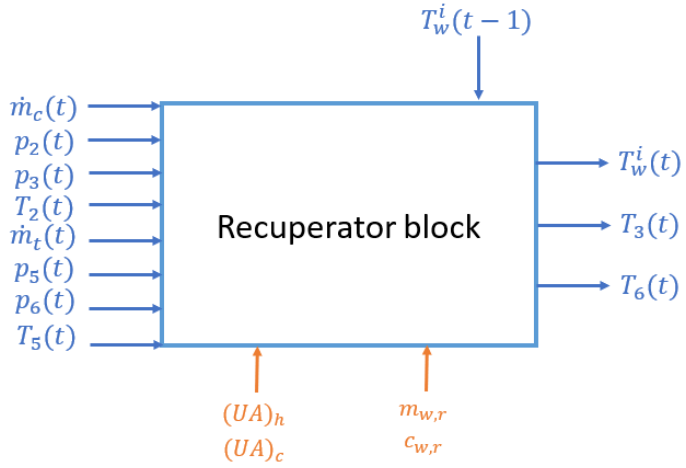

Figure 3.30: Inputs and outputs of the recuperator block

The recuperator block is thus summarized in Fig. 3.30. One should note that the mass flow rates on the cold and hot side remain constant hence no mass accumulation was considered in the recuperator. Furthermore, the outlet pressures on the cold side and hot side were computed prior to the recuperator thanks to the correlation introduced in Section 3.2.1 and the pressure distribution for each cell follows a descending step function with constant pressure for each cell.

One should also note that the mass flow at the cold side of the recuperator is the mass flow at the compressor level $\dot{m}_c$ and the mass flow at the hot side of the recuperator is the mass flow at the turbine level $\dot{m}_t$.

3.4.2 Waste heat recovery unit

The waste heat recovery unit is the heater of the cycle. It determines the heat recovered from the flue gas of the micro gas turbine. During this process, the temperature and pressures of $s-CO_2$ are far from the critical point (about $420-520$ $[K]$ and 146 $[bar]$). The sensitivity of the Nusselt number to temperature is then rather low. Indeed, varying the temperature of the CO_2 inside the same PCHE heat exchanger between 436 and 550 $[K]$, temperatures at the hot heat exchanger at nominal conditions (recovering the heat from the 100 $[kW]$ flue gas of the mGT), the maximum variation of the convective heat transfer coefficient is of 2.8 %, compared to a variation of 37 % in the case of the recuperator cold side. Moreover, only the CO_2 side of the heat exchanger is of interest for the dynamic modeling of the cycle.

For the modeling of the hot heat source, the effectiveness is considered constant at $\epsilon = 0.9$. To represent the dynamic behaviour, a lumped model is used. The transient response is then modeled by using a heat accumulator to represent the thermal inertia of the tubes and casing. The lumped assumption is valid for when the Biot number, defined as the ratio between the convective heat transfer at the surface of the body and the conduction inside the body, is close to zero. For the heater considered, we can compute using a PCHE with a geometry similar as the one described in Section 5.7:

$$Bi = \frac{hL}{k} = 0.0039 << 1, \tag{3.90}$$

with h the convective heat transfer coefficient, k the thermal conductivity of the fluid and $L = \frac{V}{A}$ the characteristic length.

Using the assumed effectiveness, defined as the ratio between the actual and the maximum heat transfer rate as in equation (2.23) defined in Section 2.4. The maximum heat exchanged in thus equal to

$$Q_{max} = min[\dot{m}_{exh}(h_{exh}(T_{exh,in}) - h_{exh}(T_{CO_2,in})), \dot{m}_{CO_2}(h_{CO_2}(T_{exh,in}) - h_{CO_2}(T_{CO_2,in}))]\,, \tag{3.91}$$

with $\dot{m}_{exh}$ the mass flow rate of flue gas in the heat exchanger, $\dot{m}_{CO_2}$ the mass flow of CO_2, h_{exh} the specific enthalpy of the flue gas as a function of temperature at atmospheric pressure and h_{CO_2} the specific enthalpy of CO_2 at the pressure at the entry of the heat exchanger as a function of temperature. In practice for this application the flue gas will have a smaller heat capacity rate ($\dot{m}c_p$) than the $s - CO_2$. At design conditions, recuperating the flue gas of a Turbec T100 working at a load of 100 $[kW]$, $(\dot{m}c_p)_{exh} = 767$ $[W/K]$ for the flue gas and $(\dot{m}c_p)_{CO_2} = 980$ $[W/K]$ for the CO_2 side, using the mean specific enthalpy between $T_{exh} = 563$ $[K]$ and $T_{CO_2,in} = 420$ $[K]$. The actual heat transfer between the flue gas and the CO_2 can then be computed as

$$Q_{hot} = \epsilon\, Q_{max}\,, \tag{3.92}$$

and Q_{hot} is expressed as

$$Q_{hot} = \dot{m}_{CO_2}(h_{CO_2}(T_{CO_2,hot}) - h_{CO_2}(T_{CO2,in}))\,, \tag{3.93}$$

evaluated at the pressure of the hot source outlet and inlet respectively, taking into account pressure losses calculated prior to the waste heat recovery block. This allows to find $T_{CO_2,hot}$ since

$$T_{CO_2,hot} = f(h_{CO2,hot}, p_{CO_2,out})\,. \tag{3.94}$$

The actual temperature of the hot end of CO_2, $T_{CO_2,out}$ is computed taking into account the thermal inertia of the casing of the heat exchanger. Using this casing approach one can obtain:

$$\frac{dT_{CO_2,out}}{dt} = \frac{\dot{m}_{CO_2}(h_{CO_2}(p_{CO_2,out}, T_{CO_2,hot}) - h_{CO_2}(p_{CO_2,out}, T_{CO_2,out}))}{m_{w,h}\, c_{w,h}} \tag{3.95}$$

This approach allows a reduction of the complexity and computational cost compared one using a discretized model. It requires a tuning of the casing coefficients $m_{w,h}$, the mass of steel in the heat exchanger and $c_{w,h}$, the heat capacity of the material. The tuning of this parameters is made in Section 5.8.

Waste heat recovery unit block

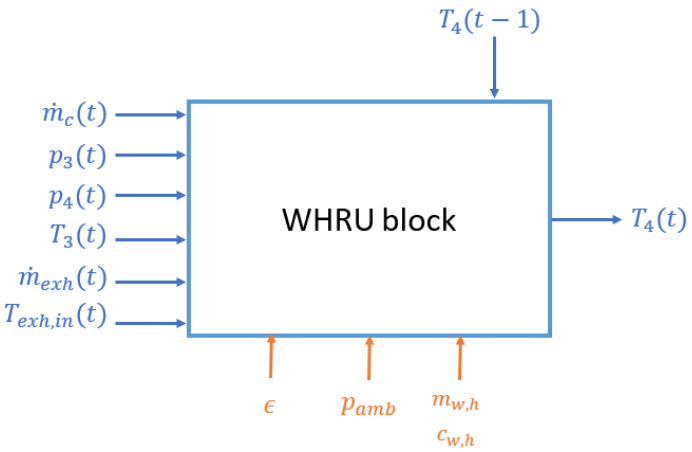

The WHRU block is thus summarized in Fig. 3.31. One should note that the CO_2 mass flow rate is constant hence no mass accumulation was considered in the WHRU. Furthermore, the outlet pressure of CO_2, p_4 was also computed prior to the WHRU block as for the recuperator thanks to the correlation introduced in Section 3.2.1 but tuned differently than for the recuperator hot and cold side as seen on Section 5.2.

Figure 3.31: Inputs and outputs of the WHRU block

The mass flow rate of CO_2 in the WHRU is still equal to the mass flow rate at the compressor level $\dot{m}_c$.

3.4.3 Cold source

The goal of the cold source is to reduce the temperature of the $s-CO_2$ at the entry of the compressor T_1. As explained in Section 1.3 and Section 1.4.2, this parameter is of high importance to reduce the work of the compressor and assure a stable operation. This is why this temperature will be controlled by varying the mass flow rate of water in this heat exchanger.

The cold sink is a water/$s-CO_2$ heat exchanger. It has been modeled using a constant (UA) value. The model used is a 0-D steady model based on equation (3.96).

$$Q_{cold} = UA\Delta T_m \tag{3.96}$$

where ΔT_m is the logarithmic mean temperature difference between CO_2 and water in the exchanger:

$$\Delta T_m = \frac{(T_{CO_2,1} - T_{water,1}) - (T_{CO_2,2} - T_{water,2})}{\log\left(\frac{T_{CO_2,1} - T_{water,1}}{T_{CO_2,2} - T_{water,2}}\right)}, \tag{3.97}$$

with $T_{CO_2,1} - T_{water,1} = \Delta T_1$ and $T_{CO_2,2} - T_{water,2} = \Delta T_2$ on Figure 3.32.

The cold heat source heat flux can be written as

$$Q_{cold} = \dot{m}_{CO_2}(h_{CO_2}(p_6, T_6) - h_{CO_2}(p_1, T_{cold})) \tag{3.98}$$

$$= \dot{m}_{H_2O}(h_{H_2O}(p_{H_2O}, T_{H_2O,out}) - h_{H_2O}(p_{H_2O}, T_{H_2O,in})), \tag{3.99}$$

with $p_{H_2O} = 3\ [bar]$.

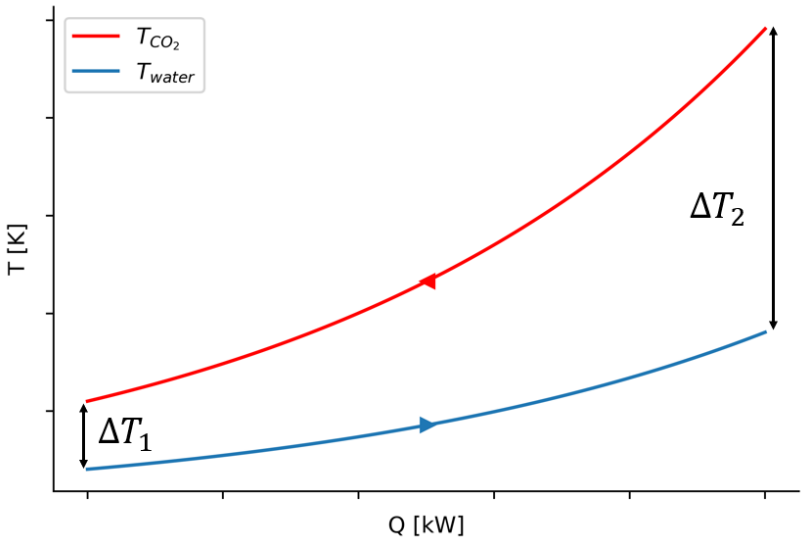

Figure 3.32: Example of temperature profile of the cooler as a function of the heat duty

The dynamic behaviour of T_1 is then simulated using a heat accumulator with the casing approach. The casing mass $m_{w,c}$ and heat capacity $c_{w,c}$ are estimated in Section 5.9.

$$\frac{dT_1}{dt} = \frac{\dot{m}_{CO_2}(h_{CO_2}(p_1, T_{cold}) - h_{CO_2}(p_1, T_1))}{m_{w,c}\, c_{w,c}}, \tag{3.100}$$

with $h_{CO_2}(p_1, T_{cold})$ the theoretical enthalpy of the CO_2 at the exit of the exchanger computed using the heat duty at time t with equation (3.98)

$$h_{CO_2}(p_1, T_{cold}) = h_{CO_2}(p_6, T_6) - \frac{Q_{cold}}{\dot{m}_{CO_2}}. \tag{3.101}$$

To compute the heat duty one needs the knowledge exit temperatures of the heat exchanger, that depends on the actual heat duty. There is then an iterative procedure. The first step assumes that the heat transfer will be the same one as the one of the previous time step to obtain the exit temperatures of the fluid with equations (3.98) and (3.99). Then the heat transfer is computed using equation (3.96). If the error between the computed and the assumed heat transfer is too large (relative error $> 0.1\,\%$ is considered), the computed heat transfer should be used to compute the temperatures in the next iteration.

To increase the convergence and avoid numerical oscillations, the next guess of Q_{cold} is calculated as the mean value between the heat transfer computed and the one of the previous iteration.

$$Q_{cold} = \frac{UA\,\Delta T_m(Q_{i-1}) + Q_{i-1}}{2} \tag{3.102}$$

The presence of a receiver tank in a heat transfer perspective is modelled by including it into the casing mass, as it increases the thermal inertia. For the control system, it means that the measurement of the temperature is made at the entry of the compressor, after the inventory tank.

Cold source block

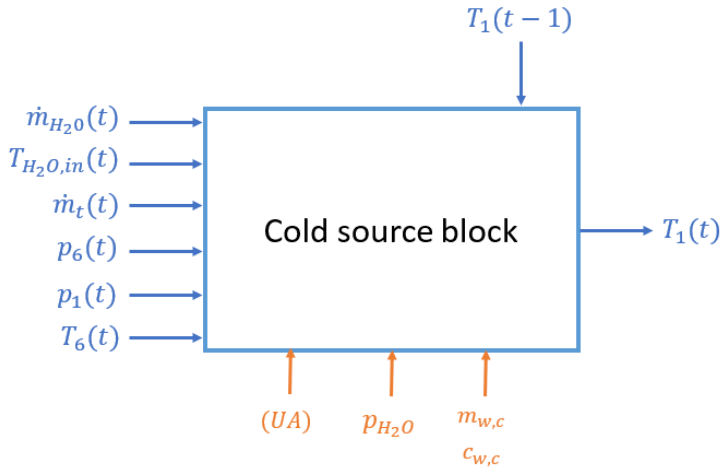

The representation of the cold source block is shown on Fig. 3.33. Once again, the mass flow rates at the cold and hot side of the heat exchanger remain constant hence no mass accumulation was taken into account. As said here above, the casing of the inventory tank coming after the cold source and before the compressor is comprised in the casing of the cold source.

Figure 3.33: Inputs and outputs of the cold source block

The mass flow rate of CO_2 at the hot source of the cold source heat exchanger is the mass flow at the turbine level $\dot{m}_t$.

3.5 Shaft

The modeling of the shaft has its interest, despite not being involved directly in the thermodynamic cycle, because of its role in transferring the power generated by the turbine to the compressor and to the generator for it to transform this mechanical energy into electrical energy.

Shaft block

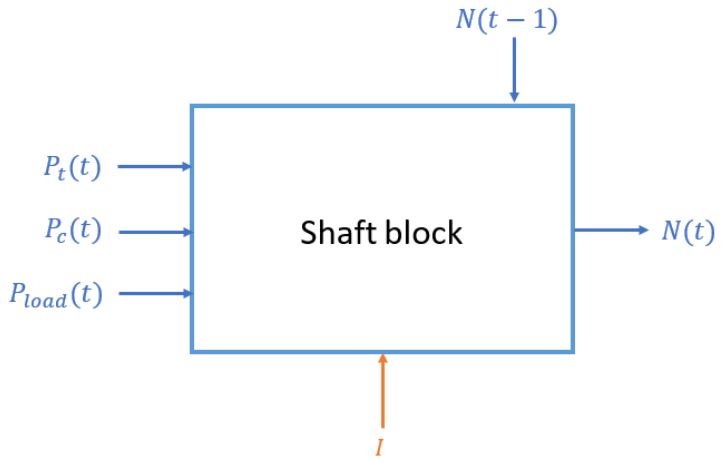

The dynamic behavior of the shaft is influenced by the difference between the power generated by the cycle (power of the turbine) $P_{in} = P_t$ and P_{out} which is the power used by the compressor P_c and the generator P_{gen} as well as the different losses P_{losses} (air friction losses, bearing losses, etc). This parameters influence rotational speed as shown in equation (3.103).

Figure 3.34: Inputs and outputs of the shaft block

$$\frac{d\omega}{dt} = \frac{P_{in} - P_{out}}{I\omega} = \frac{P_t - (P_c + P_{gen} + P_{losses})}{I\omega} \tag{3.103}$$

Recall that the rotational speed is $N = 60\omega/2\pi$, the units of N being $[rpm]$ and $\omega\,[rad/s]$.

In the modeling of the mGT done in [40], the power losses are grouped into a bearing losses P_{lb}. Due to the lack of knowledge of the modeled installation, these losses were neglected and left for a more advanced model.

Furthermore in a first approach, the power of the generator was split into electric power produced by the power block P_{elec} and electrical losses P_{le} (power lost inside the compressor and the power electronics). These electronic losses included losses of the auxiliaries in this first strategy of the control of the mGT. In this case, $P_{gen} = P_{elec} + P_{le}$ and the load power P_{load} was equal to the electric power P_{elec} such that the latter matches the demand power.

In the second approach, the auxiliaries were not included hence $P_{gen} = P_{elec} + P_{aux} + P_{le}$. Thus, in this case, the power load is computed as the sum of the electric power P_{elec} and the power of the auxiliaries (including the oil pump, the cooling water pump of the generator, the control system, etc) P_{aux}.

Once again, due to the lack of knowledge of the power block installation and its auxiliaries, the choice was made to neglect the electrical and auxiliary losses. Hence, in this case the load power is equal to the generator power. With these considerations taken into account, equation (3.103) becomes:

$$\frac{d\omega}{dt} = \frac{P_t - (P_c + P_{load})}{I\omega} \tag{3.104}$$

The discussion about the shaft's inertia I (whose value is particularly small due to compact $s - CO_2$ systems) is discussed in Section 5.3.

3.6 Inventory tanks

A physical inventory thank is put after the cold source heat exchanger and before the compressor $(IT)_c$ in order to take into account for mass accumulation. A second virtual inventory tank is put before the turbine $(IT)_t$ to account for the mass accumulation not taken into account in the recuperator, waste heat recovery unit, the pipes between the compressor and the turbine and the compressor (even if the volume of the latter is small enough to neglect this effect). The position of the inventory tank before the turbine implies an approximation since the density and mass flow variations would have impacts on the incoming blocks. This holds for the physical thank who can also be considered partially virtual since it accounts for mass accumulation inside the cold source and the turbine (the latter could also be neglected). This approximation was taken in order to consider only two mass flow rates in the system; the one at the compressor level and at the turbine level.

The mass conservation for the control volume V_i is expressed as

$$\frac{d\rho}{dt} = \frac{1}{V_i}(\dot{m}_{in} - \dot{m}_{out})\,. \tag{3.105}$$

Inventory tank prior to the compressor block

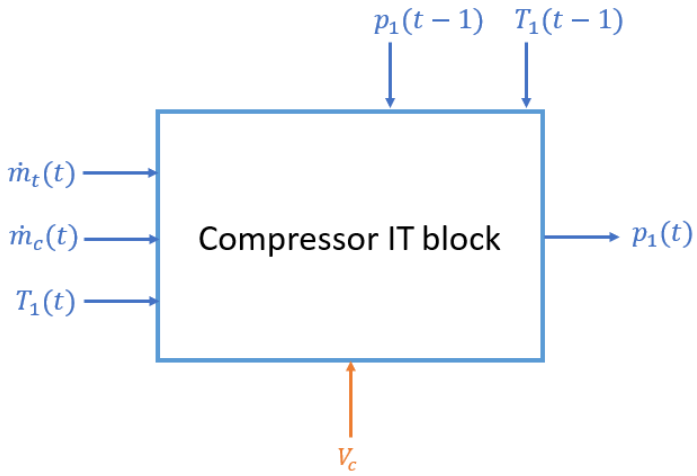

In the case of this plenum, the mass flow rate entering is the one coming from the turbine $\dot{m}_{in} = \dot{m}_t$ and the mass flow at the exit of the plenum is the one coming into the compressor $\dot{m}_{out} = \dot{m}_c$. How the inventory tank volume V_c was estimated will be addressed in Section 5.4.

Figure 3.35: Inputs and outputs of the $(IT)_c$ block

The density before the compressor at time $(t-1)$ is computed thanks to pressure and temperature at this time step

$$\rho_1(t-1) = f(p_1(t-1), T_1(t-1))\,. \tag{3.106}$$

Hence with the equation of mass conservation (3.105), one can compute the density before the compressor at the actual time step $\rho_1(t)$. The pressure at time t, $p_1(t)$, can thus be computed since

$$p_1(t) = f(\rho_1(t), T_1(t))\,. \tag{3.107}$$

Inventory tank prior to the turbine block

At the contrary, in the case of this plenum, the mass flow rate entering is the one coming from the compressor $\dot{m}_{in} = \dot{m}_c$ and the mass flow at the exit of the plenum is the one coming into the turbine $\dot{m}_{out} = \dot{m}_t$. Again, how the volume V_t was estimated will be addressed in Section 5.4.

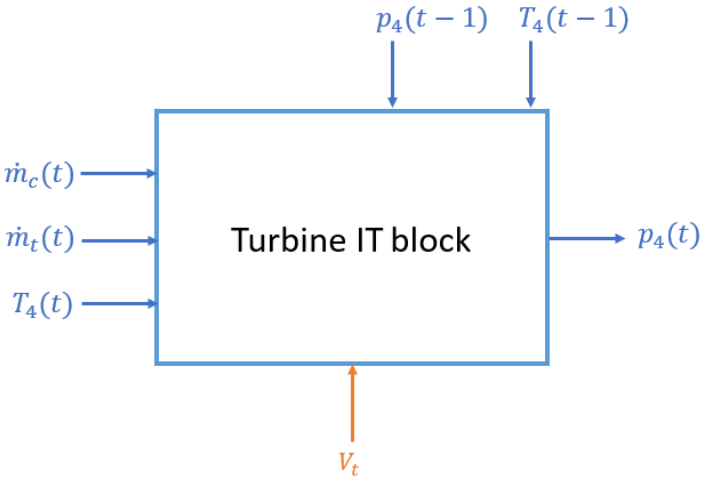

Figure 3.36: Inputs and outputs of the $(IT)_t$ block

The density before the turbine at time $(t-1)$ is computed thanks to pressure and temperature at this time step

$$\rho_4(t-1) = f(p_4(t-1), T_4(t-1))\,. \tag{3.108}$$

Again, the computation of the density before the turbine at the actual time step $\rho_4(t)$ is made thanks to equation (3.105). The pressure at time t, $p_4(t)$, can thus be computed since

$$p_4(t) = f(\rho_4(t), T_4(t)) \,. \tag{3.109}$$

3.7 Controller

The control of the cycle is based on three parameters to control; the compressor inlet pressure, the compressor inlet temperature and the shaft rotational speed. As said in Section 1.4.2, the inlet conditions are crucial parameters to control for the safe operation and good efficiency of the compressor due to the sharp variations of properties of $s - CO_2$ near the critical point. To control the compressor inlet pressure, a plenum is used and for the control of the compressor inlet temperature, the mass flow rate of the cooling water varies.

Furthermore, the control of the rotational speed is desired to allow for the isentropic efficiency of the turbine to stay relatively high [53]. Even if, in this case, the turbine maps were not used and the isentropic efficiency was assumed constant, in reality, it could vary with the rotational speed hence the choice of control. Other choices of variables to maintain constant could be used such as for example the turbine inlet temperature (for this the compressor inlet pressure would be controlled) to maintain sufficient cycle efficiency.

One should also note that the controller type used in all of the controllers used in the cycle is a Proportional Integral (PI) controller except for rotational speed control where a Proportional Integral Derivative (PID) controller is used. Indeed, as said in Section 1.4.2, a PI controller achieves a non steady state error, its sensitivity to high frequency disturbances is relatively low and it is easier to implement than other controllers available.

Pressure control

The compressor inlet pressure is maintained at a desired value by regulating the mass accumulation of the inventory tank placed before the compressor. Indeed, a fluid not too far from liquid-like supercritical CO_2 (necessitating a sufficiently high compressor inlet pressure) must be attained to achieve reduced work a the compressor. To increase this pressure, one must increase its density for a given temperature hence increase the mass accumulation $\Delta\dot{m}_{CO_2}$ (the difference between the inventory tank inlet and outlet mass flow) as seen in equation (3.105).

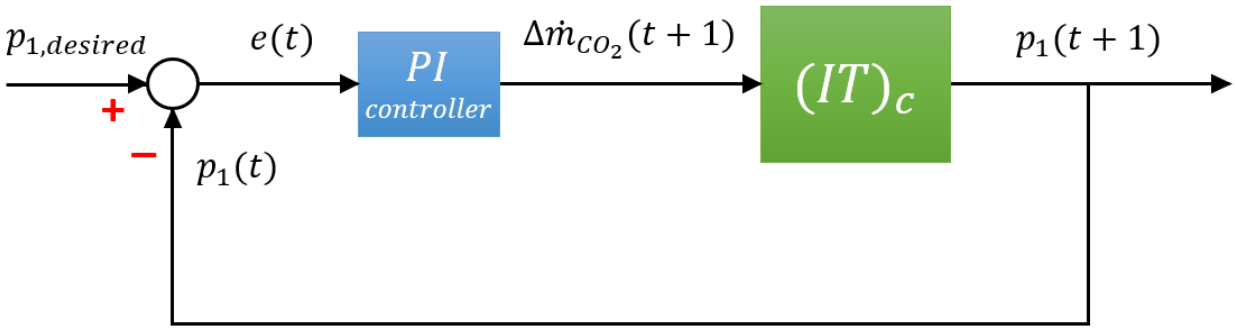

Figure 3.37: Inventory tank controller

Temperature control

For the same reasons as for the compressor inlet pressure, the compressor inlet temperature must be maintained sufficiently low. For this, the mass flow of the coolant (water) is controlled at the cold source heat exchanger level. By increasing this mass flow $\dot{m}_{H_2O}$, one can reduce this compressor inlet temperature and achieve desired CO_2 fluid properties.

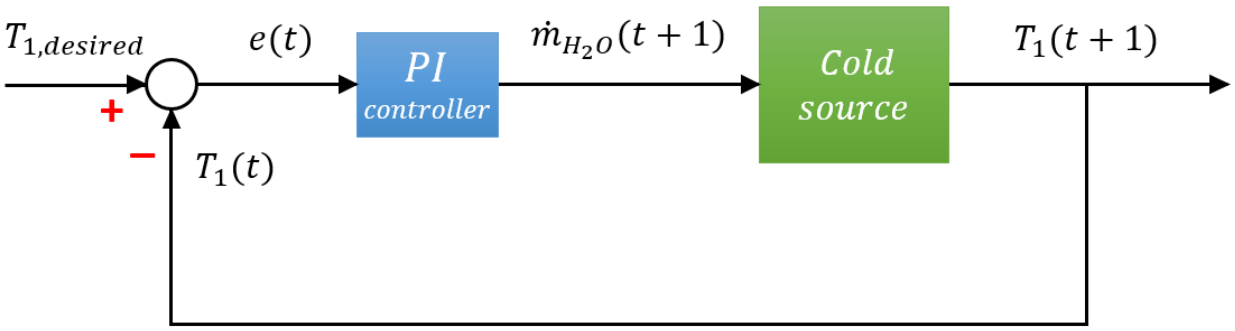

Figure 3.38: Cold source controller

Rotational speed control

To maintain the rotational speed of the shaft at a desired value, the control is put on the power load applied to the shaft. By increasing the power load, the resulting rotational speed increases or decreases depending on the difference between the power at the turbine and the sum of the power load and power needed at the compressor.

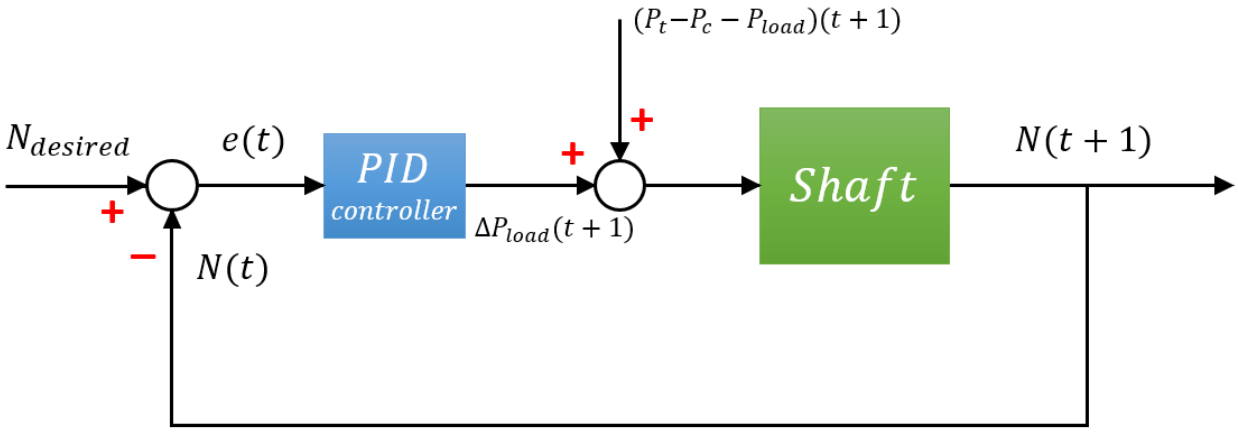

Figure 3.39: Shaft controller

3.8 Global model

The assembled blocks are represented on Fig. 3.40. One should note that the all the pressures p_2, p_3, p_5, p_6 are all computed thanks to p_1 and p_4 and the mass flow rates $\dot{m}_c$ and $\dot{m}_t$ with the pressure losses correlation as explained in Section 3.2.1. Furthermore, the inlet temperatures of the exhaust and water as well as their mass flow rates are represented in grey since they are either boundary conditions and fixed (as the exhaust mass flow rate, inlet temperature and water inlet temperature) or control variables (such as water mass flow rate).

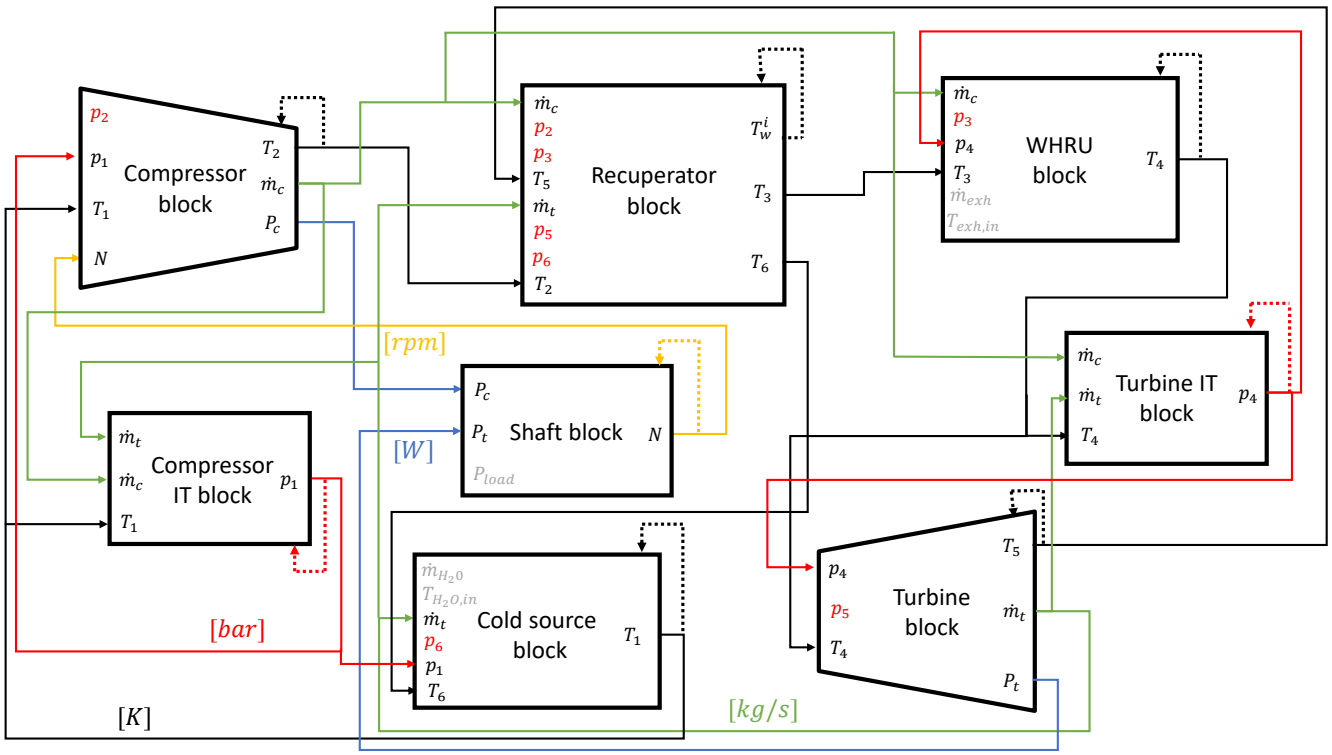

Figure 3.40: Global physical model

This figure is represented taking the full page space for more clarity in Appendix A.

CHAPTER 4

Numerical model

4.1 Introduction

In this short Chapter, the sequential procedure used to solve the different equations of the different blocks is explained.

4.2 Sequential solving procedure

The sequential procedure used for the $s - CO_2$ bottoming cycle model is shown on Fig. 4.1.

To start, the state variables steady state initial values are computed for given initial conditions. The choice of guess conditions is important since it influences the oscillatory behavior of the system during the first time steps of the sequencing procedure. Hence the steady state values found for each mGT flue gas profiles analyzed in this thesis (see Chapter 6) should be remembered to serve as initial conditions for future solving procedures to avoid this oscillatory behavior. After the initialization of the states variables, the sequential process is engaged. One should note that the thermodynamic library used for the CO_2 and other fluid properties (water and composition of the exhaust gases) is *CoolProp* [10].

4.3 Time step and performances

In dynamic analysis,the time step selected has to be smaller than the smallest characteristic time of the phenomena modelled in the cycle to ensure numerical stability. Henke et *al.* [31] showed that the limiting factor for the Δt was related to the dynamics involved with mass conservation equation. They used a time step of $0.5\,[ms]$ in their solver. A. Laterre showed that for the dynamic simulation of the Turbec T100 a time step of $100\,[ms]$ gives the same results while maintaining the numerical stability [40]. In our analysis the smallest volume considered is of 15 liters. To reduce the numerical complexity and the calculation to simulation time ratio, the time step has been increased to $50\,[ms]$ without changing the results of the analysis or encountering numerical instability. The time ratio for the simulation tool developed is then of about 0.375, allowing real time simulation.

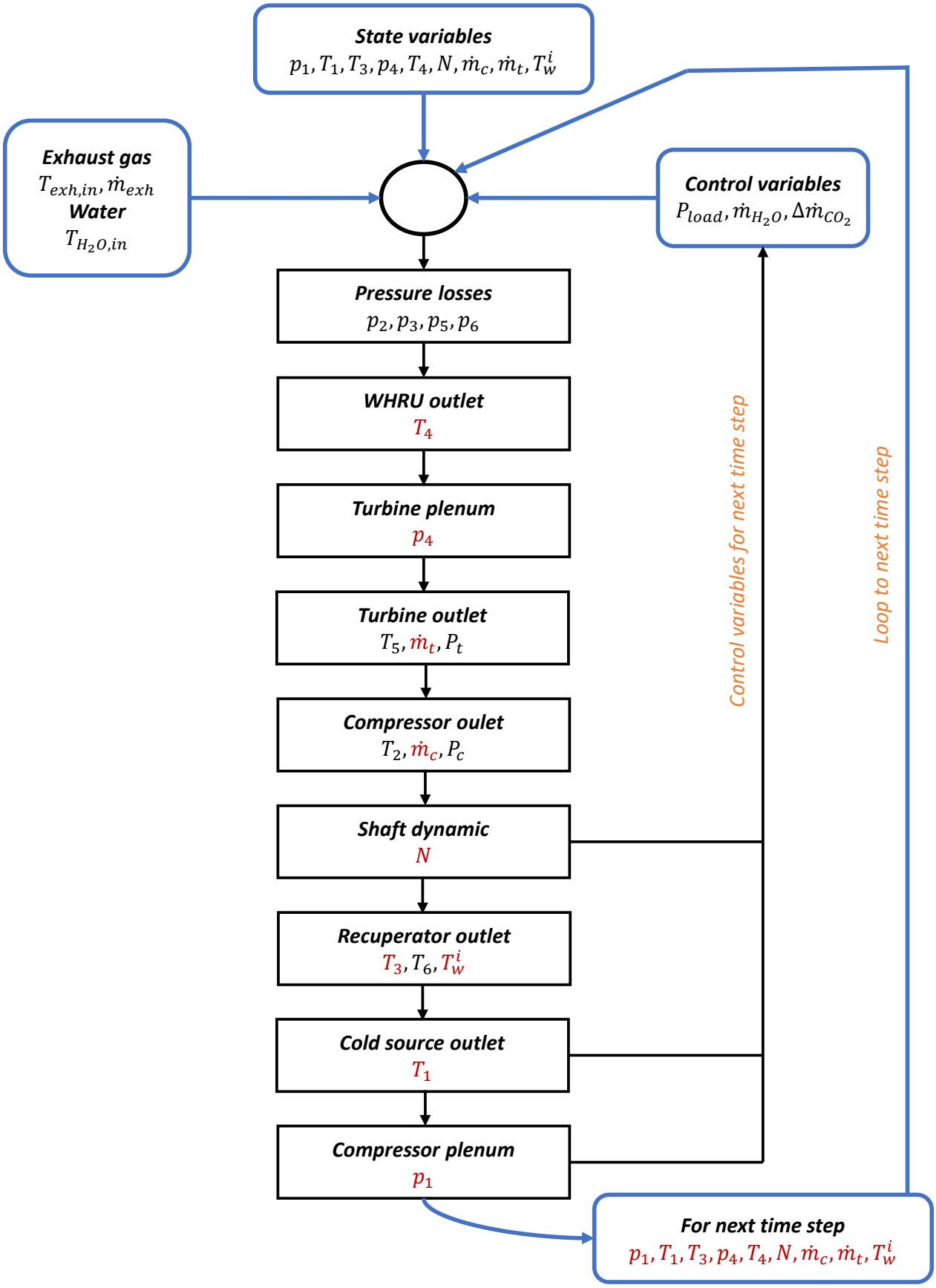

Figure 4.1: Iterative procedure for the $s - CO_2$ cycle model

CHAPTER 5

Estimation and tuning of the parameters

5.1 Introduction

This Chapter introduces the choice and tuning of the various parameters used in the modeling of the cycle. The work of this thesis is only the first step into a iterative process. The purpose of this work is to provide a first estimation of the transient behavior of a bottoming supercritical cycle for waste heat recovery, hence its accuracy must be proven afterwards. This serves as a basis for potential future construction of such an installation where the hypothesis and values of the parameters taken could be verified allowing for more precise tuning of these parameters and assessment and correction of the hypothesis taken. Hence the values discussed in this chapter only serve as an approximation.

5.2 Pressure losses

In this Section the γ coefficient used in equation (3.5) for pressure losses will be determined. This parameter depends on the design of the installation through factors like the diameter and roughness of the pipes. There is then no optimal value and it has to be tuned based on existing installations and testing facilities. First the relative pressure losses in the heat exchangers (a in equation (5.1)) are determined based on literature.

$$\Delta p = a\, p_{in} \tag{5.1}$$

The articles [22, 53, 63, 81] all analyse the dynamic behaviour of $s - CO_2$ cycles. Those four articles validated their results with an experimental facility. The relative pressure losses at each heat exchanger include the pressure losses caused by singular losses and regular losses due to piping between the components.

Four coefficient must be determined to model the pressure losses of CO_2 at the hot heat exchanger, cold heat exchanger, at the hot side of the recuperator and at its cold side. The Figure 5.1 shows the relative pressure losses considered by the researchers in those articles at the nominal conditions. In the article of T. Deng et *al.* [22], the two recuperators have been considered, hence the column Deng HTR.

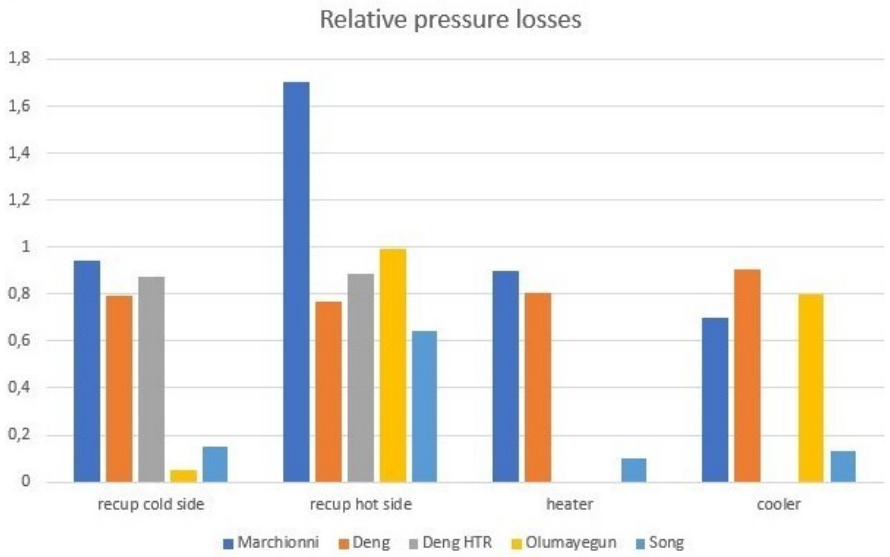

Figure 5.1: Relative pressure losses in [22, 53, 63, 81]

Based on those articles the relative pressure loss is chosen. The value considered is indicated on Tab 5.1. The gamma coefficient has been computed at nominal mass flow of 0.77 $[kg/s]$ (mass flow of the cycle when the mGT works at a load of 100 $[kW]$) in equation (5.2).

$$\gamma = \frac{a}{\dot{m}^2_{nominal}} \tag{5.2}$$

Heat exchanger	Relative pressure losses [%]	γ [-]
Cold side recuperator	0.8	0.0135
Hot side recuperator	0.9	0.0149
Heater	0.8	0.0135
Cooler	0.7	0.0118

Table 5.1: Pressure losses in heat exchangers

5.3 Shaft inertia

As the control strategy used in the analysis of the cycle consist in keeping the rotational speed of the turbomachinery constant, the modeling of the inertia of the shaft is useful in the design of a constant speed load controller at Section 3.7. In dynamic modeling studies, the value of the shaft moment of inertia can be obtained from experimental measurement. However it is most of the time tuned inside the model to match experimental results. Even in the field of micro gas turbine modeling, the estimation of the shaft inertia is a difficult process as it can vary from one study to another even for the same machine [40].

At the testing facility of Sandia National Laboratories (SNL), the rotor shaft dynamic of a Turbine Alternator Compressor unit (TAC) has been investigated. The moment of inertia of their design was of $I = 0.0022\,[kg\,m^2]$ [90]. They precised that the thrust bearing surface could be increased in their next design to allow for greater thrust load capability and for the

inclusion of magnetic thrust bearings, resulting in an increase of the inertia of the shaft. In the absence of additional data on the shaft moment of inertia of $s-CO_2$ turbomachinery, their value will be used.

5.4 Inventory tanks volume

The volume of the inventory tank influences the dynamic of the cycle. Its high volume compared to the rest of the cycle allows for a regulation of the inlet pressure of the compressor, avoiding detrimental effect on the compressor operation during addition or withdrawal of mass of CO_2 in the system. It also increases the thermal inertia before the compressor.

In *"Transient analysis and control of a heat to power conversion unit based on a simple regenerative supercritical CO_2 Joule-Brayton cycle"*, M. Marchionni et *al.* investigated the inventory control strategy on the $s-CO_2$ experimental facility at Brunel University London, whose scale is of about 60 $[kW]$. Their conditions for the inlet of the compressor are similar to the ones considered in this study except for the nominal mass flow rate of CO_2 who amounts to 2.1 $[kg/s]$ in their study for about 0.77 $[kg/s]$ in this thesis. The volume they used for the inventory tank is of 0.165 $[m^3]$, and the system inventory has been varied between 20 and 60 $[kg]$ of CO_2.
The volume selected in this thesis is of 0.043 $[m^3]$, which represents an inventory of 12 $[kg]$ in the tank at design pressure and temperature (p_1, T_1), which are the same as the ones of M. Marchionni. A reduction of the volume of the tank allows for faster transient response and a reduced volume of the installation, at the cost of a less stable operation of the compressor.

For the mass conservation equation of the plena before the turbine and compressor, the volume of heat exchanger and piping system has been estimated to 0.015 $[m^3]$. M. Marchionni showed that the inventory tank contained about half the mass of CO_2 in the cycle. Due to the higher density of the fluid after the compressor, assuming same volume in the cold and hot heat exchangers lead to the latter volume. The selected volume ensures a numerical stability of the simulation tool with a time step of 0.05 $[s]$.

5.5 Turbomachinery casing mass

In order to represent the thermal inertia effect of the exit temperature of the turbine and compressor, a heat accumulator is used. It is modeled using the heat capacity of the casing of the turbine and compressor, respectively $m_{cas,T}\, c_{cas}$ $[kJ/K]$ and $m_{cas,C}\, c_{cas}$ $[kJ/K]$.

In [83], Visser et *al.* highlighted the importance of considering the thermal effects on the turbomachinery for small scale turbines due to the high surface-to-volume ratios. However they showed that the transient response is mostly dictated by the recuperator heat capacity. The casing heat capacity influences the time requires to reach steady state. They showed that 0-D and 1-D approaches are limited and requires a fine tuning of the $m_{cas}\, c_{cas}$ term to be matched with available experimental data.

The choice of those parameters is made based on dimensional analysis. They have been chosen to ensure numerical stability of the model but needs to be validated using transient experimental data. In its numerical model of a mGT, R. Govaerts [29] selected a heat capacity of 12.25 $[kJ/K]$, while Henke et *al.* [31] estimated it at 61.1 $[kJ/K]$. In this work the casing

heat capacity of the turbomachinery should be smaller than the ones used for the modeling og the mGT turbine and compressor. Indeed, the size of the components of a $s-CO_2$ cycle are considerably reduced compared to gas turbines due to the high density of the fluid. Typical $s-CO_2$ turbines of the scale of a few tens of kW have a diameter between 40 and 72 $[mm]$ [15, 30, 53, 75]. The casing heat capacity is estimated to 2.5 $[kJ/K]$ for the turbine and compressor, which represents a casing mass of about 5 $[kg]$ of steel.

5.6 Controller gains

The controllers described in Section 3.7 require a tuning of the gains. For a PID controller the gains are defined as

$$u(t) = K_p\left(e(t) + \frac{1}{\tau_i}\int_0^t e(\tau)d\tau + \tau_d\frac{de(t)}{dt}\right) = K_p e(t) + K_i\int_0^t e(\tau)d\tau + K_d\frac{de(t)}{dt} \tag{5.3}$$

with u the control function and e the error value of the process variable. The derivative action is not used in general because of its sensitivity to high frequency noise (a filter is then needed), and the increased complexity in the tuning of the gains. Tuning PI controllers is a difficult problem, and it is often done manually following rules of good practice. There exists methods to automatically tune the controller that minimize a certain criterion. The ITAE (Integral of Time and Absolute Error) minimization method has been used to have a first guess on the controller gains for the low temperature control. It minimizes the integral of the time weighted absolute error:

$$ITAE = \int_0^t \tau|e(\tau)|d\tau \tag{5.4}$$

To tune the gain of the controller, there are tables with the optimal gains to minimize this criterion for a first order system with dead time. The open loop behaviour has then to be approximated to a first order system as a first approach. To get the open loop behaviour, a step on the control variable has been imposed from $\dot{m}_{H_2O} = 1.6\,[kg/s]$ to $\dot{m}_{H_2O} = 1.2\,[kg/s]$ at $t = 0$. The resulting change in temperature T_1 is shown on Fig. 5.2. The process gain is defined as the ratio between the difference in the control variable and the difference in process variable after steady state is achieved:

$$PG = \frac{\Delta T_1}{\Delta\dot{m}_{H_2O}} \tag{5.5}$$

In this case it amounts to -1.288. The process time constant TC is defined as

$$TC = 0.9(t_{0.75} - t_{0.25})\,, \tag{5.6}$$

with $t_{0.75}$ and $t_{0.25}$ the time needed for T_1 to reach respectively 75 % and 25 % of $T_{1,max} - T_{1,t=0}$. The settling time for T_1 is quite important compared to the one of the other temperatures of the cycle due to the casing mass associated to the cold heat exchanger, as explained in Section 5.9. Based on a table of coefficients from [62], who analyses different tuning methods, the gains of the controller have been computed. The resulting gains are $K_p = -3.7$ and $K_i = 0.68$.

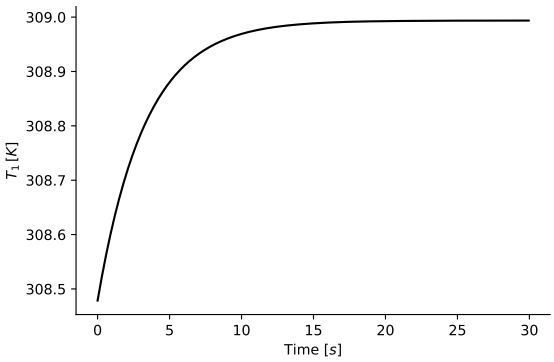

Figure 5.2: Open loop response of a change of $\dot{m}_{H_2O}$ from 1.6 $[kg/s]$ to 1.2 $[kg/s]$

Because the optimal behaviour in the cycle is not always the ITAE one, the gains have been tuned manually. Indeed, for the control of the temperature, a significant deviation (more than 1 $[K]$ basically) from its set value is not accepted as it has a high influence on the compressor stability. Moreover a variation in pressure at p_1 was not considered during the open loop analysis. The direct implementation of this controller resulted in an unstable response for T_1. To increase the stability, the gain of the process have been decreased, following the advice of Åström, K. J. For the low temperature control the gains have finally been tuned as $K_p = -0.15$ and $\tau_i = 10$. The control action u is in this case the change in mass flow rate of the water of the cold source, that has to be increased if the measured temperature T_1 is higher than its set value, hence the negative gain.

The inventory controller has been tuned using the same methodology, and the final gain selected is $K_p = 0.9e^{-5}$ and $\tau_i = 2.8$. The time scale of the controller for the inventory control has been set to 1 $[s]$. The control variable is then actualised only every seconds. The valve dynamic have not been modeled and the mass flow rate of CO_2 in the cycle is then instantaneously changed.

For the rotational speed of the shaft, the frequency experimental method has been used to tune the gains. It is done by using a P controller and increasing K_p until the limit of stability is reached. This gain is called K_u and was equal to 0.055. At the limit of stability the process variable shows a constant oscillation with period T_u, which is 20 $[s]$. Then the gains are determined with the Ziegler-Nichols coefficients. For this controller a PID was designed to respond faster to a change in power at the turbine. The rotational speed maintained constant with $K_p = 0.033$, $\tau_i = 10$ and $\tau_d = 2.5$. The time resolution of the controller is very small because the reaction time is dictated by the electronics. It has then been set to 50 $[ms]$. Existing controllers manage to keep a shaft speed constant very precisely.

5.7 Recuperator

One of the most crucial step in heat exchanger modeling is the estimation of the heat transfer coefficient. The model used in Section 3.4.1 uses the heat transfer coefficient of the cold and hot side of the heat exchanger. To increase the knowledge on the behaviour of recuperator, a first design of the recuperator has been proposed. This physical design allows for a more precise knowledge of the characteristics of the fluid inside the heat exchanger and of the geometry of the recuperator. It will be used to estimate the (UA) value at the cold and hot side as well as the casing mass of the recuperator used in dynamic modeling.

The recuperator is assumed to be a PCHE exchanger with a zigzag configuration. As

explained in Section 1.3.2, this design is the most used for $s-CO_2$ recuperators. To limit the pressure losses in the recuperator the Reynolds number of the fluid should not be too high. According to Li et *al.* [48], this Reynolds number should be limited to 30000.

To estimate convective heat transfer coefficient, the Nusselt number is often used (see equation (5.11). Various empirical correlations have been proposed to estimate the Nusselt for straight and zigzag channels [48].

The correlation used in this thesis is the Gnielinski one. Indeed, [54] showed that in the absence of data on heat exchanger performance from experimental test the Gnielinski correlation performs better in predicting manufacturers data in the range of Reynolds number we are interested in ($20000 < Re_d < 30000$). It is also the correlation that gave the best results when comparing our results with 3-D CFD from [53]. It stays valid at Reynolds number up to 60000 and at Prandtl number higher than one, which is an important factor as at design conditions the local Prandtl number at the lowest temperature of the recuperators is close to 1.85. Correlations for Nusselt number and friction factor are shown on equation (5.7) and (5.8).

$$Nu = \frac{\frac{f}{8}(Re_d - 1000)Pr}{\left(1 + 12.7(Pr^{2/3} - 1)\sqrt{\frac{f}{8}}\right)}, \tag{5.7}$$

with

$$f = \frac{1}{(1.8\log_{10}(Re_d) - 1.5)^2}\,. \tag{5.8}$$

5.7.1 Recuperator Design

Because of the lack of reference in the literature on recuperators designed for $s-CO_2$ cycles for small scale application that could be used to tune our model, we decided to design our own recuperator. Indeed, most of the studies on recuperators use experimental results of larger scale heat exchanger or CFD simulation of elementary heat transfer unit as in [54]. Moreover it will allow us to gain knowledge on the physical characteristics of the recuperator. The casing mass of the recuperator will be estimated as the mass of the recuperator designed in this section.

In [60], a study showed that reducing the recuperator effectiveness from 0.9 to 0.85 reduces the cost of the heat exchanger by 50 %. In most studies the effectiveness ranges between 0.9 and 0.95, as it represents the optimal effectiveness in term of efficiency. In this thesis the effectiveness of the recuperator will be designed to be about 0.88 at design conditions, which is considered as a good trade off between the heat duty and cost of the exchanger. This effectiveness doesn't take into account the singular pressure losses and the one occurring outside of the heat exchanger. When taking it into account in Section 6, it decreases to 0.85. To confirm the optimal value of the effectiveness, an economical analysis would be necessary. In Section 6.2, a sensitivity analysis on the impact of a change in recuperator efficiency is shown.

The model we build is based on the geometry found in [48] [54] and [61] for zigzag PCHE. It can be built based on an elementary heat transfer unit represented on Fig. 5.3. The

characteristics of this PCHE's elementary element are shown in the table 5.2. The recuperator can be modeled by assembling several elementary heat transfer units together.

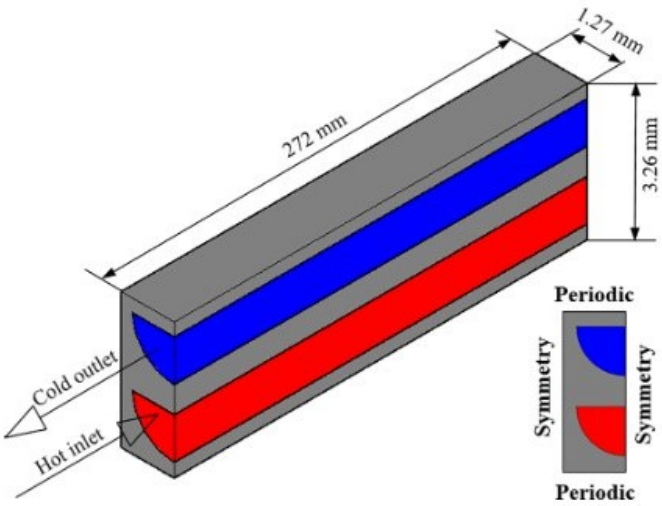

Figure 5.3: Elementary heat transfer unit of a PCHE [54]

Wetted perimeter P_w $[mm]$	5.14
Hydraulic diameter d_h $[mm]$	1.22
Cross-sectional area A_e $[mm^2]$	1.57
Length $[mm]$	272
Material	Stainless steel 316L

Table 5.2: Geometrical features and materials of the elementary heat transfer unit

To compute the heat transfer, the heat exchanger is divided into several cells along its length. At each cell, the characteristics of the fluid can be evaluated by their mean value without too much error. To characterize the convective heat transfer, the Nusselt number is computed based on the Gnielinski correlation at each cell for the hot and cold side, that express the Nusselt number as a function of the Reynolds and Prandtl numbers (see equation (5.7)). The Reynolds number is computed as

$$Re_d = \frac{\dot{m}_e d_h}{A_e \mu_i}\,, \tag{5.9}$$

with m_e the mass flow rate in the elementary channel, A_e the cross sectional area of a channel and μ_i the dynamic viscosity of the fluid evaluated at the i^{th} cell. The Prandtl number is a characteristic of the fluid that can be computed using the *CoolProp* library [10] as

$$Pr = f(\overline{p_i}, \overline{T_i})\,. \tag{5.10}$$

The convective heat transfer coefficient is obtained as

$$h_i = \frac{Nu_i k_i}{d_h}\,, \tag{5.11}$$

where $k(T, p)$ is the thermal conductivity of the working fluid that depends on the temperature and pressure of the fluid.

The heat transfer in Section 3.4.1 is computed using the wall temperature as a dynamic variable. The same model should be used to compute $(UA)_{cold}$ and $(UA)_{hot}$ during the physical design. The heat transfer at each cell for the hot and cold side is then computed based on the mean wall temperature T_w^i at this cell. The discretized recuperator can be seen on Fig. 3.28. As in [54], the discretized model has been divided into 80 cells. Compared to a discretization using 1000 cells, the error made by using 80 cells on the (UA) value is of 0.0125 [%] for the hot leg and 0.22 [%] an the cold side. This error leads to an overestimation of about 0.16 [%] of the effectiveness of the heat exchanger, with a error of 0.12 $[K]$ on the cold leg outlet temperature and 0.13 $[K]$ on the hot leg outlet temperature.

The procedure to compute the heat transfer and so the temperature and pressure all along the heat exchanger is the following:

- First an initial guess is needed for the temperature and pressure distribution at each cell. This is computed by assuming the effectiveness (see equation ((2.23)) to compute T_3 and T_6. The temperature distribution is then supposed linear with the length of the PCHE for simplicity. The pressure losses are neglected for now. The first assumption of the effectiveness will have a huge influence on the calculation time.

- Once the temperature is known, the wall temperature in steady state at each cell can be computed so that the heat flux is the same at the cold and hot side, respecting the energy conservation. To do so the temperature of the hot and cold flow are computed from left to right on Fig. 3.28. For the hot side the temperature at each cell exit is computed from the inlet temperature using the heat transfer per kg of CO_2 q_h^i as

$$T_h^{i,out} = f(p_{i,out}, h_{i,in} - q_h^i)\,, \tag{5.12}$$

  with $T_h^{0,in} = T_5$ the temperature of the hot fluid going inside the recuperator, used as an input of the calculation procedure.

  For the cold side it is computed as

$$T_c^{i,in} = f(p_{i,in}, h_{i,out} - q_c^i)\,, \tag{5.13}$$

  with $h_{i,out}$ the specific enthalpy of CO_2 in $[kJ/kg]$ at the outlet of the i^{th} cell and $T_c^{0,out} = T_3$ the temperature of the cold fluid going outside the recuperator. This temperature can not be known a priori as the input of the procedure is the inlet temperature T_2. This procedure is necessary as the heat flux $q_h^i = q_c^i$ at steady state is not known a priori. The next cell uses the temperature computed from the previous cell as $T_h^{i+1,in} = T_h^{i,out}$ and $T_c^{i,in} = T_c^{i+1,out}$.

  At the end of the process T_2 is obtained from the initial guess on T_3 and the heat load. As T_2 is a known boundary condition, an estimation of the error on T_2 is trivial. Based on this error the initial condition T_3 is modified until the error on T_2 is smaller than 0.01 $[K]$.

  The heat flux q_c^i and q_h^i are computed using Gnielinski correlation to estimate the convective heat transfer coefficient. Then the heat flux is computed as in equation (3.74):

$$Q^i = (U^i A^i)\Delta T^i\,, \tag{5.14}$$

using the same definition as equations (3.78) and (3.77) for the (UA) value.

The pressure is computed using the Darcy–Weisbach equation (3.2) with f the Gnielinski's friction factor. An iterative process is necessary on one side of the heat exchanger for the inlet pressure, just like for T_2 previously, depending on what pressure is used as input.

The intrinsic characteristics of the fluid are evaluated for each cell as the ones at the entry of the cell for the hot side and at the exit for the cold side. This assumption avoids an iterative procedure as the mean temperature on the cell depends on the heat transfer. With a number of cells of 80 considered for the characterisation of the elementary heat transfer unit, the error using this assumption is of 0.02 % on the heat load and effectiveness and 0.03 $[K]$ on the exit temperature of the cold side of the heat exchanger, which is legitimately neglected.

Validation

The model developed will be compared to a result of a 3-D CFD model for validation. The boundary conditions used in this model are shown in Tab. 5.3.

Mass flux $[kg/m^2s]$	509.3
Cold side inlet temperature T_2 $[°C]$	100
Hot side inlet temperature T_5 $[°C]$	400
Cold side outlet pressure p_3 $[bar]$	150
Hot side inlet temperature p_6 $[bar]$	75

Table 5.3: Boundary conditions used for the model comparison

The model has been validated in steady state by comparing the resulting temperature and pressure profile over the length of the heat exchanger with CFD results from [54], as shown on Figure.5.4. The deviance from 3-D CFD results for the outlet temperatures does not exceed 1.7 [%], which is way less than the experimental error.

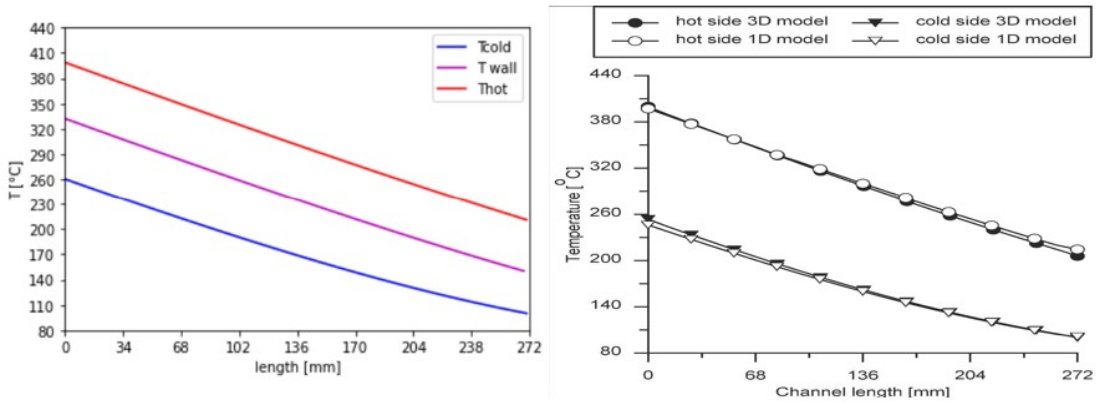

Figure 5.4: Validation of the recuperator model compared with CFD results in steady state

The recuperator has been designed as a combination of elementary transfer units presented on Tab. 5.2. The mass flow in a channel of the PCHE can be reduced by increasing the number of channels. The number of channels have been selected to obtain a Reynolds number smaller than 30000 as in [48]. To avoid heat losses it is important to minimize the area of the external walls. That is why a square design of the cross section area is preferable. Designing

the PCHE recuperator as the superposition of 24 metal plates with 34 semi circular channels etched on each plates gives a square design and satisfy the Reynolds number limitation. The length of the channels amounts to 68 $[cm]$ to reach the desired effectiveness. The mass of steel in this recuperator can be obtained by computing the core volume based on this geometry. It amounts to 22.5 $[kg]$. This mass will be used as the casing mass of the recuperator.

In practice, the model we developed could be directly used for the transient simulation. However, due to the iterative processes used it is too costly from a numerical perspective. Moreover, it shows some numerical instabilities during transient. That is why it will be used to develop a correlation for the (UA) value, used in the model explained at Section 3.4.1. It is a usual approach to use the (UA) value of a recuperator as this value is given by the manufacturer as a function of the mass flow. This is what is used in the modeling of the recuperator in [40].

The correlation for $(UA)_c$ and $(UA)_h$ is built by varying the mass flow through the heat exchanger while keeping the inlet temperature constant, equal to their nominal values for the bottoming CO_2 cycle recovering heat from the nominal exhaust of a 100 $[kW]$ Turbec T100. This value has been determined iteratively when trying to determine the (UA) of the recuperator.

$$(UA)_h = f(\dot{m}_h) \tag{5.15}$$

$$(UA)_c = f(\dot{m}_c) \tag{5.16}$$

Those correlations neglect the influence of a change of inlet temperature on the (UA) value. The error made by this assumption has been analysed by extracting the changes in operating conditions during transient and computing the corresponding (UA) value in the physical heat exchanger model. The transient profiles analysed correspond to the recuperation of the exhaust of a mGT going from 100 to 80 $[kW]$ of load and from 90 to 100 $[kW]$. Those profiles are represented in Section 6.3. Then a worst case scenario error has been analysed. The extreme values of T_2, T_5, p_2 and p_5 during those transient have been collected (see Tab. 5.4 for the considered range) and the (UA) value corresponding to any combination of those values have been computed for several mass flows.

value	min	max
$T_2\,[K]$	355.5	357
$p_2\,[bar]$	148.9	149.2
$T_5\,[K]$	440	465
$p_5\,[bar]$	76.7	76.8

Table 5.4: Extreme values considered for the error analysis $UA(m)$

The error made by expressing the (UA)value only as a function of the mass flow during the analysis of Section 6.3 has been post processed and is shown on Fig. 5.5. The maximum (UA) value (upper limit of the error bar) has been obtained with $[p_{2,min}, p_{5,min}, T_{2,max}, T_{5,max}]$ for the hot side and $[p_{2,min}, p_{5,min}, T_{2,max}, T_{5,min}]$. The minimum one is obtained when taking the other value for the inlet pressures and temperatures. The relative deviation from the correlation in [%] is of about $[-0.21, +0.58]$ for the hot side and $[-1.64, +3]$ for the cold side.

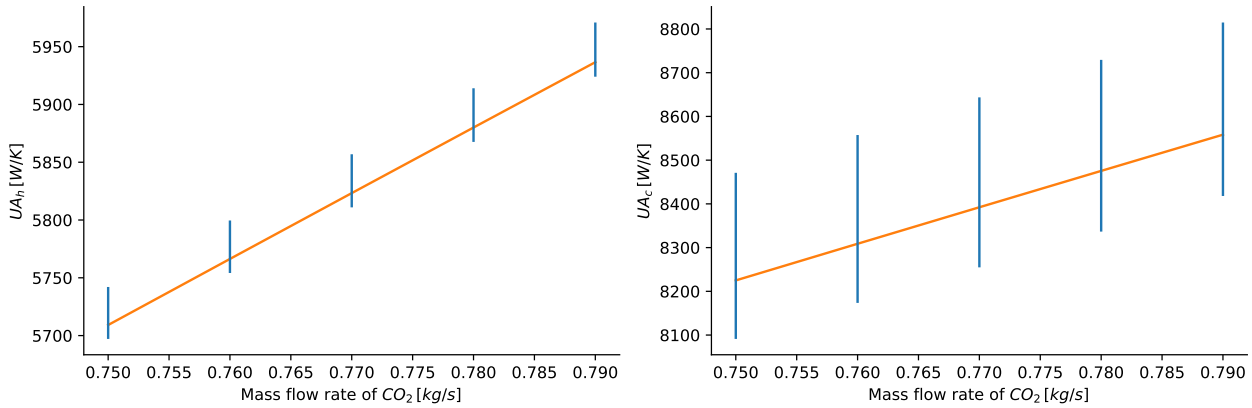

Figure 5.5: Error made using the correlation on (a) $(UA)_h$ and (b) $(UA)_h$

Despite the limited variation of temperature on the cold side compared to the hot side, the variation in (UA) is more significant. The convective heat transfer coefficient varies only a little along the length of the exchanger on the hot side $(2100 - 2210\,[W/m^2K])$ compared to the cold side $(2540 - 3700\,[W/m^2K])$ at design conditions. This is because the properties of CO_2 are more sensitive to a temperature change in the cold side. Indeed, at the cold side the high pressure of CO_2 involves a higher pseudo-critical temperature (see Fig. 1.2). The temperature being closer to this pseudo-critical temperature, the variations of properties are more significant.

5.8 Waste heat recovery unit

For the waste heat recovery heat exchanger, heater of the bottoming cycle, the characteristics of the casing $(m_{w,h}c_{w,h})$ used to represent the thermal inertia must be determined.

The material used in the manufacturing of this heat exchanger is 316 steel. Because the maximum temperature of the cycle is quite low, the use of steel is always preferred for a reduction of the manufacturing cost. The heat capacity of this material can be assumed constant at $c_{w,h} = 490\,[J/kgK]$. The mass must be determined to ensure dynamic stability of the model. It has been tuned to show the same time constant as the one of [53], defined as

$$\tau = \frac{m_{w,h}\, c_{w,h}}{UA} \tag{5.17}$$

In [53], the time constant for the heater is $\tau = 1.55\,[s]$.
At design conditions the (UA) value of the heat exchanger in steady state can be computed by integrating

$$dQ = UdA\Delta T\,, \tag{5.18}$$

ΔT being the temperature difference between the hot and the cold fluid (see Figure 5.6). This difference evolves over the heat exchanger depending on the heat exchanged, as shown on Fig. 5.6. It can be expressed as

$$\Delta T = T_h - T_c = f(Q_{exch})\,, \tag{5.19}$$

with the temperature of the hot source T_h expressed as a function of the enthalpy of the flue gas $h_{h,in} - q_h$.

$$T_h = f(h_{h,in} - q_h)\,, \tag{5.20}$$

$$q_h = \frac{Q_{exch}}{\dot{m}_{ex}} \tag{5.21}$$

Similarly for the cold side where

$$T_c = f(h_{c,out} - q_c)\,, \tag{5.22}$$

$$q_c = \frac{Q_{exch}}{\dot{m}_{CO_2}} \tag{5.23}$$

Leading to the equation (5.24).

$$(UA) = \int_0^{Q_{exch}} \frac{1}{T_h(h_{h,in} - q_h) - T_c(h_{c,out} - q_c)} dQ\,, \tag{5.24}$$

Integrating numerically using the *Scipy* library from *Python*, one can obtain a nominal (UA) value of about $3.5\,[kW/K]$. The mass of the casing can then be estimated using equation (5.17): $m_{w,h} = 11.1\,[kg]$. The value of the casing heat capacity for the heater is then $m_{w,h}\,c_{w,h} = 5.44\,[kJ/K]$.

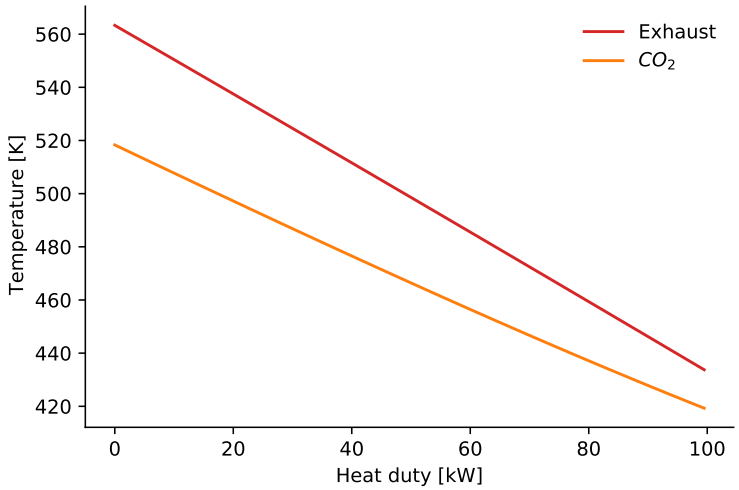

Figure 5.6: Temperature profiles of the heater as a function of the heat load

5.9 Cold heat source

For the water-CO_2 cold heat exchanger used as cooler of the bottoming cycle the lumped approach is used to represent the dynamic behaviour. This model requires a tuning of the casing mass and specific heat capacity, just like the hot heat source.

Using the same approach as in Section 5.8, the specific heat capacity is the one of 316 steel $c_{w,c} = 490\,[J/kg/K]$ and the mass is estimated using equation (5.17) with $\tau = 2.38\,[s]$.

To design the exchanger, the (UA) value must be chosen. This value depends on the design of the heat exchanger and of the acceptable flow rate of water going through the heat exchanger. Designing an exchanger with a small (UA) value will decrease its response time, volume, price and pressure losses. However it will decrease the maximum heat transfer. A better heat transfer can be achieved by increasing the mass flow of water to increase the

temperature difference between the water and CO_2. The temperature of water at the exit of the cooler will then decrease. This approach has a limit and the mass flow of water increases rapidly. As the cycle uses the mass flow of water to regulate the lowest temperature of the cycle, the exchanger must be well designed from the start. Imposing an exit temperature of 32 $[°C]$ at the hot end of the heat exchanger, a (UA) value of 2.6 $[kW/K]$ is found. The resulting mass flow rate of water is about 1.8 $[kg/s]$. Reducing T_1 is favorable for improving the net power output of the cycle but it has the disadvantage to rapidly increase the mass flow of water or the necessary (UA) of the cooler.

Using this nominal (UA), one can obtain $m_{w,c} = 12.6\,[kg]$ from equation (5.17). As explained in Section 3.4.3, the thermal inertia of the inventory tank has to be taken into account into the casing mass. At the design conditions of the inventory tank $p_1 = 75.5\,[bar]$ and $T_1 = 308.2\,[K]$, the heat capacity of CO_2 is $c_p(p_1, T_1) = 854.3\,[J/kg/K]$, its density is $\rho = 279.6\,[kg/m^3]$. The volume of the inventory tank has been design to be $V = 0.043\,[m^3]$. For the inventory tank $m\,c_p = 10.3\,[kJ/K]$, which is equivalent to the thermal inertia of 21 $[kg]$ of steel. For the cold heat source the value of the casing heat capacity is $m_{w,c}\,c_{w,c} = 16.45\,[kJ/K]$. The temperature vs heat load profile for the cold source at nominal conditions is represented on Figure 5.7.

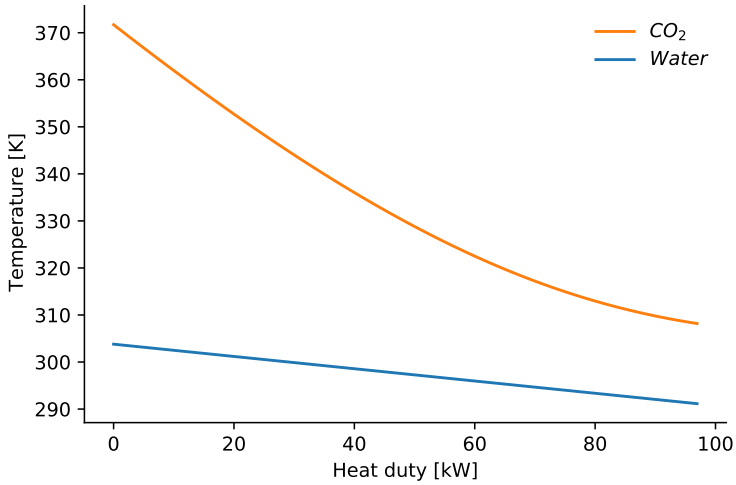

Figure 5.7: Temperature profiles of the cooler as a function of the heat load

5.10 Turbine isentropic efficiency

As explained in Section 3.3.2, the turbine is considered choked and the isentropic efficiency is assumed constant at $\eta_{is,T} = 0.84\,[-]$. This estimation of the isentropic efficiency of the turbine has been made based on literature review. For this purpose, small scale $s - CO_2$ turbines must be considered. Indeed, the small scale of the turbomachinery results in relatively large tip clearances and windage losses.

Barber-Nichols designed the $s - CO_2$ turbomachinery prototypes of about 100 $[kW_e]$ at the Sandia National Laboratory and in the Integrated System Test (IST) at the Naval Nuclear Laboratory. Those two turbomachinery prototypes are quite similar and have respectively a design isentropic efficiency of 0.85 and 0.8 for the turbine [3]. Echogen EPS100 turbine performance measurements of their 250 $[kW_e]$ prototype indicate peak turbine isentropic efficiencies just over 0.8, and comparison with modified NASA TP-1730 radial turbine performance curve suggests that this efficiency will continue to increase at full load [3]. At the KIER

experimental facility, a 12.6 $[kW]$ TAC (Turbo Alernator Compressor) unit has been tested [15] with a turbine efficiency of 0.84.

In the dynamic analysis carried out by M. Marchionni et *al.* in [53] on a 50 $[kW]$ $s-CO_2$ cycle, the performance map of the turbine shows efficiency up to 0.83. In its work on analyzing a bottoming cycle for mGT, F. Reale et *al.* considered an efficiency of 0.85. Salah et *al.* [75] worked on the design of a 100 $[kW]$ radial turbine whose design efficiency is 0.835. In [50], different layouts of supercritical CO_2 power cycles for waste heat recovery have been investigated considering an isentropic efficiency of 0.85 for the turbine.

In the end an isentropic efficiency of 0.84 has been selected for the dynamic analysis made in this thesis. A sensitivity analysis on the turbine isentropic efficiency has been carried out and is shown on Fig. 6.6 in Section 6.2 to show the impact of this parameter on the cycle performances and the gains achievable in efficiency by improving the turbine design.

CHAPTER 6

Dynamic analysis results

6.1 Introduction

In this Section the dynamic code has been used to investigate the behaviour of the designed $s-CO_2$ cycle for the recovery of exhaust gas from a mGT. First a sensitivity analysis on important parameters of the cycle has been carried out. This analysis justify the choices made during the design of the cycle and show the effect of changes in the cycle operation or design.

Then a dynamic simulation of the cycle has been made while recovering changing exhaust flow of the mGT. The exhaust given as an input for the simulation is the one obtained during a change of operation of the Turbec T100, from 100 to 80 $[kW]$ and from 90 to 100 $[kW]$. For those simulation the control strategy is the following:

- The compressor inlet temperature is kept constant at $T_1 = 308.5\,[K]$ using low temperature control.
- The compressor inlet pressure is maintained constant at $p_1 = 75.5\,[bar]$ using inventory control
- To recover the maximum power from the cycle and maintain the isentropic efficiency of the turbomachinery, the rotational speed of the shaft is kept constant at 33100 $[rpm]$

6.2 Sensitivity analysis

To control the cycle and maximize the power recovered from the mGT exhaust, it is important to select the control variables wisely. To see the effects of specific parameters on the cycle performances in steady state, different sensitivity analysis were performed. Those analysis were made on a bottoming $s-CO_2$ cycle recovering waste heat from the exhaust of the 100 $[kW]$ Turbec T100. The characteristics of this exhaust is a mass flow rate of $\dot{m}_{exh} = 0.746\,[kg/s]$ and a temperature of $T_{exh} = 563.4\,[K]$. Defining the waste heat recovery potential as the power recovered when cooling the exhaust gases to 100 $[°C]$:

$$P_{WHR} = \dot{m}_{exh}(h(T_{exh}) - h(T = 373.15\,[K]))\,, \tag{6.1}$$

the potential of recovery of this exhaust flow is of 150.5 $[kW]$. The composition considered for the exhaust gas composition is described in Section 3.2.2.

For the following analysis, the effect of a deviation from design value of different parameters will be investigated. The design value are made explicit on Tab. 6.1.

Cycle parameter	**Design value**
$T_1\,[K]$	308.5
$p_1\,[bar]$	75.5
$N\,[rpm]$	33100
$\eta_{is,T}$	0.84

Table 6.1: Design parameters used for the steady state analysis

Compressor inlet temperature

On Fig. 6.1, one can see the variation in power output of the bottoming cycle when varying the lowest temperature of the cycle T_1 with $p_1 = 75.5\,[bar]$ and $N = 33100\,[rpm]$.

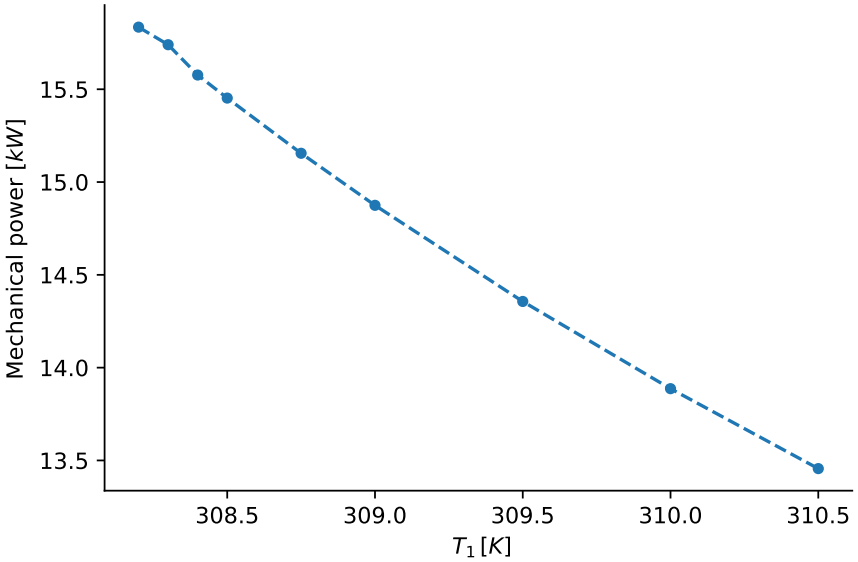

Figure 6.1: Power output of the cycle as a function of T_1

Decreasing T_1 allows a significant increase of the net power of the cycle by reducing the power consumption of the compressor. On the contrary, an increase of $1\,[°C]$ from $T_1 = 308.5\,[K]$ induces a decrease of $1.1\,[kW]$, equivalent to 7.1 % of the power output. This is explained by a reduction of the compressibility factor Z and by the fact that increasing T_1 decreases the mass flow rate and pressure ratio at the compressor, hence the power extracted at the turbine. This trend is shown in red on Fig. 6.3 by showing the pressure ratio evolution with the mass flow when changing T_1 from $308.2\,[K]$ to $310.5\,[K]$. This is why low temperature control is often used in $s - CO_2$ applications. The impact of changing the temperature at constant pressure on the compressibility factor of CO_2 is shown on Fig. 6.4 and 3.6 in Section 3.3.

Compressor inlet pressure

The effects of a change in inlet pressure at the compressor have been investigated. The pressure p_1 has been varied while keeping the temperature T_1 constant at 308.5 $[K]$. On Fig.6.2 the cycle power output is shown as a function of p_1.

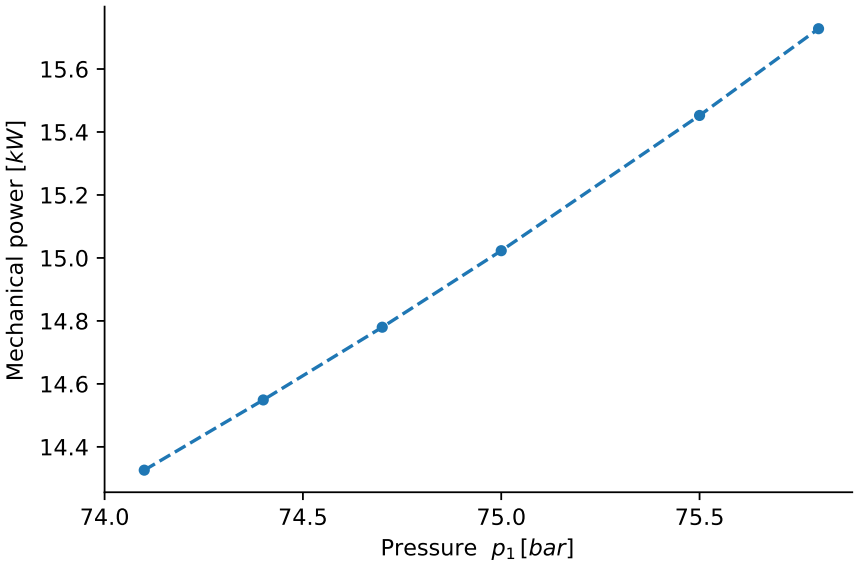

Figure 6.2: Power output of the cycle as a function of p_1

Increasing p_1 decreases the compressibility factor Z, as shown on Fig. 6.4. For the same compression ratio, the compressor specific power consumption decreases with p_1. The effect of increasing p_1 is the same as the one seen when decreasing T_1, i.e. an increase of the mass flow rate and pressure ratio at the compressor. In the range of pressure and temperature considered on Fig. 6.1 and 6.2, the pressure ratio of the compressor as a function of the mass flow rate of CO_2 has been plotted on Fig. 6.3.

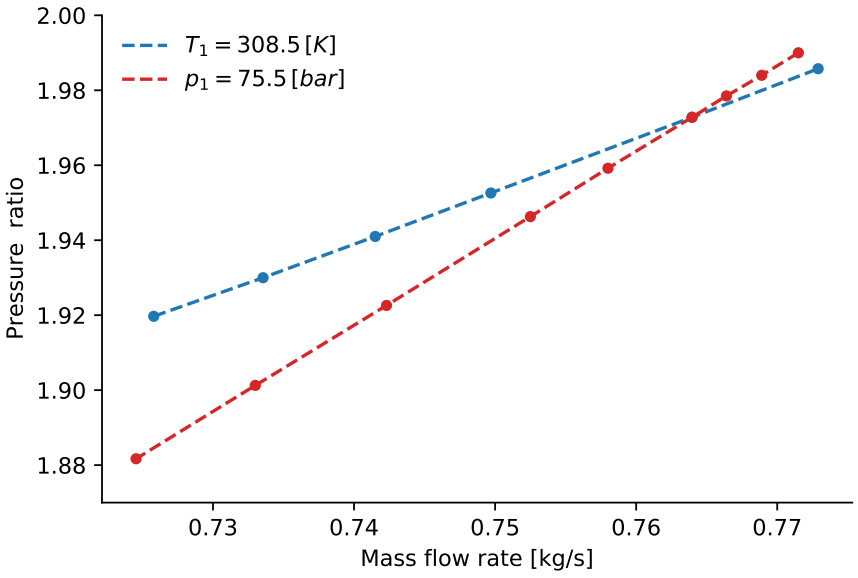

Figure 6.3: Pressure ratio as a function of the mass flow rate when varying the CIP (blue) and CIT (red)

The increase in power output of the bottoming cycle when increasing p_1 can be explained by a reduction of the compressibility factor Z at the compressor entrance due to the changing characteristics of $s - CO_2$, reducing the compressor work for the same turbine work. It explains why the cycle efficiency increases despite a decrease of the turbine inlet temperature shown on Fig. 6.5. The change of Z has been plotted on Fig. 6.4, where the blue dots are the investigated pressures p_1. It can be seen on that image that the properties of $s - CO_2$ are not fully used. The operating point is in the vapour-like supercritical fluid region, as explained in Section 3.3.1, so before the reduction of compressibility factor occurring in the pseudo critical region. On a T-s diagram the compressor inlet state is on the right of the critical point.

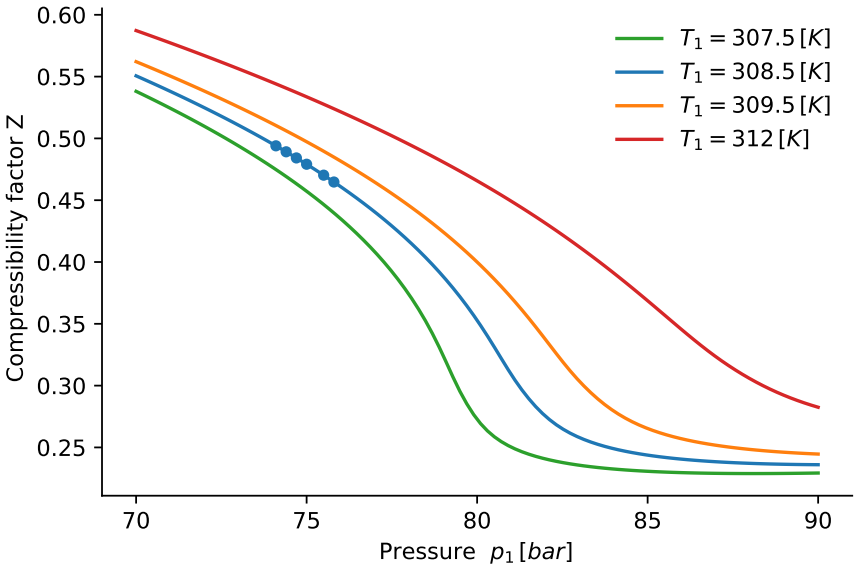

Figure 6.4: Variation of the compressibility factor Z as a function of pressure and temperature

A lower compressibility of about 0.25 can be achieved by increasing the lowest pressure or decreasing the temperature to have a liquid like supercritical fluid behaviour, and it would reduce even more the specific power consumption of the compressor. However it would induce a mass flow rate of CO_2 that is too big for our application. Decreasing T_1 increases the reduced mass flow and decreases the Z. Decreasing Z increases the maximum mass flow rate but also decreases the maximum pressure ratio achievable. If the mass flow rate is imposed at the compressor, decreasing T_1 brings the operating point closer to the surge line, due to the modification of the compressor map taking real gas behaviour into account. Moreover the approximations used during the modeling of the compressor are not valid in the liquid like supercritical region where the Z is too small.

To analyse the gain achievable in efficiency when decreasing Z, the cycle has been tested in steady state with an increased mass flow rate. The mass flow rate f the exhaust flue gas has been doubled and the TIT of the bottoming cycle has been conserved at 522.8 $[K]$, conserving the specific heat addition at the hot source (same WHR efficiency). The impact of decreasing Z to 0.322 by decreasing T_1 to 306.13 $= T_{crit} + 2\,[K]$ and increasing p_1 to 76.84 $[bar]$ is an increase in cycle efficiency from 15.04 % to 22.2 %. This is partly due to an increase of the compression ratio, increasing the turbine specific power from 46.57 $[kW/kg]$ to 58.71 $[kW/kg]$. At same Z, increasing the compression ratio would also increase the specific power consumption of the compressor. However it is reduced from 26.34 $[kW/kg]$

at $Z = 0.47$, $PR = 1.97$ to 26.17 at $Z = 0.332$, $PR = 2.4$. The comparison has been made with a constant isentropic efficiency. This analysis shows that the turbomachinery considered in this thesis is not well adapted to the small scale $s - CO_2$ cycle analysed, for which the pressure ratio and mass flow rate are limited. It has been used by scaling an existing compressor map of mGT, because of the absence of existing adapted compressor map available.

Inventory control consists in varying p_1 by changing the density at the inlet of the compressor by changing the total mass of CO_2 in the cycle. Varying p_1 allows a control of the turbine inlet temperature, an important parameter to enhance the cycle efficiency, without changing the rotational speed of the turbine. It allows a better conservation of the turbine isentropic efficiency at part load [53]. Fig.6.5 shows the variation of the TIT with a variation of p_1 in the cycle analysed. The linear behaviour eases the implementation of a controller. The range of control is quite limited and a control of T_1 or of the pressure ratio is necessary to increase the controllability of the cycle.

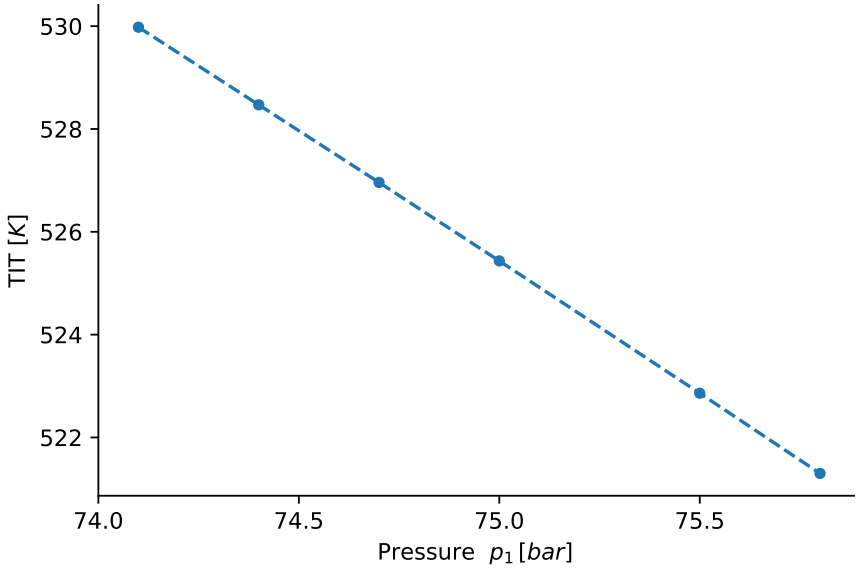

Figure 6.5: Variation of the turbine inlet temperature (TIT) as a function of the pressure p_1

Turbine isentropic efficiency

To show the potential improvement of $s - CO_2$ cycle with an increase of the isentropic efficiency of the turbine and to show the impact of a miss estimation of the turbine efficiency, a sensitivity analysis on $\eta_{is,T}$ has been performed. The impact on the turbine specific power and the resulting change in efficiency of the cycle are shown on Fig. 6.6. This parameter has a huge impact on the cycle performance and research on this field are important to enhance the efficiency of $s - CO_2$ cycles. From the exhaust gas thermal power available for waste heat recovery (P_{WHR}) and the power extracted at the bottoming cycle (P_m), the total efficiency can be extracted, defined as

$$\eta_{tot} = \frac{P_m}{P_{WHR}} = \eta_{cycle}\eta_{WHR}\,, \tag{6.2}$$

with

$$\eta_{WHR} = \frac{P_{hot}}{P_{WHR}}\,, \tag{6.3}$$

$$P_{hot} = \dot{m}_{CO_2}(h_4 - h_3)\,, \tag{6.4}$$

$$\eta_{cycle} = \frac{P_m}{P_{hot}} \,. \tag{6.5}$$

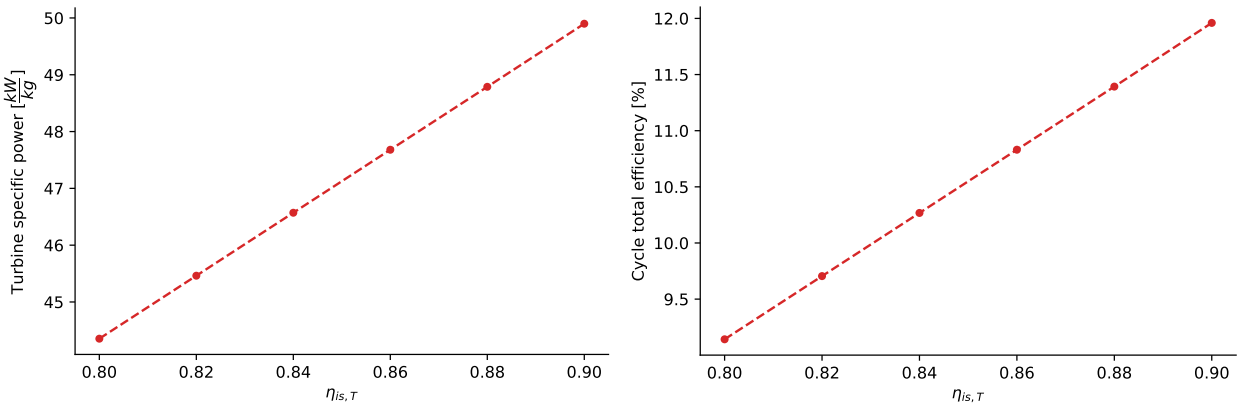

Figure 6.6: (a) Specific power at the turbine and (b) resulting η_{tot} when varying the turbine isentropic efficiency

Recuperator effectiveness

The recuperator is one of the main components of the cycle, improving the internal efficiency of the thermodynamic cycle. Improving its effectiveness is made by increasing its length and is associated with an increase in capital cost. The impact of its effectiveness is assessed in this Section.

To analyse its impact, the effectiveness of the recuperator as been changed by increasing the recuperator length in the physical design while conserving the same pressure losses. A new correlation $UA(\dot{m})$ is found and used to quantify the effect on the whole cycle. The other parameters of the cycle are kept constant at the design value (see Tab. 6.1). The effectiveness of the recuperator has been recomputed to take the effective pressure losses into account, computed based on the correlations from Section 5.2. At the design conditions, the effectiveness of the recuperator amounts to 0.852. As shown on Fig. 6.7, increasing the effectiveness increases the net power output of the cycle. The gain in efficiency of the bottoming cycle is way smaller than the one obtained when increasing the turbine isentropic efficiency (see Fig. 6.6). However the turbine isentropic efficiency cannot be increased easily, while the recuperator effectiveness results from a design choice, trade off between investment cost, pressure losses and heat duty.

The internal efficiency of the cycle is increased (see Fig. 6.7) because of the higher heat duty at the recuperator, decreasing the losses at the cold source (see Fig. 6.9). A side effect is an increase of the temperature at the inlet of the waste heat recovery heat exchanger, reducing the quality of the heat transfer at the heater of the cycle. Less energy can be extracted from the flue gases due to the reduced temperature difference, decreasing the WHR efficiency of the bottoming cycle (see Fig. 6.8). Overall there is a net gain in efficiency when increasing the effectiveness. However it is associated with an increase in the recuperator size, and then increases the capital cost, the casing mass for transient operation and the pressure losses. In this study the increase in pressure losses has not been modeled, but other studies show that due to its effect there exists an optimum in term of power recovering [48, 74], at an effectiveness between 0.9 and 0.95 depending on the specific cycle and on the design of the pipes impacting the pressure losses.

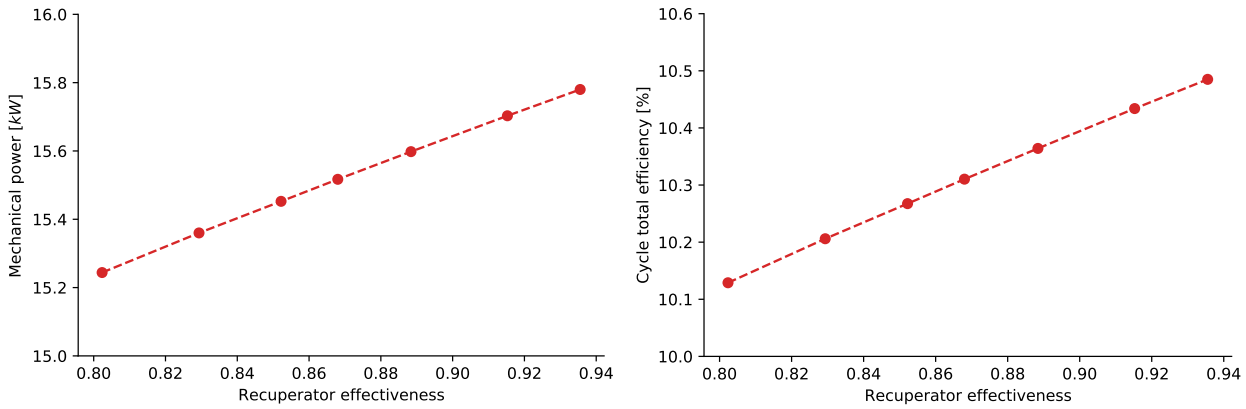

Figure 6.7: Change in power output of the cycle when varying recuperator effectiveness and resulting η_{tot}

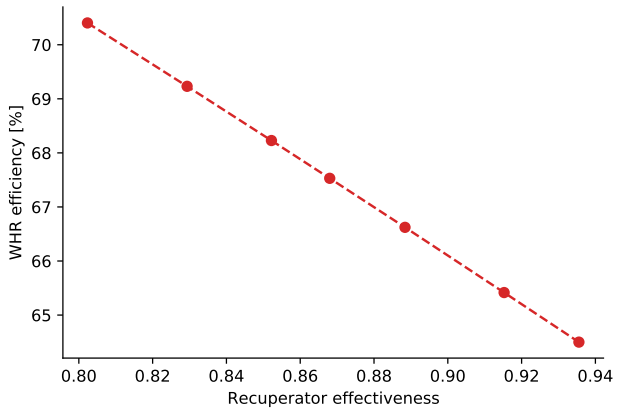

Figure 6.8: Waste heat recovery efficiency vs recuperator effectiveness

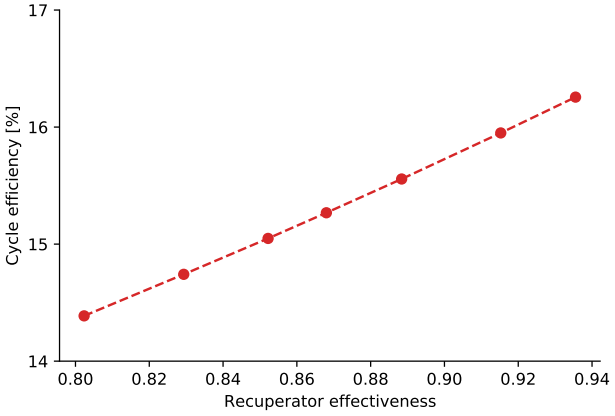

Figure 6.9: $s - CO_2$ cycle efficiency vs recuperator effectiveness

6.3 Dynamic analysis

In this Section, the recovering from the exhaust gases of a Turbec T100 during transient operation has been analysed. Two profiles will be presented, the decreasing step induces by a change of load from 100 $[kW]$ to 80 $[kW]$ and the increasing step from 90 $[kW]$ to 100 $[kW]$. The resulting exhaust gases characteristics are shown on Fig. 6.10 for the $100 - 80\,[kW]$ transient and on Fig. 6.11 for the $90 - 100\,[kW]$ transient. From the mGT perspective, an increasing step in the power load is not problematic in term of compressor surge. Indeed, it is associated with an overshoot in reduced air flow, increasing the surge margin during transient. That is why the step in mass flow of the exhaust is sharper than in the situation with a decreasing step. The profile of temperature and mass flow of this exhaust is depicted on Fig. 6.11.

Originally 800 seconds of transient were available but the first 100 seconds were not represented in this analysis because they are used to reach a steady state regime from the initial conditions of the $s - CO_2$ cycle. The variations present during this lapse of time are not physically representative as they are induces by a non-matching of the initial conditions with the steady state conditions. To run the simulation, 300 seconds of CPU time with $dt = 0.05\,[s]$ were needed to run 800 seconds of cycle.

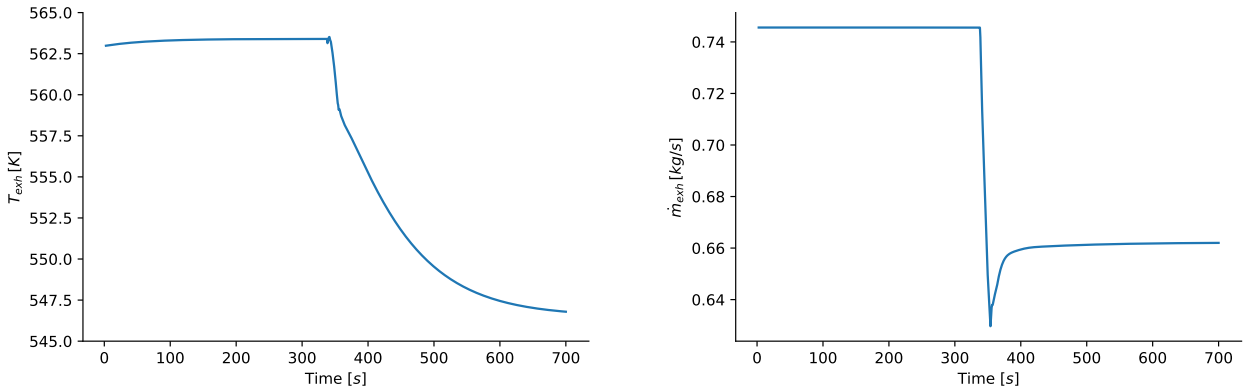

Figure 6.10: (a) Temperature and (b) mass flow rate profile of the exhaust gases during the $100 - 80\,[kW]$ transient maneuver

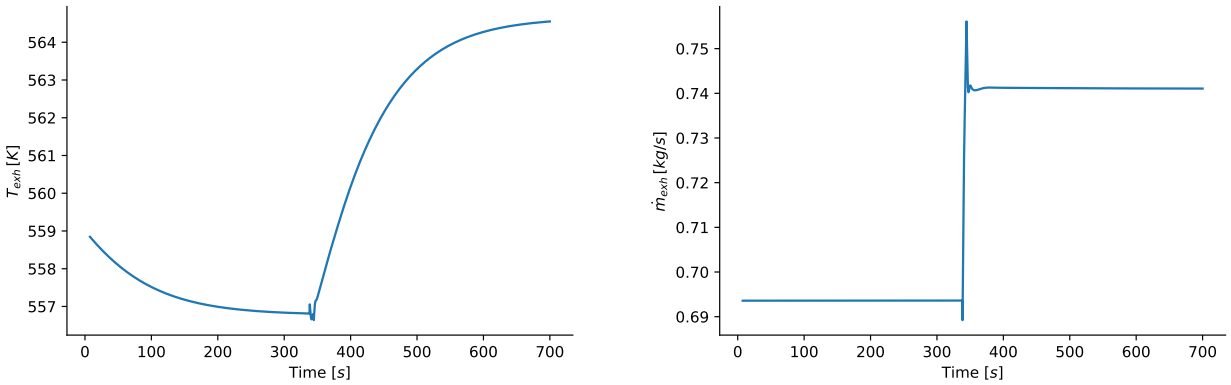

Figure 6.11: (a) Temperature and (b) mass flow rate profile of the exhaust gases during the $90 - 100\,[kW]$ transient maneuver

Three steady state results have been computed with the model for the load points of mGT considered during the dynamic analysis: 80, 90 and $100\,[kW]$. The resulting T-s diagrams are represented on Fig. 6.12. It is clear here that the compressor inlet has a vapour-like behaviour because it is in the supercritical region on the right of the supercritical point. The operating conditions stay the same for the three cycle except for the TIT and turbine outlet temperature that decrease with the available power.

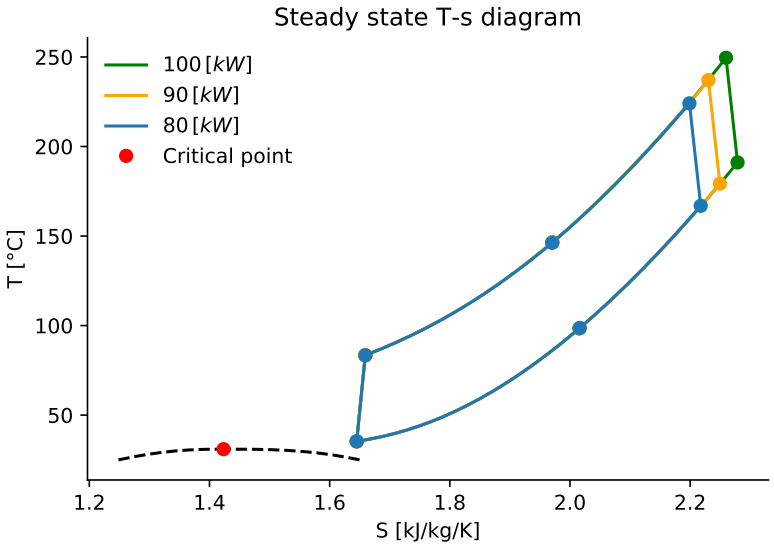

Figure 6.12: T-s diagram of the bottoming $s - CO_2$ cycle for different loads of the mGT

The operating point of the compressor is represented on Fig. 6.13. The map has been built to consider real gas behaviour, varying with Z and the isentropic exponent n_s.

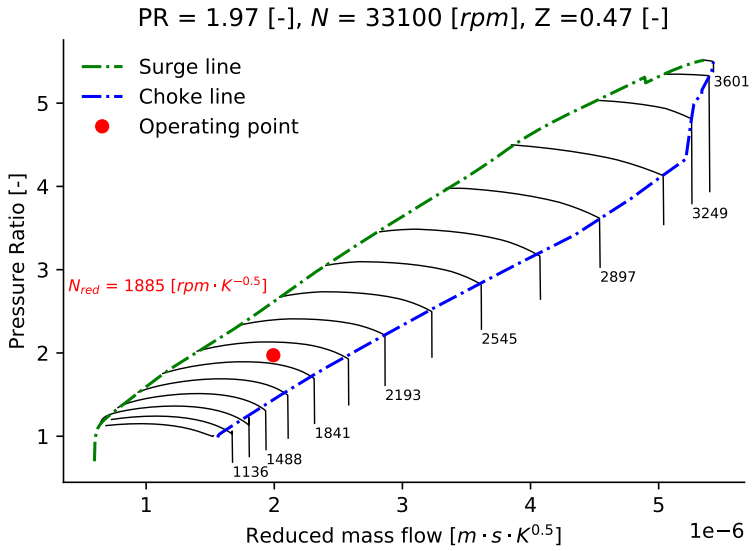

Figure 6.13

The boost in power output of the mGT installation due to the addition of a $s - CO_2$ bottoming cycle has been represented on Fig. 6.14. The relative increase in efficiency of the mGT is of 15.5 % for the load of 100 $[kW]$, of 15.8 % for the 90 $[kW]$ and of 16.25 % for the 80 $[kW]$. The mGT efficiency at 100 $[kW]$ of mGT electrical load is then boosted from 30 % to 34.65 %. The increase in bottoming cycle efficiency when decreasing the load shows that better efficiency could be reached with a better selection of the cycle control parameters. An better optimisation of steady state operations is possible.

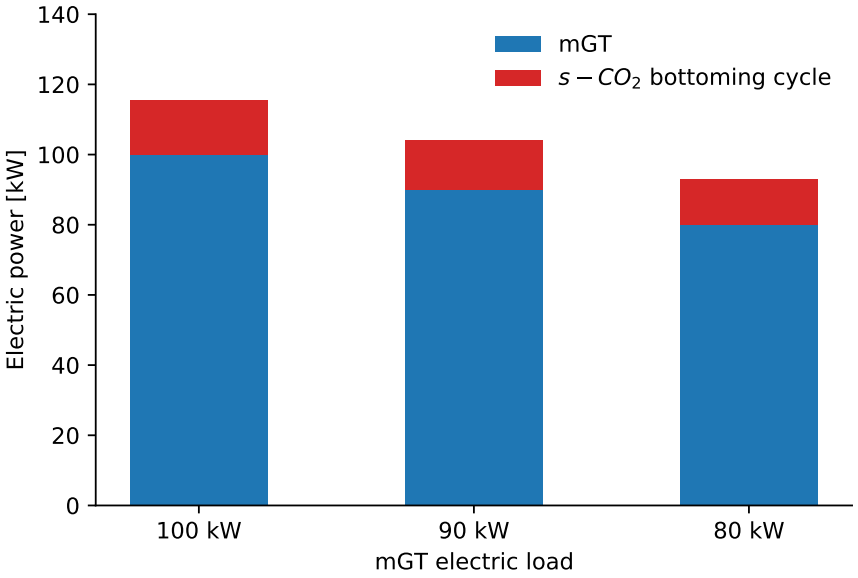

Figure 6.14: Boost in electrical power obtained when using the designed $s - CO_2$ cycle as WHR at different operating load of the mGT

With the control strategy presented in Section 3.7, the corresponding transient behaviour for the $s - CO_2$ bottoming cycle has been computed. The first thing to note is the fact that the control strategy managed to keep a stable operation of the compressor. During transient, the mass flow rate of $s - CO2$ at the compressor and turbine are not equal. A loss of power at the cold heat source decreases the turbine power. The turbine being considered choked during transient, a decrease in TIT increases the mass flow rate (see equation (3.61)). The loss of power at the compressor at constant rpm induces a decrease in compressor pressure ratio and an increase of the mass flow rate. To keep a constant rotational speed of the shaft, the generator load is reduced. When the mass flow rate of CO_2 is higher at the compressor than at the turbine, there is a mass accumulation downstream the turbine, hence an increase in density and pressure. This explains the change in pressure ratio shown in Fig. 6.17.

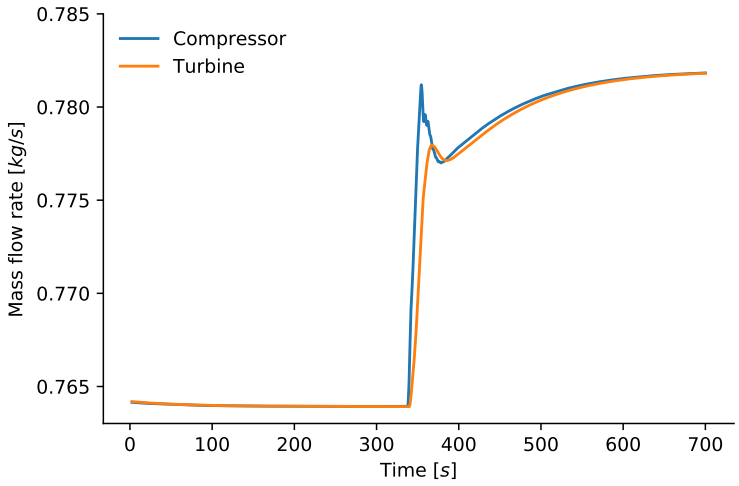

Figure 6.15: Mass flow rate of CO_2 at the turbine and compressor during the $100 - 80\,[kW]$ transient

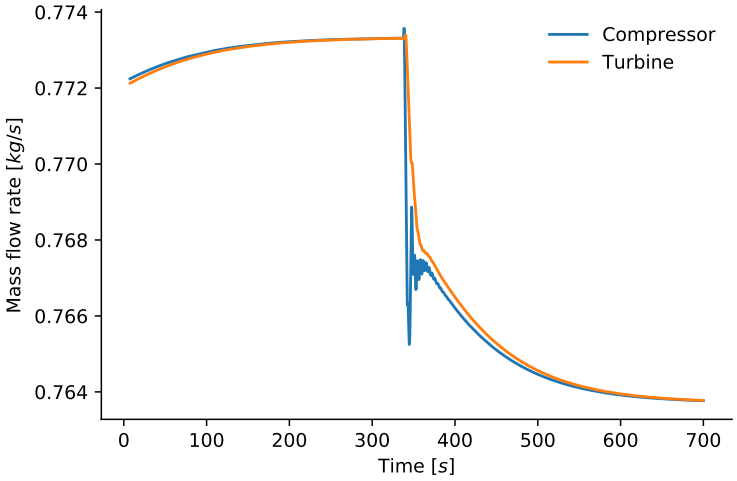

Figure 6.16: Mass flow rate of CO_2 at the turbine and compressor during during the $90 - 100\,[kW]$ transient

The oscillations visible on the compressor mass flow rate during transient on Fig. 6.16 are caused by the shaft rotational speed control.

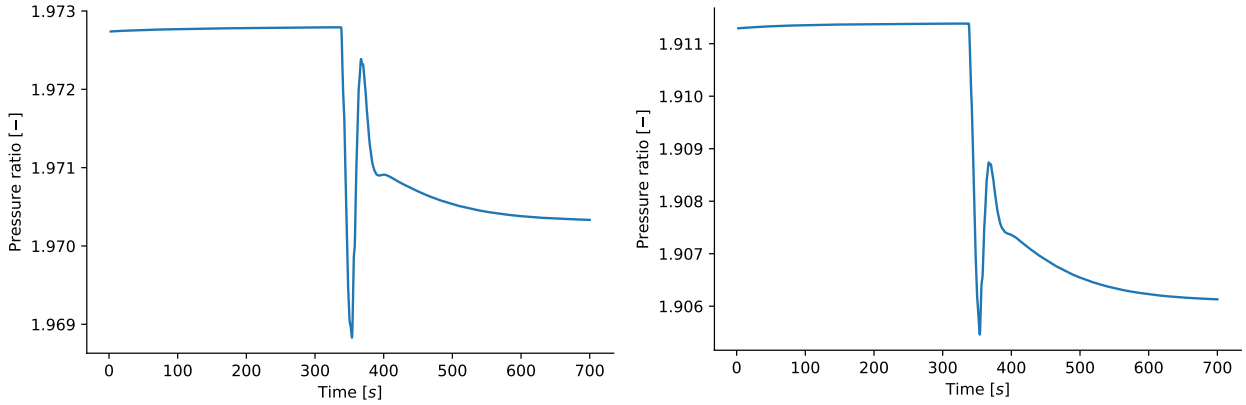

Figure 6.17: Pressure ratio of the (a) compressor and (b) turbine during the $100 - 80\,[kW]$ transient

Energy

The mechanical power at the shaft is represented on Fig. 6.18 and 6.20. We can observe that it follows well the profile of the potential of exhaust gases during transient, described on Fig. 6.19.

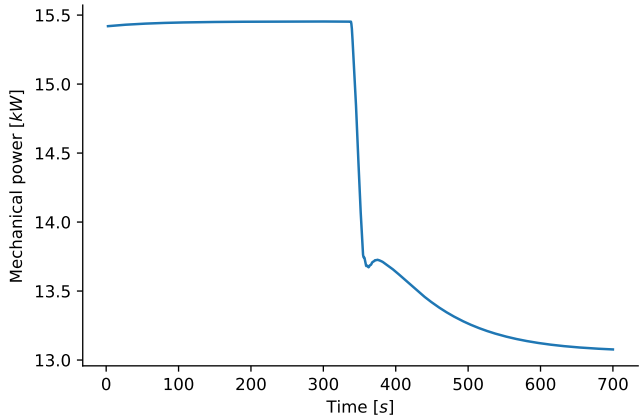

Figure 6.18: Power output during the $100 - 80\,[kW]$ transient

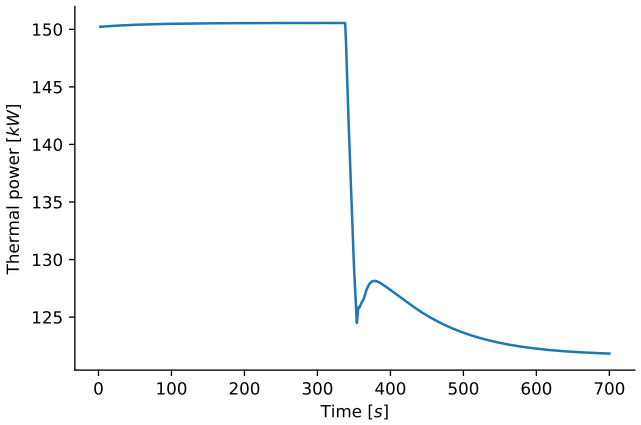

Figure 6.19: Potential of exhaust gases during the $100 - 80\,[kW]$ transient

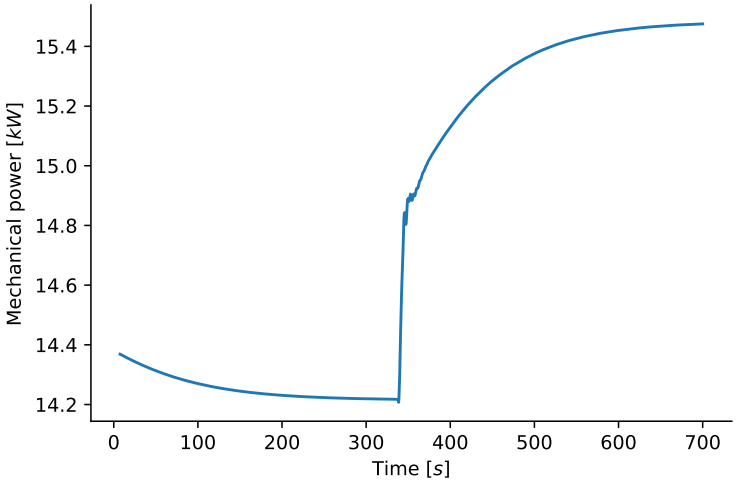

Figure 6.20: Power output during the $90 - 100\,[kW]$ transient

When the power available at the exhaust decreases, the mass flow rate of CO_2 increases. Increasing the mass flow rate of CO_2 in the cycle reduces the turbine inlet temperature. The increase in cycle efficiency is caused by the increase in mass flow rate. It increases the effectiveness of the recuperator, enhancing the internal efficiency of the cycle. As shown in Section 6.2, an increase in effectiveness of the recuperator boosts the internal efficiency but also reduces the WHR efficiency. This behaviour is visible on Fig. 6.23 and 6.22 for the $100 - 80\,[kW]$ transient and on Fig. 6.25 and 6.24 for the other one. An increase in mass flow rate also increases the pressure losses but as the recuperator design effectiveness is smaller than the optimal one in term of efficiency, an increase in recuperator effectiveness is positive in term of power conversion.

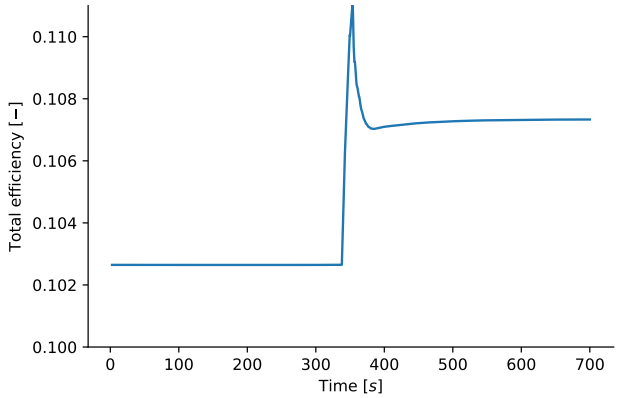

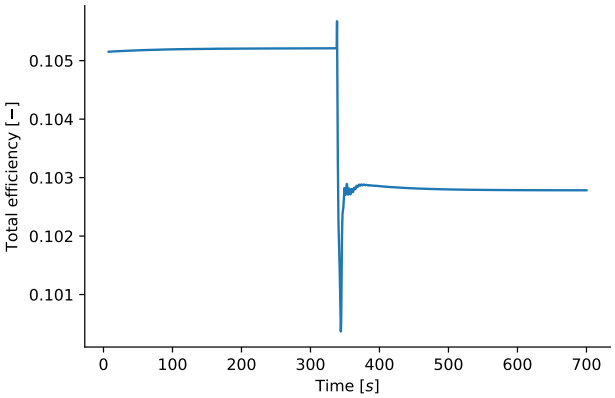

Figure 6.21: Change in total efficiency of the bottoming cycle during (a) the $100 - 80\,[kW]$ transient and (b) the $90 - 100\,[kW]$ transient

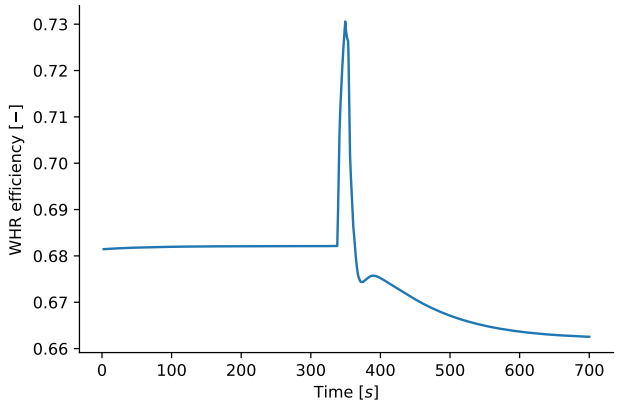

Figure 6.22: Waste heat recovery efficiency during the $100 - 80\,[kW]$ transient

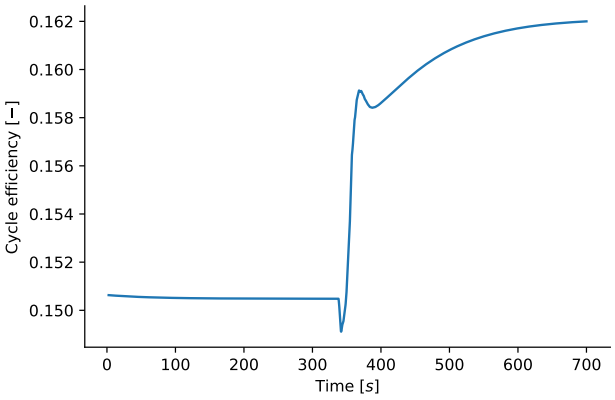

Figure 6.23: $s - CO_2$ cycle efficiency during the $100 - 80\,[kW]$ transient

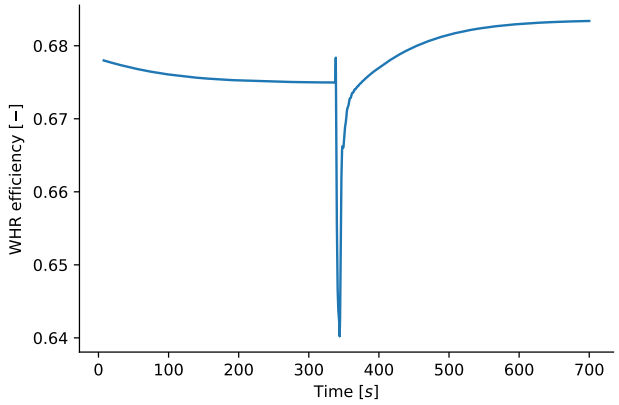

Figure 6.24: Waste heat recovery efficiency during the $90 - 100\,[kW]$ transient

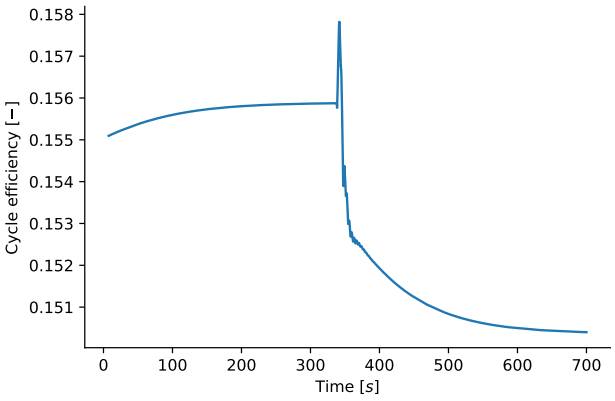

Figure 6.25: $s - CO_2$ cycle efficiency during the $90 - 100\,[kW]$ transient

Control strategy

To ensure stable operation of the compressor, a rapid change of density at its inlet is not allowed. The temperature and pressure at its inlet have then been controlled through inventory and low temperature control.

The low temperature control consists in changing the mass of water flowing through the cold heat exchanger. The set-point in term of T_1 has been fixed to $308.5\,[K]$. Decreasing T_1 increases the performances of the cycle (see Fig. 6.1) but brings the compressor closer to the choke line by increasing the reduced mass flow. The mass flow of CO_2 would become too important to recover heat from the exhaust of the mGT. The profile of T_1 during the transient operation is shown on Fig. 6.26 and the mass flow rate of water on Fig. 6.27. The controller accurately controls T_1, reducing the deviation from its set value to less than $0.1\,[°C]$. In practice the error made by the measurement devices increases the deviation of T_1. Due to its huge impact on the compressor stable operation, high precision measuring device is needed for $s-CO_2$ cycles working close to critical/pseudo-critical conditions.

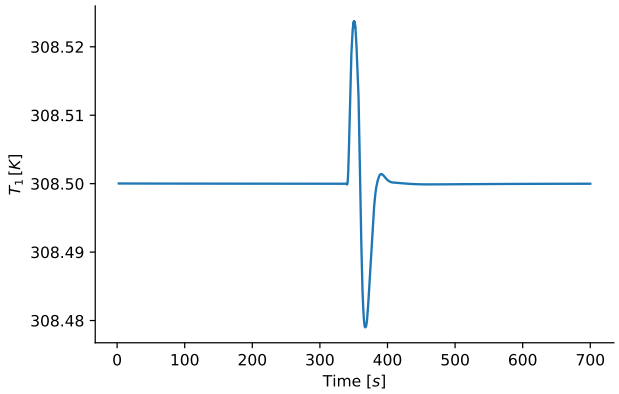

Figure 6.26: Temperature at the compressor inlet T_1 during the $100-80\,[kW]$ transient

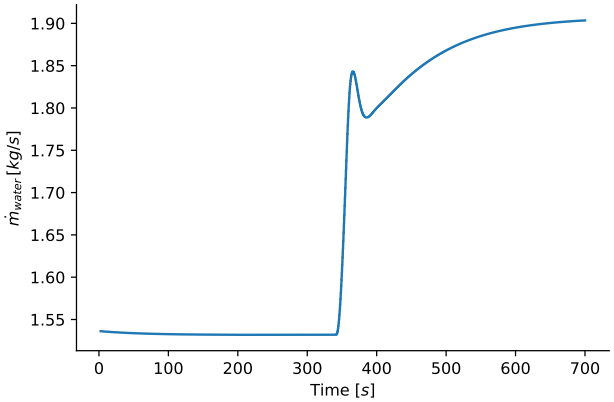

Figure 6.27: Mass flow rate of water in the cooler during the $100-80\,[kW]$ transient

Inventory control allows a control of the lowest pressure of the cycle p_1. By keeping it constant at $75.5\,[bar]$ the compressor is assured not to cross the surge line. A more clever strategy would allow a change in p_1 in order to control the turbine inlet temperature and optimize the net power output of the cycle. It would require a good knowledge of the compressor map and is hard to implement from a control level. The evolution of p_1 is represented on Fig. 6.28, and the mass flow of $s-CO_2$ going in the inventory tank on Fig. 6.29.

In this study the dynamic of the valves used in practice for inventory control have not been modeled. The time scale of the inventory controller is of $1\,[s]$, meaning that the mass flow rate $\dot{m}_{inv}$ only vary every seconds. It explains why the curve is not smooth and comprises some steps.

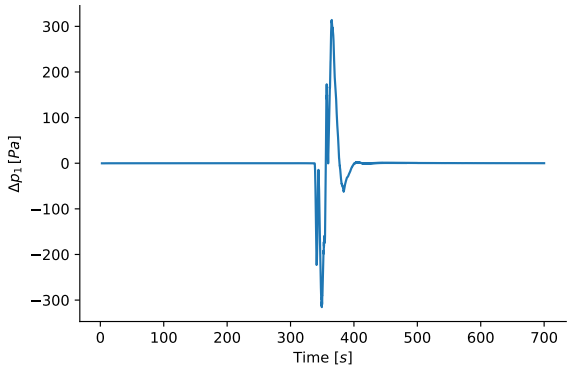

Figure 6.28: Deviation from $p_1 = 75.5\,[bar]$ during the $100 - 80\,[kW]$ transient

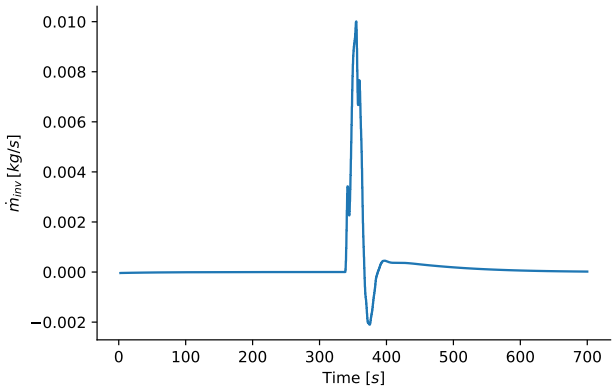

Figure 6.29: Mass flow rate of CO_2 in the inventory tank during the $100 - 80\,[kW]$ transient

The rotational speed controller managed to keep the rpm constant with a maximum deviation of 25 during the transient step, as shown on Fig. 6.30.

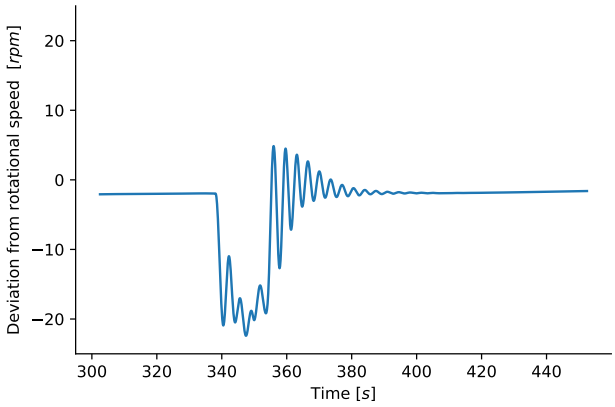

Figure 6.30: Deviation from $N = 33100\,[rpm]$ during the $100 - 80\,[kW]$ transient

With the compressor operating conditions described here above, the isentropic efficiency of the compressor stays constant during transient operation at $\eta_{is,C} = 80.53\,\%$.

CHAPTER 7

Conclusion

The aim of this thesis was to assess the potential increase of efficiency associated to the addition of a CO_2 bottoming cycle whose purpose is to valorize the waste heat of the exhaust of a mGT namely the Turbec T100. For this purpose, the implementation of, first, a steady-state model followed by a dynamic model was made. The main purpose of the steady-state, simplified model was to compare the performances of CO_2 cycles with the performances of the most mature technology existing today for waste heat recovery within the temperature ranges of the mGT; the ORC's. Because the mGT requires flexible operations due to its role in filling the gap caused by the intermittency of renewable energy, so does the CO_2 bottoming cycle. Hence a dynamic model was implemented for the analysis of transient behavior. The characterisation of the dynamic behaviour of the cycle is necessary for the development of suited and efficient control systems. This was done without any experimental data available in order to validate the model. The aim of this work is thus the first iteration in a process of modeling-construction-validation loop for an $s - CO_2$ installation.

The steady-state models were both implemented in the *Python* open-source programming language using the *CoolProp* thermodynamic library. The dynamic model was implemented using a block approach for each component of the cycle. These blocks were assembled subsequently to form a global model.

In Chapter 2, a steady-state analysis was made comparing a transcritical CO_2 cycle, a supercritical CO_2 cycle with two ORC's; one with R113, the other with R245fa. The boundary conditions were found based on thorough literature review; the constraints found mainly limited the pressure ratio for the CO_2 cycles, and the TIT of the ORC's due to thermal stability of the organic fluids. Results based on energetic and exergetic analysis as well as effectiveness for the heat exchangers showed that for the conditions applied, the R113, then the $t - CO_2$, then $s - CO_2$, then the R245fa cycle showed the best performances. The performances were essentially lowered by the cycle efficiency for the $s - CO_2$ cycle due to high compressor power consumption. The inlet conditions chosen for the compressor induce the latter to work in the vapour-like supercritical region, i.e. where fluid possesses gas-like density. This is why with the $t - CO_2$ cycle (where the inlet of the compressor is in liquid state), the power consumption of the compressor is significantly reduced. However, $s - CO_2$ showed the best performances regarding the heat transfer because of the good temperature

matching between the heated CO_2 and the exhaust gases.

A physical model was implemented and discussed for each block in Chapter 3. Special care was taken in the modeling of the compressor and the recuperator. Indeed, both work in conditions where the working fluid approaches the critical conditions where the fluid properties vary greatly with small temperature/pressure changes. The compressor needing a new map for each entry conditions to accurately model real gas behaviour, a methodology was used to derive these multiple maps from the initial compressor maps of the Turbec T100. The recuperator has been modeled the same way as in [40], because of the low complexity of the model. Different heat transfer coefficient were used at each side of the recuperator and wall thickness have been taken into account. A correlation for the UA value at each side of the recuperator has been developed to make up for the lack of experimental result. It has been validated with 3-D CFD results. Control strategy was also discussed.

Chapter 5 discusses the estimation of the different parameters used in the modeling of the component blocks. This was made with the help of a thorough review of literature on the subject.

The results obtained using this dynamic model were detailed in Chapter 6. At first, a sensitivity analysis on important parameters of the cycle has been carried out. This analysis justify the choices made during the design of the cycle and show the effect of changes in the cycle operation or design. The compressor consumption decreases with the compressibility factor Z, hence the importance of controlling its inlet conditions carefully. The second step consists in a dynamic simulation of the cycle recovering changing exhaust flow of the mGT. The exhaust given as an input for the simulation is the one obtained during a change of operation of the Turbec T100, from 100 to 80 $[kW]$ and from 90 to 100 $[kW]$.

Stable control of the cycle have been achieved by maintaining the compressor inlet conditions constant. The control strategy implemented did not take measurement errors into account and could then not be directly implemented for real application. More clever and robust control strategy should be investigated to optimize the power recovery of the bottoming cycle and maintain stable operation of the compressor despite the presence of measurement errors. For what concerns the numerical performances of the simulator, the computation to simulated time ratio was between 1/2 and 1/3, allowing real time simulation.

The primary aim of this work is a first assessment of $s-CO_2$ cycle performances in an optic of first construction of this kind of installation that could serve as a validation of this model. A numerical modeling tool for dynamic simulation has been developed to investigate the dynamics of $s-CO_2$ systems and the challenges associated.

Further improvements

- **Turbomachines**
  Using the performance maps of the Turbec T100 was a first step in $s-CO_2$ cycle modeling but it was clear in the analysis that the turbomachinery maps of the mGT were un-optimized for the application of $s-CO_2$ cycle. Indeed, pressure ratios achivied in a $s-CO_2$ cycle were significantly smaller than the ones for which the mGT are designed for.

  In the case of the compressor, this means that the compressor works in bottom of

the map further away from optimized isentropic efficiency and where the speed-lines experience pronounced non-monotonous behavior compared to speed lines at higher pressure ratios. This results in non-uniqueness of the solution i.e. for a given pressure ratio, two mass flow rates are possible. this issue is further explained in Appendix C.

In the case of the turbine, this also means that working in the bottom region of the map decreases the turbine isentropic efficiency unless the rotational speed of the turbine works at very low rpm. This region is also more sensible to rotational speed and expansion ratio change in terms of mass flow rate, i.e. for a given pressure ratio, a rpm change will induce a wider mass flow rate change than in the case of the top of the turbine map idem in the case of expansion ratio change.

The solution for this would be to make CFD simulations in order to design turbomachinery optimized for $s-CO_2$ and the range of operations it must follow or use data from $s-CO_2$ turbomachinery. From this, in the case of the compressor, one could derive a performance map from which different maps for different could be derived as done in this thesis or make several maps expanding the supercritical region allowing for interpolation of the map for the inlet conditions in between.

- **Cold source**
  The cold source was simulated in a simplified way. However, in order to achieve a more precise model, one should investigate the parameters influencing the variation of the global heat transfer of CO_2 whose conditions approach the critical point at the exit of the cold source as done for the recuperator.

- **Control strategies**
  As for now, only one combination of controlled parameters was investigated. In order to assess which control strategy would imply the best performances, further investigation requiring the control of different parameters should be done. One point of attention regarding these control strategy should always be the safe and stable operation of the compressor which is a special concern of $s-CO_2$ cycles. Indeed, staying in a stable zone in an automated fashion has shown some difficulty. For real-world applications robust controllers are necessary to take measurement errors into account while keeping the compressor stable.

- **Exhaust conditions**
  More exhaust conditions should be investigated. Indeed, as for now, only the exhaust conditions obtained during the change of operation of the mGT from 100 to 80 $[kW]$ and from 90 to 100 $[kW]$ were investigated. System startup and shutdown of the bottoming cycle have not been studied.

- **Validation**
  A future objective would ideally be the validation and calibration of the model with experimental data. This would allow for finer estimation of the parameters used in the different components of the model, for a finer estimation of pressure losses, power losses (for the shaft block), allow for more realistic hypothesis, etc.

Appendices

APPENDIX A

Global physical model

The global physical model developed in Chapter 3 is represented on next page on Fig. A.1 taking the full page space.

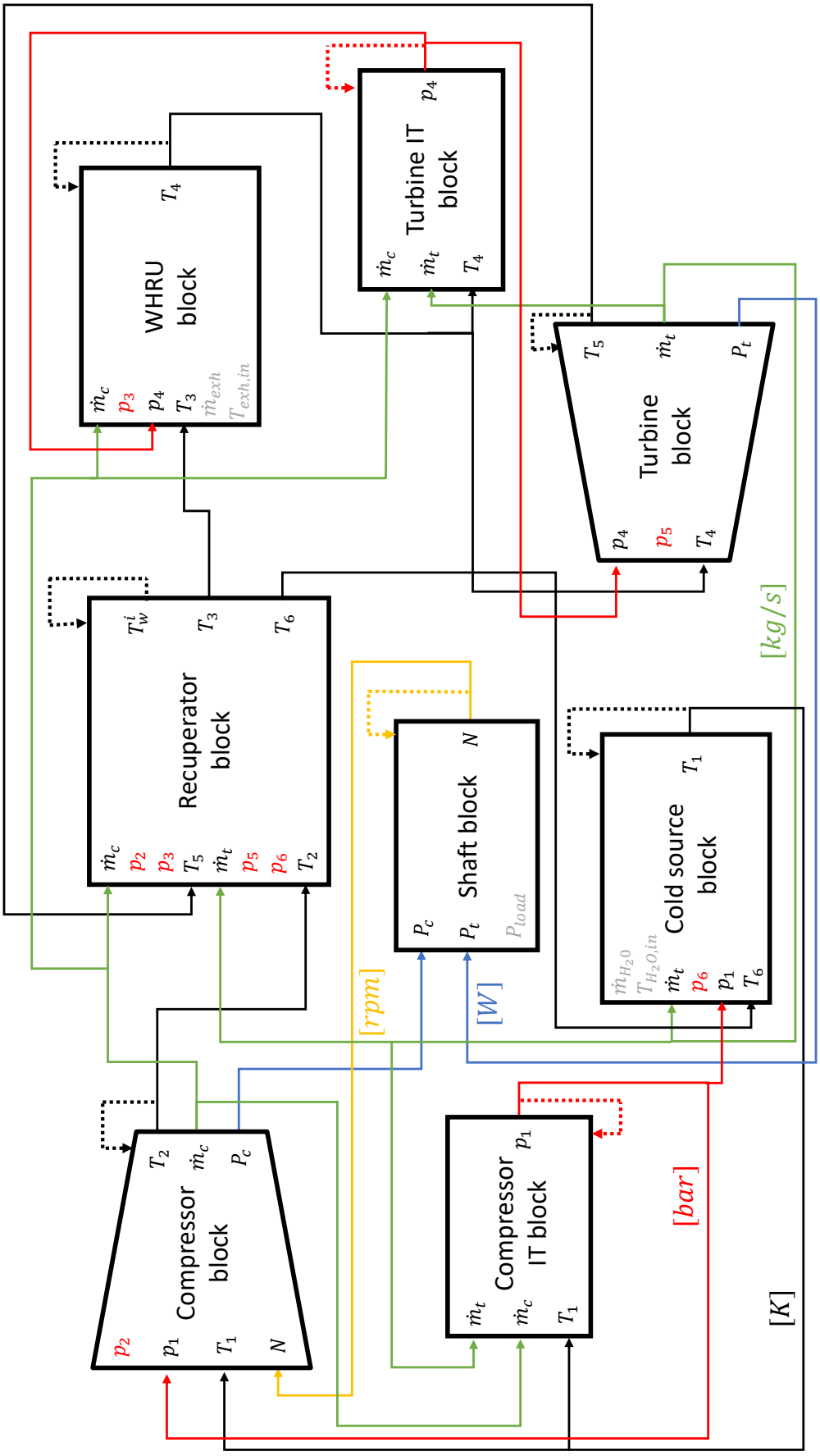

Figure A.1: Global physical model

APPENDIX B

Discussion about enthalpy

In the dynamic modeling of the $s-CO_2$ bottoming cycle, to estimate the exhaust composition, the exhaust gases were assumed to be obtained after a complete combustion with air (whose molar composition is assumed at 21 % O_2 and 79 % N_2) i.e. where no unburned products subsist in the exhaust gases (namely CO and H_2). Hence the combustion equation, using a fuel with the following molecular composition C_zH_y, is expressed as follows:

$$C_zH_y + \lambda\left(z+\frac{y}{4}\right)(O_2+3.76N_2) \longrightarrow (\lambda-1)\left(z+\frac{y}{4}\right)O_2+\frac{y}{2}H_2O+zCO_2+3.76\lambda\left(z+\frac{y}{4}\right)N_2$$

In the case of the mGT considered, based on A. Laterre's work, the exhaust were assumed to be obtained with a combustion with pure methane CH_4 and with an excess air coefficient $\lambda = 7.7\,[-]$. Hence the combustion equation gives the following exhaust composition:

O_2 %	N_2 %	H_2O %	CO_2 %
18	78	2.7	1.3

Table B.1: mGT Exhaust composition

However, in Chapter 2, air was used as a heat provider for the bottoming cycles investigated. The specific enthalpies of the exhaust and of air in function of temperature are shown on Fig. B.1(a) and the relative error e_{rel} between the two defined by equation (B.1) is shown in Fig. B.1(b).

$$e_{rel} = 100 \cdot \frac{|h_{air} - h_{exh}|}{h_{air}} \tag{B.1}$$

The enthalpies were evaluated at ambient pressure. One can see that there is a non negligible relative error in the range of temperatures experienced by the mGT exhaust. Hence the approximation of using air as exhaust can be discussed despite a very lean combustion. This is also because even if very few fuel is used in comparison to air, the proportions of O_2 and N_2 change in the exhaust because only O_2 is the oxidiser; N_2 being only a diluent. However, since the point of Chapter 2 was to compare four cycles, and that this approximation was used for all the cycles, this hypothesis is reasonable especially since the order of magnitude for the enthalpies of air and the exhaust gases is the same.

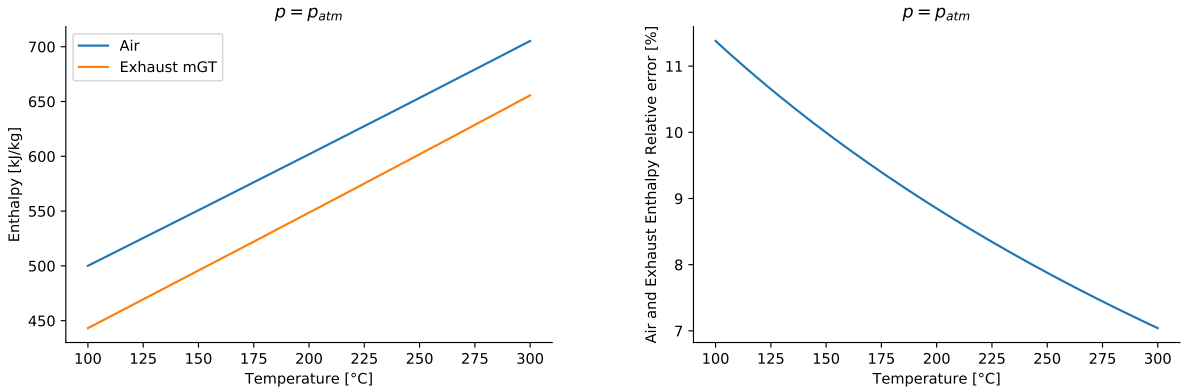

Figure B.1: (a) Specific enthalpies of air and exhaust, (b) Relative difference between air and exhaust

Furthermore, in a recuperator cell, the assumption that the second term of the following equation (B.2) was independent of temperature i.e. $\mu_T = \mu(p)$ was used in order to only use the specific heats (since the pressure p was constant in the cell) to have a direct expression for the outlet temperature of the cell (see Section 3.4.1).

$$h(p, T_2) - h(p, T_1) = c_p(p, T_2)T_2 - c_p(p, T_1)T_1 + (\mu_T(p, T_2) - \mu_T(p, T_1))p \tag{B.2}$$

The plot of μ_T in function of temperature is shown on Fig. B.2.

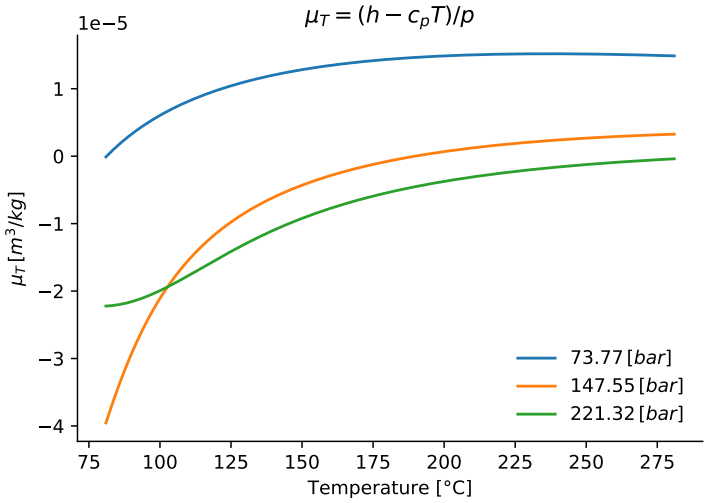

Figure B.2: μ_T of CO_2 in function of temperature

One can see that in the range of operation of the recuperator this value can be considered constant. Furthermore, the order of magnitude of μ_T is such that its difference between two temperatures would be insignificant. Hence this approximation is valid.

APPENDIX C

Ellipse and *Supershape* fits for compressor map

Because of the non monotonous behavior of the iso-speed lines on the compressor performance maps (especially for lower pressure ratio), a non-uniqueness problem arises i.e. for a given pressure ratio, two mass flow rate are possible as seen on Fig. C.1. In A. Laterre's work [40], several fits for the interpolation of the data provided by the manufacturer for the performance map of the Turbec T100 compressor were implemented. After comparing the *ellipse* and the *supershape* fit, one can observe that the first provides values outside of the domain defined in Fig. C.1 (lower mass flow rates values) and the second provides values inside this domain (mass flow rates values closer to choke).

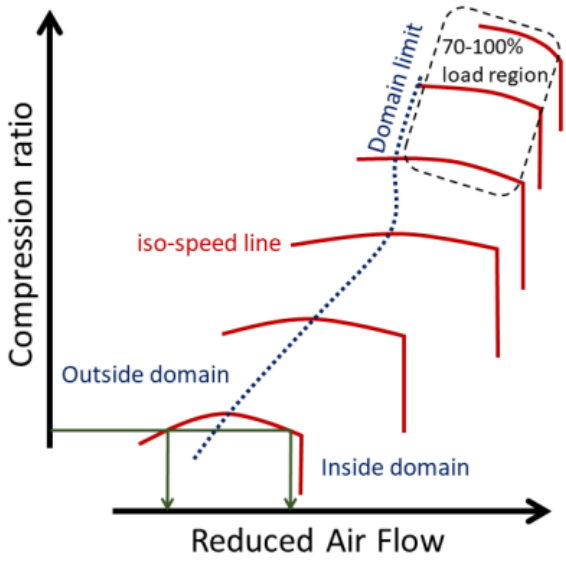

Figure C.1: Illustration of the non-uniqueness issue (figure found in [40])

One should note that usually the non-monotonous speed lines present first a pressure rise followed by a longer pressure drop. Hence, the part on the right of the dotted line on Fig. C.1 is considered outside the domain because, for a given pressure ratio, the smallest rotational speed would give a unique mass flow rate located usually on the center left of the speed line. Then, when increasing this speed, two mass flow rates are possible and the *ellipse* fit would

give the smallest of the two. But when the rotational speed increases enough for the smallest mass flow rate to be smaller than the surge mass flow for this pressure ratio, then the *ellipse* fit would have to choose the only mass flow rate left which is the one on the choke side since speed lines descend further down in pressure ratio from the one it started before rising. This would cause a mass flow rate discontinuity when increasing rotational speed as seen on Fig. C.2.

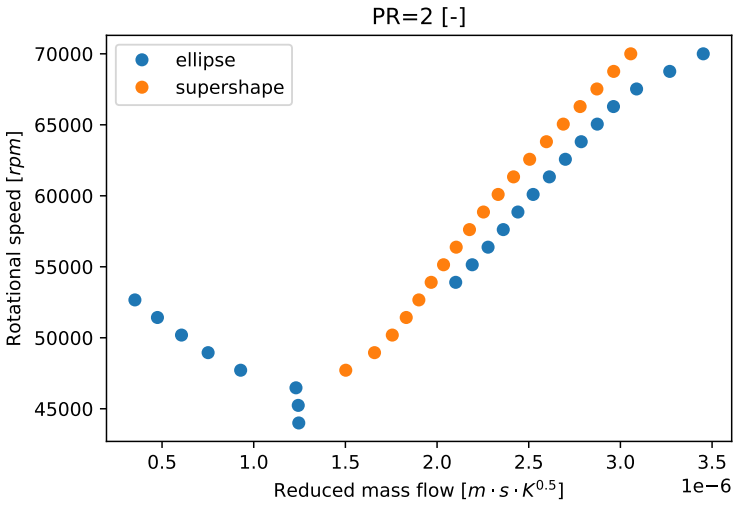

Figure C.2: Mass flow rates given by the *ellipse* and *supershape* fits for a given pressure ratio

Hence in this thesis, the *supershape* fit was chosen to avoid this discontinuity appearance. Furthermore, one can observe that the *ellipse* fit still provides a mass flow rate value (the two dotted point on the bottom of Fig. C.2) even when the rotational speed is outside the range of rotational speed range giving mass flow values for a given pressure ratio whereas the *supershape* fit stops as it should. Also, one can note that in the case where both fits give mass flow rate inside the compressor domain as defined in Fig. C.1, there is a non-negligible mass flow rate value difference between the two fits.

Bibliography

[1] Yoonhan Ahn, Seong Jun Bae, Minseok Kim, Seong Kuk Cho, Seungjoon Baik, Jeong Ik Lee, and Jae Eun Cha. Review of supercritical co2 power cycle technology and current status of research and development. *Nuclear engineering and technology*, 47(6):647–661, 2015.

[2] Dario Alfani, Marco Binotti, Ennio Macchi, Paolo Silva, and Marco Astolfi. sco2 power plants for waste heat recovery: design optimization and part-load operation strategies. *Applied Thermal Engineering*, 195:117013, 2021.

[3] T.C. Allison, J. Moore, R. Pelton, J. Wilkes, and B. Ertas. 7 - turbomachinery. In Klaus Brun, Peter Friedman, and Richard Dennis, editors, *Fundamentals and Applications of Supercritical Carbon Dioxide (sCO_2) Based Power Cycles*, pages 147–215. Woodhead Publishing, 2017.

[4] Tim Allison, Jason Wilkes, Klaus Brun, Jeffrey Moore, et al. Turbomachinery overview for supercritical co2 power cycles. In *Proceedings of the 46th Turbomachinery Symposium*. Turbomachinery Laboratory, Texas A&M Engineering Experiment Station, 2017.

[5] Maria Alessandra Ancona, Michele Bianchi, Lisa Branchini, Andrea De Pascale, Francesco Melino, Antonio Peretto, and Noemi Torricelli. Systematic comparison of orc and s-co2 combined heat and power plants for energy harvesting in industrial gas turbines. *Energies*, 14(12):3402, 2021.

[6] Ioanna Aslanidou, Moksadur Rahman, Valentina Zaccaria, and Konstantinos G. Kyprianidis. Micro Gas Turbines in the Future Smart Energy System: Fleet Monitoring, Diagnostics, and System Level Requirements. *Frontiers in Mechanical Engineering*, 7, 2021.

[7] Marco Astolfi, Dario Alfani, Silvia Lasala, and Ennio Macchi. Comparison between orc and co2 power systems for the exploitation of low-medium temperature heat sources. *Energy*, 161:1250–1261, 2018.

[8] Abubakr Ayub, Costante M Invernizzi, Gioele Di Marcoberardino, Paolo Iora, and Giampaolo Manzolini. Carbon dioxide mixtures as working fluid for high-temperature heat recovery: a thermodynamic comparison with transcritical organic rankine cycles. *Energies*, 13(15):4014, 2020.

[9] Shubham Banik, Satyaki Ray, and Sudipta De. Thermodynamic modelling of a recompression co2 power cycle for low temperature waste heat recovery. *Applied Thermal Engineering*, 107:441–452, 2016.

[10] Ian H. Bell, Jorrit Wronski, Sylvain Quoilin, and Vincent Lemort. Pure and pseudo-pure fluid thermophysical property evaluation and the open-source thermophysical property library coolprop. *Industrial & Engineering Chemistry Research*, 53(6):2498–2508, 2014.

[11] G Bianchi, S Tassou, et al. Design considerations on a small scale supercritical co2 power system for industrial high temperature waste heat to power recovery applications. 2016.

[12] F Caresana, L Pelagalli, G Comodi, and Massimiliano Renzi. Microturbogas cogeneration systems for distributed generation: Effects of ambient temperature on global performance and components' behavior. *Applied Energy*, 124:17–27, 2014.

[13] Yunus A Cengel, Michael A Boles, and Mehmet Kanoğlu. *Thermodynamics: an engineering approach*, volume 5. McGraw-hill New York, 2011.

[14] Lei Chai and Savvas A Tassou. A review of printed circuit heat exchangers for helium and supercritical co2 brayton cycles. *Thermal Science and Engineering Progress*, 18:100543, 2020.

[15] Junhyun Cho, Munkyoung Choi, Young-Jin Baik, Gilbong Lee, Ho-Sang Ra, Byunghui Kim, and Minsung Kim. Development of the turbomachinery for the supercritical carbon dioxide power cycle. *International Journal of Energy Research*, 40(5):587–599, 2016.

[16] Seong Kuk Cho, Seong Jun Bae, Yongju Jeong, Jekyoung Lee, and Jeong Ik Lee. Direction for high-performance supercritical CO_2 centrifugal compressor design for dry cooled supercritical CO_2 Brayton cycle. *Applied Sciences*, 9(19):4057, 2019.

[17] COMPUTATIONAL THERMO-FLUIDS LAB. Supercritical Energy Cycles. `https://cfd.engr.tamu.edu/supercritical-energy-cycles/`, 2022. [Online; accessed 23-May-2022].

[18] Xiaoye Dai, Lin Shi, and Weizhong Qian. Review of the working fluid thermal stability for organic rankine cycles. *Journal of thermal science*, 28(4):597–607, 2019.

[19] Chaobin Dang and Eiji Hihara. In-tube cooling heat transfer of supercritical carbon dioxide. part 1. experimental measurement. *International journal of refrigeration*, 27(7):736–747, 2004.

[20] Ward De Paepe, Marina Montero Carrero, Svend Bram, Alessandro Parente, and Francesco Contino. Toward Higher Micro Gas Turbine Efficiency and Flexibility—Humidified Micro Gas Turbines: A Review. *Journal of Engineering for Gas Turbines and Power*, 140(8), July 2018.

[21] Ward De Paepe, Alessio Pappa, Marina Montero Carrero, Laurent Bricteux, and Francesco Contino. Reducing waste heat to the minimum: Thermodynamic assessment of the m-power cycle concept applied to micro gas turbines. *Applied Energy*, 279:115898, 2020.

[22] Tianrui Deng, Xionghui Li, Qiuwang Wang, and Ting Ma. Dynamic modelling and transient characteristics of supercritical CO_2 recompression Brayton cycle. *Energy*, 180:292–302, 2019.

[23] Vaclav Dostal, Michael J Driscoll, and Pavel Hejzlar. A supercritical carbon dioxide cycle for next generation nuclear reactors. 2004.

[24] EnggCyclopedia contributors. Compressor Choke or Stonewall. `https://en.wikipedia.org/wiki/Surge_in_compressors`, 2022. [Online; accessed 11-May-2022].

[25] Huw Fox and William Bolton. *Mathematics for engineers and technologists*. Elsevier, 2002.

[26] YT Ge, L Li, X Luo, and SA Tassou. Performance evaluation of a low-grade power generation system with co2 transcritical power cycles. *Applied Energy*, 227:220–230, 2018.

[27] Karim Gharaibeh and Aaron W Costall. A flow and loading coefficient-based compressor map interpolation technique for improved accuracy of turbocharged engine simulations. 2017.

[28] Jinlan Gou, Kelong Zhang, Yuansheng Lin, Yong Li, Can Ma, and Hanbing Ke. Physical property effects of the compression process with supercritical carbon dioxide as working fluid. *Journal of Mechanical Science and Technology*, 34(8):3379–3393, 2020.

[29] Robin Govaerts and Francesco Contino. Dynamic model of a micro gas turbine.

[30] Alexander Hacks, Sebastian Schuster, Hans Josef Dohmen, Friedrich-Karl Benra, and Dieter Brillert. Turbomachine Design for Supercritical Carbon Dioxide Within the sCO2-HeRo.eu Project. *Journal of Engineering for Gas Turbines and Power*, 140(12), 11 2018. 121017.

[31] Martin Henke, Thomas Monz, and Manfred Aigner. Introduction of a new numerical simulation tool to analyze micro gas turbine cycle dynamics. *Journal of Engineering for Gas Turbines and Power*, 139(4), 2017.

[32] Yuan Jiang, Eric Liese, Stephen E Zitney, and Debangsu Bhattacharyya. Design and dynamic modeling of printed circuit heat exchangers for supercritical carbon dioxide brayton power cycles. *Applied energy*, 231:1019–1032, 2018.

[33] David Johnson, Joseph Martin, and Pierre Wauters. *Thermal power plants: energetic and exergetic approaches*. Presses universitaires de Louvain, 2015.

[34] Francisco Jurado. Modelling micro-turbines using hammerstein models. *International journal of energy research*, 29(9):841–855, 2005.

[35] Akshay Khadse, Lauren Blanchette, Jayanta Kapat, Subith Vasu, Jahed Hossain, and Adrien Donazzolo. Optimization of supercritical co2 brayton cycle for simple cycle gas turbines exhaust heat recovery using genetic algorithm. *Journal of energy resources technology*, 140(7), 2018.

[36] Min Seok Kim, Yoonhan Ahn, Beomjoo Kim, and Jeong Ik Lee. Study on the supercritical co2 power cycles for landfill gas firing gas turbine bottoming cycle. *Energy*, 111:893–909, 2016.

[37] Gregor Klemencic, S Flegkas, A Werner, M Haider, and H Leibinger. Comparison of conventional and co2 power generation cycles for waste heat recovery. In *The 5th Supercritical CO2 Power Cycles Symposium*, pages 1–15, 2016.

[38] Rafał Kowalski, Szymon Kuczyński, Mariusz Łaciak, Adam Szurlej, and Tomasz Włodek. A Case Study of the Supercritical CO2-Brayton Cycle at a Natural Gas Compression Station. *Energies*, 13(10):2447, January 2020. Number: 10 Publisher: Multidisciplinary Digital Publishing Institute.

[39] Jin Su Kwon, Seongmin Son, Jin Young Heo, and Jeong Ik Lee. Compact heat exchangers for supercritical co2 power cycle application. *Energy Conversion and Management*, 209:112666, 2020.

[40] Antoine Laterre and Francesco Contino. Towards dynamic modelling of micro gas turbines.

[41] Renaud Le Pierres, David Southall, and Stephen Osborne. Impact of mechanical design issues on printed circuit heat exchangers. In *Proceedings of SCO2 power cycle symposium*, pages 24–25. University of Colorado Bolder, 2011.

[42] Steven Lecompte, Erika Ntavou, Bertrand Tchanche, George Kosmadakis, Aditya Pillai, Dimitris Manolakos, and Michel De Paepe. Review of experimental research on supercritical and transcritical thermodynamic cycles designed for heat recovery application. *Applied Sciences*, 9(12):2571, 2019.

[43] JP Lefebvre. Physical basis of acoustics. *Acoustics: Basic Physics, Theory, and Methods*, page 1, 1998.

[44] Bo Li, Shun-sen Wang, Keke Wang, and Liming Song. Comparative investigation on the supercritical carbon dioxide power cycle for waste heat recovery of gas turbine. *Energy Conversion and Management*, 228:113670, 2021.

[45] Chengyu Li and Huaixin Wang. Power cycles for waste heat recovery from medium to high temperature flue gas sources – from a view of thermodynamic optimization. *Applied Energy*, 180:707–721, 2016.

[46] Liang Li, Yunting Ge, Xiang Luo, and Savvas A Tassou. Experimental investigation on power generation with low grade waste heat and co2 transcritical power cycle. *Energy Procedia*, 123:297–304, 2017.

[47] Xiaoya Li, Gequn Shu, Hua Tian, Lingfeng Shi, Guangdai Huang, Tianyu Chen, and Peng Liu. Preliminary tests on dynamic characteristics of a co2 transcritical power cycle using an expansion valve in engine waste heat recovery. *Energy*, 140:696–707, 2017.

[48] XL Li, GH Tang, YH Fan, and DL Yang. A performance recovery coefficient for thermal-hydraulic evaluation of recuperator in supercritical carbon dioxide brayton cycle. *Energy Conversion and Management*, 256:115393, 2022.

[49] A Mahmoudi, M Fazli, and MR Morad. A recent review of waste heat recovery by organic rankine cycle. *Applied Thermal Engineering*, 143:660–675, 2018.

[50] Giovanni Manente and Francesca Maria Fortuna. Supercritical co2 power cycles for waste heat recovery: A systematic comparison between traditional and novel layouts with dual expansion. *Energy Conversion and Management*, 197:111777, 2019.

[51] Matteo Marchionni, Giuseppe Bianchi, Apostolos Karvountzis-Kontakiotis, Apostolos Pesyridis, and Savvas A Tassou. An appraisal of proportional integral control strategies for small scale waste heat to power conversion units based on organic rankine cycles. *Energy*, 163:1062–1076, 2018.

[52] Matteo Marchionni, Giuseppe Bianchi, and Savvas A Tassou. Review of supercritical carbon dioxide ($s - CO_2$) technologies for high-grade waste heat to power conversion. *SN Applied Sciences*, 2(4):1–13, 2020.

[53] Matteo Marchionni, Giuseppe Bianchi, and Savvas A Tassou. Transient analysis and control of a heat to power conversion unit based on a simple regenerative supercritical CO2 Joule-Brayton cycle. *Applied Thermal Engineering*, 183:116214, 2021.

[54] Matteo Marchionni, Lei Chai, Giuseppe Bianchi, and Savvas A Tassou. Numerical modelling and transient analysis of a printed circuit heat exchanger used as recuperator for supercritical co2 heat to power conversion systems. *Applied Thermal Engineering*, 161:114190, 2019.

[55] Mark R. Anderson. Performance corrections for compressor maps. https://www.conceptsnrec.com/blog/performance-corrections-for-compressor-maps, 2019. [Online; accessed 04-May-2022].

[56] Alberto Jose Martel Matos. *Preliminary Aerodynamic Design of a Supercritical Carbon Dioxide Centrifugal Compressor*. PhD thesis, Carleton University, 2018.

[57] Anton Moisseytsev and James J Sienicki. Controllability of the supercritical carbon dioxide brayton cycle near the critical point. In *Proceedings of the 2008 International Congress on Advances in Nuclear Power Plants-ICAPP'08*, 2008.

[58] Benjamín Monge, D Sánchez, M Savill, and Tomás Sánchez. Exploring the design space of the sco2 power cycle compressor. In *Proceedings of the 4th International Symposium on Supercritical CO2 Power Cycles*. Citeseer, 2014.

[59] Leonid Moroz, Petr Pagur, Oleksii Rudenko, Maksym Burlaka, and Clement Joly. Evaluation for scalability of a combined cycle using gas and bottoming sco2 turbines. In *ASME Power Conference*, volume 56604, page V001T09A007. American Society of Mechanical Engineers, 2015.

[60] G. Musgrove, S. Sullivan, D. Shiferaw, P. Fourspring, and L. Chordia. 8 - heat exchangers. In Klaus Brun, Peter Friedman, and Richard Dennis, editors, *Fundamentals and Applications of Supercritical Carbon Dioxide (sCO_2) Based Power Cycles*, pages 217–244. Woodhead Publishing, 2017.

[61] Konstantin Nikitin, Yasuyoshi Kato, and Lam Ngo. Printed circuit heat exchanger thermal–hydraulic performance in supercritical co2 experimental loop. *International Journal of refrigeration*, 29(5):807–814, 2006.

[62] Diogo C Nunes, Jan EMG Pinto, Daniel GV Fonseca, André L Maitelli, and Fábio MU Araújo. Relay based pid auto-tuning applied to a multivariable level control system. In *2014 11th International Conference on Informatics in Control, Automation and Robotics (ICINCO)*, volume 1, pages 741–748. IEEE, 2014.

[63] Olumide Olumayegun and Meihong Wang. Dynamic modelling and control of supercritical CO2 power cycle using waste heat from industrial processes. *Fuel*, 249:89–102, 2019.

[64] Valeria Palomba and Andrea Frazzica. Modeling of sorption systems for thermal energy storage. In *Advances in Thermal Energy Storage Systems*, pages 453–475. Elsevier, 2021.

[65] V Pandey, P Kumar, and P Dutta. Thermo-hydraulic analysis of compact heat exchanger for a simple recuperated sco2 brayton cycle. *Renewable and Sustainable Energy Reviews*, 134:110091, 2020.

[66] Hong-Son Pham, Nicolas Alpy, Jean-Henry Ferrasse, Olivier Boutin, Mark Tothill, Johann Quenaut, Olivier Gastaldi, Thierry Cadiou, and Manuel Saez. An approach for establishing the performance maps of the sc-co2 compressor: Development and qualification by means of cfd simulations. *International Journal of Heat and Fluid Flow*, 61:379–394, 2016.

[67] N Thiwaan Rao, AN Oumer, and UK Jamaludin. State-of-the-art on flow and heat transfer characteristics of supercritical co2 in various channels. *The Journal of supercritical fluids*, 116:132–147, 2016.

[68] Johannes Ratz, Sebastian Leichtfuß, Maximilian Beck, Heinz-Peter Schiffer, and Friedrich Fröhlig. Surge margin optimization of centrifugal compressors using a new objective function based on local flow parameters. *International Journal of Turbomachinery, Propulsion and Power*, 4(4):42, 2019.

[69] Fabrizio Reale, Vincenzo Iannotta, and Raffaele Tuccillo. Numerical study of a micro gas turbine integrated with a supercritical co2 brayton cycle turbine. In *Turbo Expo: Power for Land, Sea, and Air*, volume 51173, page V008T26A018. American Society of Mechanical Engineers, 2018.

[70] Fabrizio Reale, Raniero Sannino, and Raffaele Tuccillo. Micro gas turbine integrated with a supercritical co2 brayton cycle turbine: Layout comparison and thermodynamic analysis. In *Turbo Expo: Power for Land, Sea, and Air*, volume 84195, page V008T20A011. American Society of Mechanical Engineers, 2020.

[71] Alessandro Romei. Turbomachinery operating in the non-ideal compressible fluid-dynamic regime: a step towards next-generation power systems. 2021.

[72] Alessandro Romei and Giacomo Persico. Computational fluid-dynamic modelling of two-phase compressible flows of carbon dioxide in supercritical conditions. *Applied Thermal Engineering*, 190:116816, 2021.

[73] Sjolander S.A. *"MECH 4305 Fluid Machinery Supplementary Notes.* Carleton University, Department of Mechanical and Aerospace Engineering. Ottawa, ON, Canada, 2017.

[74] Muhammed Saeed, Khaled Alawadi, and Sung Chul Kim. Performance of supercritical co2 power cycle and its turbomachinery with the printed circuit heat exchanger with straight and zigzag channels. *Energies*, 14(1):62, 2020.

[75] Salma I Salah, Mahmoud A Khader, Martin T White, and Abdulnaser I Sayma. Mean-line design of a supercritical CO_2 micro axial turbine. *Applied Sciences*, 10(15):5069, 2020.

[76] Samira Sayad Saravi and Savvas A Tassou. An investigation into sCO_2 compressor performance prediction in the supercritical region for power systems. *Energy Procedia*, 161:403–411, 2019.

[77] Han Seo, Jae Eun Cha, Jaemin Kim, Injin Sah, and Yong-Wan Kim. Design and performance analysis of a supercritical carbon dioxide heat exchanger. *Applied Sciences*, 10(13):4545, 2020.

[78] RK Shah. Classification of heat exchangers. *Heat Exchangers: Thermal-Hydraulic Fundamentals and Design*, 1986.

[79] Hyungki Shin, Junhyun Cho, Young-Jin Baik, Jongjae Cho, Chulwoo Roh, Ho-Sang Ra, Youngseok Kang, and Jaesung Huh. Partial admission, axial impulse type turbine design and partial admission radial turbine test for sco2 cycle. In *Turbo Expo: Power for Land, Sea, and Air*, volume 50961, page V009T38A019. American Society of Mechanical Engineers, 2017.

[80] SimulateLive. Introduction to Black Box Modeling in Process Industry. https://simulatelive.com/process/monitoring/introduction-to-black-box-modeling-in-process-industry, 2020. [Online; accessed 23-May-2022].

[81] Ping Song, Zhenxing Zhao, Lie Chen, Chunhui Dai, Chonghai Huang, Mengran Liao, Xingsheng Lao, Yuansheng Lin, and Wei Wang. Research on dynamic modeling of the supercritical carbon dioxide power cycle. *Processes*, 9(11):1946, 2021.

[82] Tri Quang Trinh. *Dynamic response of the supercritical $C0_2$ Brayton recompression cycle to various system transients*. PhD thesis, Massachusetts Institute of Technology, 2009.

[83] WPJ Visser and ID Dountchev. Modeling thermal effects on performance of small gas turbines. In *Turbo Expo: Power for Land, Sea, and Air*, volume 56628, page V001T01A014. American Society of Mechanical Engineers, 2015.

[84] Ales Vojacek, Tomas Melichar, Petr Hájek, Frantisek Doubek, and Timm Hoppe. Experimental investigations and simulations of the control system in supercritical CO2 loop. *3rd European Conference on Supercritical CO2 (sCO2) Power Systems 2019: 19th-20th September 2019*, pages 89–104, October 2019. Conference Name: 3rd European supercritical CO2 Conference September 19-20, 2019, Paris, France.

[85] Harald Taxt Walnum, Daniel Rohde, and Yves Ladam. Off-design analysis of ORC and CO2 power production cycles for low-temperature surplus heat recovery. *International Journal of Low-Carbon Technologies*, 8(1):29–36, January 2012. _eprint: https://academic.oup.com/ijlct/article-pdf/8/1/29/2218840/ctr043.pdf.

[86] Xurong Wang and Yiping Dai. Exergoeconomic analysis of utilizing the transcritical co2 cycle and the orc for a recompression supercritical co2 cycle waste heat recovery: A comparative study. *Applied energy*, 170:193–207, 2016.

[87] Martin T White, Giuseppe Bianchi, Lei Chai, Savvas A Tassou, and Abdulnaser I Sayma. Review of supercritical co2 technologies and systems for power generation. *Applied Thermal Engineering*, 185:116447, 2021.

[88] Wikipedia contributors. Molecular mass — Wikipedia, the free encyclopedia. http://https://en.wikipedia.org/wiki/Molecular_mass, 2022. [Online; accessed 04-May-2022].

[89] Wikipedia contributors. Surge in compressors — Wikipedia, the free encyclopedia. https://en.wikipedia.org/wiki/Surge_in_compressors, 2022. [Online; accessed 09-May-2022].

[90] Steven A Wright, Ross F Radel, Milton E Vernon, Gary E Rochau, and Paul S Pickard. Operation and analysis of a supercritical co2 brayton cycle. *Sandia Report, No. SAND2010-0171*, 2010.

[91] Gang Xiao, Tianfeng Yang, Huanlei Liu, Dong Ni, Mario Luigi Ferrari, Mingchun Li, Zhongyang Luo, Kefa Cen, and Mingjiang Ni. Recuperators for micro gas turbines: A review. *Applied Energy*, 197:83–99, 2017.

[92] Jinliang Xu, Chao Liu, Enhui Sun, Jian Xie, Mingjia Li, Yongping Yang, and Jizhen Liu. Perspective of s- co2 power cycles. *Energy*, 186:115831, 2019.

[93] Suk Young Yoon, Min Jae Kim, In Seop Kim, and Tong Seop Kim. Comparison of micro gas turbine heat recovery systems using orc and trans-critical co2 cycle focusing on off-design performance. *Energy procedia*, 129:987–994, 2017.

[94] Haoshui Yu, Donghoi Kim, and Truls Gundersen. Cascaded transcritical/supercritical co2 cycles and organic rankine cycles to recover low-temperature waste heat and lng cold energy simultaneously. *International Journal of Energy and Power Engineering*, 12(4):286–290, 2018.

[95] Peng Zhang and P Zhang. Industrial control system simulation routines. *Advanced industrial control technology*, 784, 2010.

[96] Christoph Zöphel, Steffi Schreiber, Theresa Müller, and Dominik Möst. Which flexibility options facilitate the integration of intermittent renewable energy sources in electricity systems? *Current Sustainable/Renewable Energy Reports*, 5(1):37–44, 2018.

UNIVERSITÉ CATHOLIQUE DE LOUVAIN
École polytechnique de Louvain
Rue Archimède, 1 bte L6.11.01, 1348 Louvain-la-Neuve, Belgique | **www.uclouvain.be/epl**